

BIOPHYSICS

Gene-scale *in vitro* reconstitution reveals histone acetylation directly controls chromatin architecture

Yohsuke T. Fukai^{1,2,*}, Tomoya Kujirai^{3,4}, Masatoshi Wakamori⁵, Setsuko Kanamura^{1,2†}, Lisa Yamauchi^{1,2†}, Somayeh Zeraati^{1,2†}, Satoshi Morita⁶, Chiharu Tanegashima⁷, Mitsutaka Kadota⁷, Mikako Shirouzu^{6,8}, Hitoshi Kurumizaka^{3,4,9}, Takashi Umebara^{5,8,10}, Kyogo Kawaguchi^{1,2,11*}

Understanding how epigenetic modifications intrinsically shape gene-scale chromatin architecture remains challenging due to difficulties in reconstituting and characterizing sufficiently long arrays with defined modification patterns. Here, we overcome this barrier by reconstituting 20-kilobase (96-nucleosome) chromatin arrays with modification patterns precisely controlled at 12-nucleosome resolution. Single-molecule microscopy reveals the dynamics governed by hydrodynamic interactions, demonstrating that increasing histone H4 acetylation density enhances structural fluctuations and relaxation times. *In vitro* Hi-C reveals power-law decay of the nucleosome contacts consistent with the Gaussian chain, which is globally reduced by acetylation. We also observe that heterogeneous modification patterns alone are sufficient to create distinct structural domains reminiscent of higher-order chromatin organization. These findings establish how histone modifications modulate chromatin architecture via changes in local stiffness and nucleosome interactions, providing a quantitative framework for genome organization.

INTRODUCTION

The dynamic regulation of chromatin structure plays a crucial role in establishing and maintaining the cell identity of eukaryotes (1–3). Distinct histone modification patterns have been correlated with the three-dimensional genome structure (4–6). However, the molecular mechanisms underlying these structures are multifaceted; they encompass not only direct physical interactions between nucleosomes (7–9) but also the action of various proteins that recognize specific epigenetic modifications (10–14). The limited control over the chromatin environment *in vivo* makes it challenging to disentangle the contributions and interdependencies of diverse mechanisms shaping large-scale chromatin structure and dynamics across genes or regulatory domains.

Reconstituted chromatin systems offer a powerful way to overcome these limitations, as they enable precise manipulation of factors

Copyright © 2025 The Authors, some rights reserved; exclusive licensee American Association for the Advancement of Science. No claim to original U.S. Government Works. Distributed under a Creative Commons Attribution NonCommercial License 4.0 (CC BY-NC).

Downloaded from https://www.science.org at Rikagaku Kenkyusho Library of Riken on November 19, 2025

at the single-nucleosome level (9, 14, 15). Studies using regularly spaced 12-mer arrays have shown that chromatin structure depends on histone acetylation (7, 8), protein binding (16, 17), and linker DNA length (18) and can undergo liquid–liquid phase separation or aggregation at high concentrations (19, 20). Yet, replicating the complex, large-scale organization found *in vivo*, especially domains potentially defined by heterogeneous histone modifications (21), remains a major challenge using traditional methods. Developing *in vitro* systems that faithfully capture both the relevant length scale and epigenetic heterogeneity of genomic regions is crucial for dissecting fundamental mechanisms of genetic regulation.

A deeper challenge lies in determining the fundamental physical nature of nucleosome–nucleosome interactions within these larger arrays. While histone acetylation is believed to decompact chromatin by neutralizing positive charges on histone tails, its broader influence for higher-order structural configurations remains incompletely understood. Moreover, simple polymer models often treat nucleosomes as interacting monomers undergoing normal Brownian motion, overlooking key factors such as the hydrodynamic coupling between the nucleosomes via the surrounding solvent. Resolving how these interactions shape chromatin dynamics is critical for more accurate physical models of genome organization and for understanding processes like transcriptional regulation that depend on nucleosome accessibility under fluctuation.

To address these points, we developed a method to reconstitute 20-kb, 96-mer long nucleosome arrays with defined histone modification patterns controlled at 12-mer resolution. By direct single-molecule observation of the endpoint fluctuation, we uncover the relationship between histone H4 acetylation patterns, structure, and dynamics at the scale involving distal interactions within the chromatin chain. Using the barcodes introduced at single nucleosome resolution, we further probe the conformation of the reconstituted nucleosome arrays through *in vitro* conformation capture experiments (*i.e.*, *in vitro* Hi-C). The obtained contact map validates how the patterning of histone modifications is sufficient to induce

¹Nonequilibrium Physics of Living Matter RIKEN Hakubi Research Team, RIKEN Center for Biosystems Dynamics Research, 2-2-3 Minatojima-minamimachi, Chuo-ku, Kobe, Hyogo 650-0047, Japan. ²Nonequilibrium Physics of Living Matter Laboratory, RIKEN Pioneer Research Institute, 2-2-3 Minatojima-minamimachi, Chuo-ku, Kobe, Hyogo 650-0047, Japan. ³Laboratory of Chromatin Structure and Function, Institute for Quantitative Biosciences, The University of Tokyo, 1-1-1 Yayoi, Bunkyo-ku, Tokyo 113-0033, Japan. ⁴Laboratory for Transcription Structural Biology, RIKEN Center for Integrative Medical Sciences, 1-7-22 Suehiro-cho, Tsurumi-ku, Yokohama 230-0045, Japan. ⁵Laboratory for Epigenetics Drug Discovery, RIKEN Center for Biosystems Dynamics Research, 1-7-22 Suehiro-cho, Tsurumi-ku, Yokohama, Kanagawa 230-0045, Japan. ⁶Drug Discovery Structural Biology Platform Unit, RIKEN Center for Integrative Medical Sciences, 1-7-22 Suehiro-cho, Tsurumi-ku, Yokohama, Kanagawa 230-0045, Japan. ⁷Laboratory for Developmental Genome System, RIKEN Center for Biosystems Dynamics Research, 2-2-3 Minatojima-minamimachi, Chuo-ku, Kobe, Hyogo 650-0047, Japan. ⁸Laboratory for Protein Functional and Structural Biology, RIKEN Center for Integrative Medical Sciences, 1-7-22 Suehiro-cho, Tsurumi-ku, Yokohama, Kanagawa 230-0045, Japan. ⁹Department of Biological Sciences, Graduate School of Science, The University of Tokyo, 1-1-1 Yayoi, Bunkyo-ku, Tokyo 113-0032, Japan. ¹⁰Department of Pharmacy, College of Pharmaceutical Sciences, Ritsumeikan University, 1-1-1 Noji-higashi, Kusatsu, Shiga 525-8577, Japan. ¹¹Institute for Physics of Intelligence, Department of Physics, The University of Tokyo, 7-3-1 Hongo, Bunkyo-ku, Tokyo 113-0033, Japan.

*Corresponding author. Email: ysk@yfukai.net (Y.T.F.); kyogo.kawaguchi@riken.jp (K.K.).
†These authors contributed equally to this work.

heterogeneous contacts at kilobase scales, resembling higher-order structures observed *in vivo*.

RESULTS

Reconstituting chromatin with defined nucleosome modifications

To construct long arrays of nucleosomes with defined histone modification patterns, we first reconstituted 12-mer nucleosome arrays with distinctly modified human histone octamers and subsequently pooled them to ligate up to 96-mers (Fig. 1A). This approach scales

up the strategy previously applied to generate shorter arrays (4- to 25-mers) (22–24), extending both the length and number of arrays. The DNA fragments we designed consist of twelve repeats of the Widom 601 sequence (25), separated by linker sequences (Fig. 1B). The Widom 601 sequence enables reproducible nucleosome positioning with high efficiency without the aid of chaperones. Sticky ends of these 12-mers can only be ligated in the designed order (Fig. 1, A and B), allowing the creation of defined sequences of histone modification patterns at 12-mer resolution. We chose histone tail acetylation in this study, considering its well-established role in gene activation and its demonstrated capacity to directly influence

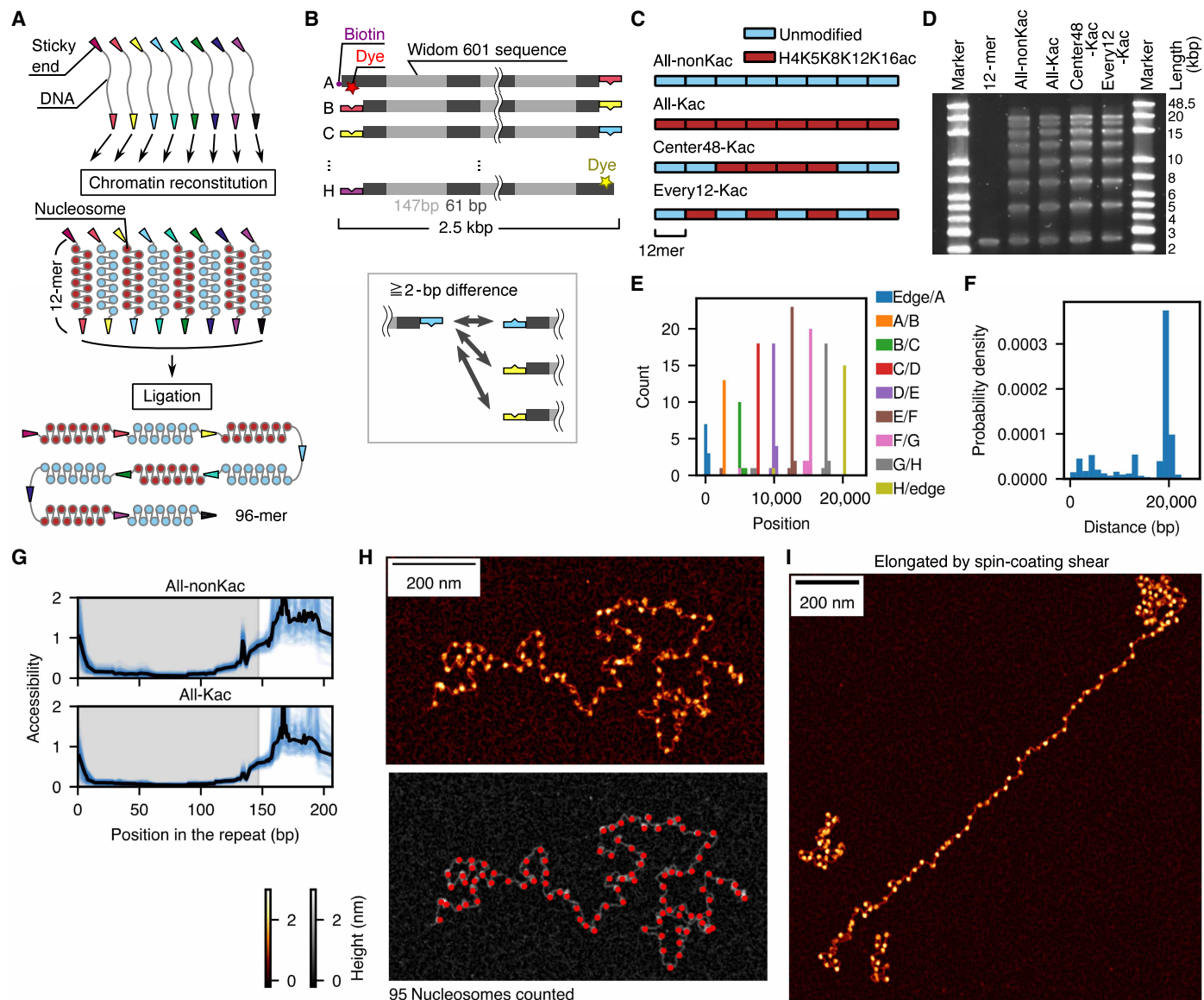


Fig. 1. Reconstituting chromatin arrays with defined histone modifications. (A) Schematics of the experiment. (B) Design of the eight 12-mer arrays. (C) Design of the histone modification patterns. (D) Electrophoresis result of the ligated product of eight 12-mer arrays. (E) Counts of the ligated regions at each position found in Nanopore sequences. (F) Sequence bias-corrected distribution of the length of nonbarcoded chromatin when subsampling the sequences with both ends of the 96-mer design. (G) Accessibility of the DNA in all repeats in the long chromatin arrays. The gray-shaded region indicates the 601 sequence, and the white region indicates the linker. (H) AFM image of a reconstituted long array. Each observed blob likely corresponds to a nucleosome, resulting in a total count of 95 nucleosomes. The red points show the detected nucleosome positions. (I) AFM image of a reconstituted 96-mer chromatin array observed after applying shear by the spin coater to elongate the chains (see Materials and Methods). The image also shows two shorter arrays, identified as 12-mer and 24-mer arrays.

chromatin structure. We used H4 tail tetra-acetylation (Kac; i.e., H4K5K8K12K16ac) to reproduce the H4 hyperacetylation found in the transcriptionally active chromatin (26–29). The acetylated 12-mers were combined with unmodified 12-mers to construct four distinctly patterned arrays: all acetylated (All-Kac), all nonacetylated (All-nonKac), center region acetylated (Center48-Kac), and 12-mer alternatingly acetylated (Every12-Kac) patterns (Fig. 1C and fig. S1A).

To construct long nucleosome arrays with high histone-loading fractions on 601 sequences, we first reconstituted the 12-mer arrays with an optimized method (see Materials and Methods). Gel shift assays confirmed efficient reconstitution of the 12-mers, showing that less than 5% of the DNA remained unbound to histones (fig. S1, B to I). We also checked the uniformity of the reconstitution visually by atomic force microscopy (AFM); around 90% of detected arrays counted 12 blobs that correspond to nucleosomes (fig. S1, J and K).

To efficiently ligate the 12-mers into larger structures, we optimized the concentration of the samples, magnesium ions, and adenosine triphosphate (ATP); magnesium ions induce undesired aggregation for nucleosomes but are necessary for the ligation reaction by T4 DNA ligase. With the ligation condition that yielded 96-mers with a high fraction (Fig. 1D), the nucleosomes remained intact after the ligation as assessed by the gel shift assay (fig. S2A). By Nanopore sequencing, we also confirmed that the ligation sites identified in the long reads corresponded to the designed positions (Fig. 1E and fig. S2B), and the length distribution of strands containing both end sequences had a sharp peak around 20 kb, matching the design (Fig. 1F and fig. S2C). The positioning of the histones on the 601 sequence was also confirmed by the accessibility assay by adenine methylation (fig. S3) (30, 31), where enzyme access was found to be almost completely suppressed at the positions of histones (Fig. 1G).

We further validated the ligated products by AFM (Fig. 1, H and I, and fig. S4). By optimizing the imaging protocol, we were able to reach a resolution where we could count the number of histones contained in the nucleosomes, which were close to 96 for the largest structures (Fig. 1, H and I, and fig. S4, A to F). In the AFM images, we also observed intermediate products corresponding to the heterogeneous population of arrays in multiples of 12-mers (Fig. 1, D and I, and fig. S4, G to M).

Spatiotemporal fluctuation of nucleosomes depends on the fraction of acetylation

Next, we aimed to characterize the spatiotemporal structural fluctuation of 96-mers and its dependence on histone modification patterns by single-molecule microscopy. Fully ligated arrays should contain distinctly colored fluorescent probes at both ends (Figs. 1B and 2A). We designed an observation chamber passivated with polyethylene glycol to minimize nonspecific binding to the substrate (see Materials and Methods). The chamber can introduce fluid flow, which allows the exchange of the buffer into distinct salt conditions, as well as the application of shear force to check the extent of elongation of the molecules (Fig. 2, B and C). We excluded molecules nonspecifically bound to the substrate postimaging and focused on molecules that fluctuated significantly during the observation and elongated sufficiently upon the application of shear (fig. S5, A to C).

The molecules presented fluctuation at the size of around 100 to 200 nm (Fig. 2, C and D, and fig. S5D) and elongated to the length of 750 to 1500 nm when applied shear, consistent with the expected

size of 96-mer nucleosomes (fig. S5, B and C). The amplitude of the fluctuation had a clear histone modification dependence: The arrays had larger fluctuation with the acetylated nucleosomes compared with the nonacetylated nucleosomes, consistent with the acetylated histones having weaker attractive interactions between the histone tails and negatively charged regions such as the acidic patches of the nucleosomes and DNA. This difference was enhanced in the physiological salt condition (150 mM KCl) and was not seen for 50 mM KCl, indicating that the charge difference induced by acetylation is a subtle effect that depends substantially on the environment. At lower salt concentrations, repulsive interactions between DNA dominate and expand the array regardless of the nucleosome interactions, whereas at higher salt concentrations, electrostatic screening mitigates these DNA-DNA repulsions, allowing modification-dependent histone-histone and/or histone-DNA interactions to become prominent. We also found a consistent result in the size of molecules observed by AFM; at 150 mM KCl, acetylated arrays tended to be larger compared to the nonacetylated, a difference undetectable at the 12-mer scale but becoming significant beyond 24-mers (fig. S6, A to C). Diffusion coefficients of free-floating single 12-mer nucleosomes, however, showed a significant difference between acetylated and nonacetylated arrays (Fig. 2E).

We found that the patterned chromatin with half of the histones being acetylated (Center48-Kac and Every12-Kac) tended to fluctuate in size between the fully acetylated and nonacetylated arrays (Fig. 2D and fig. S5D). The difference between the distinct patterns of acetylation, the Center48-Kac and Every12-Kac arrays, was not detected in the single-molecule fluorescence microscopy (Fig. 2D and fig. S5D) and AFM (fig. S6D), indicating that the pattern dependence in heterogeneously modified chromatin is small if the overall acetylation fraction is the same.

From the live imaging data, we further estimated the true width of the end-to-end fluctuation and its timescale of relaxation by changing the number of averaging frames and fitting the fluctuation amplitude with a theoretical model accounting for the finite camera exposure time (Fig. 2F and fig. S5E; see Materials and Methods). The timescale of relaxation, around 10 ms or less (Fig. 2G), is shorter than the timescale found in the longest lifetime of stacked nucleosomes (32), which was reported to be in the order of 100 ms (17). We also observed that the timescale of relaxation was slower for chromatin arrays containing acetylation. Together, these results suggest that the constructed 96-mer nucleosomes were fluctuating freely in a histone mark density-dependent manner, without forming aggregates.

Physical model explains the relationship between fluctuation amplitude and relaxation timescale

We found that the relaxation timescales of the chromatin fluctuations were proportional to the cube of their spatial extent (Fig. 2G). This cubic relation suggests that the dynamics of our reconstituted chromatin is consistent with the Zimm model (33, 34), which accounts for hydrodynamic interactions in polymer dynamics. The Zimm model predicts that the slowest relaxation time τ follows $\tau \propto \eta R^3/k_B T$, where R is the root mean squared end-to-end distance, η is the solvent viscosity, k_B is the Boltzmann constant, and T is the temperature.

For 25° to 30°C water, the Zimm model for a tethered chain predicts $R^3/\tau \approx 4.27$ to 4.77 $\mu\text{m}^3/\text{s}$. Although there is ambiguity in the prefactor in this theory [see Supplementary Methods and fig. S7 (A and B)], the order matches with the slope yielded from experimental

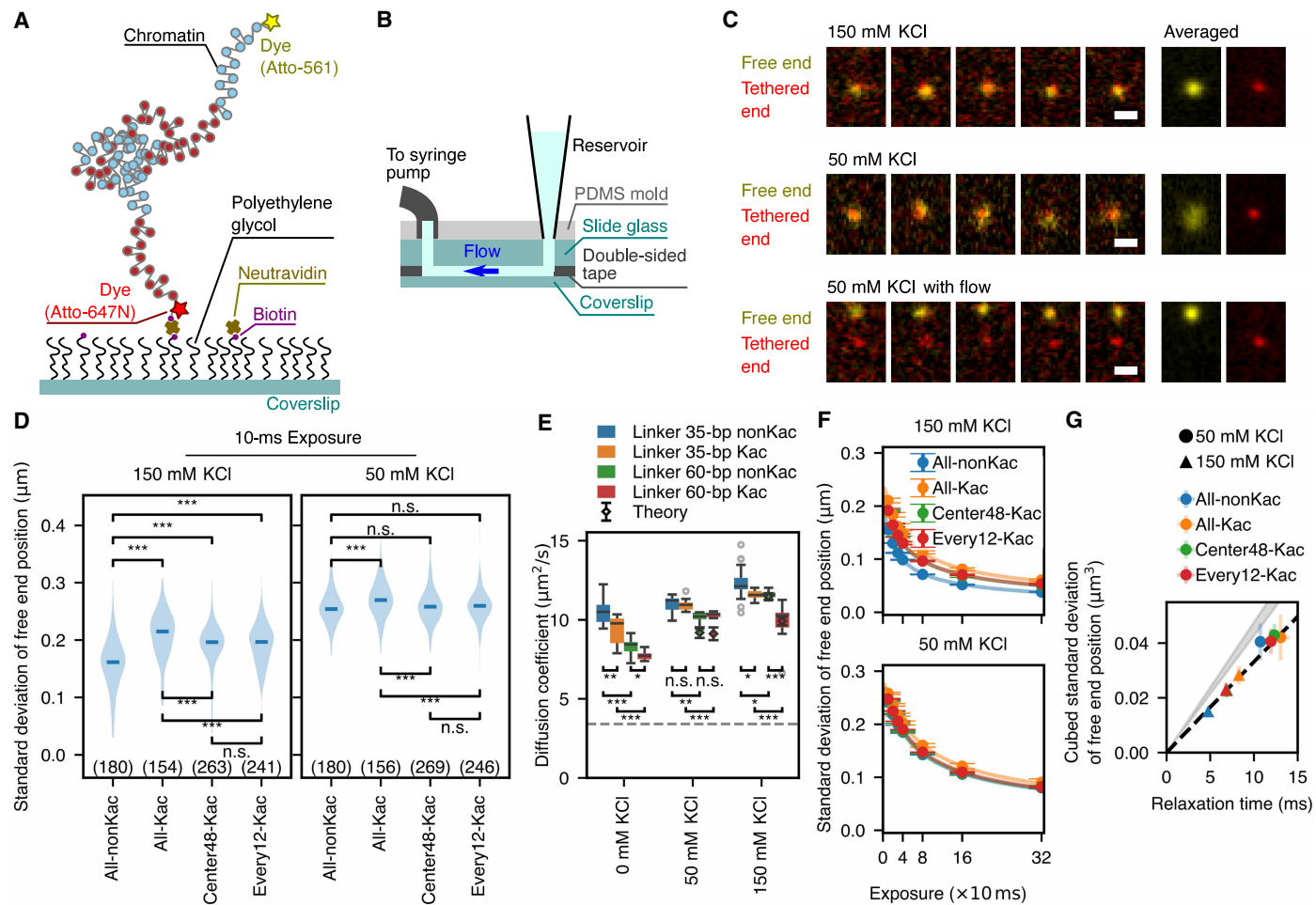


Fig. 2. Single-molecule microscopy shows histone modification-dependent fluctuations. (A) Schematic of the single-molecule observation of a 96-mer array. (B) Design of the chamber. PDMS, poly(dimethylsiloxane). (C) Montage of the fluorescent probe observations. Scale bars, 1 μm . (D) Extent of fluctuation for a single frame (10-ms exposure) measured from the fluctuation amplitude of the free ends. The numbers in parentheses indicate the number of analyzed spots. (E) Diffusion constant of the 12-mer arrays at 30°C measured by dynamic light scattering (DLS). The gray dashed line indicates the value without the hydrodynamic interaction. The values from bootstrap replicates (10 per observation; see Supplementary Methods) for each condition are summarized as a box plot; The box extends from the first to third quartile of data, with the middle line indicating the median. The whiskers extend from the box to the furthest data point within 1.5 times the interquartile range. The gray circles indicate the outliers. The theoretically estimated values are shown by the square symbols with error bars (see Supplementary Methods). (F) The median value of the extent of fluctuation with varied exposure time and the theoretical fits. The error bars represent the bootstrap SDs for the median value estimation. (G) Spatial extent of fluctuation in the zero-exposure limit plotted with respect to the relaxation time. Circle: 50 mM KCl, triangle: 150 mM KCl. The error bars represent the combined bootstrap SDs of two replicates. The gray shaded area represents the Zimm model prediction for the tethered chain setup, using the viscosity of water between 25° and 30°C. For (D) and (E), the asterisks indicate the statistical significance of the Mann-Whitney test adjusted by the Benjamini-Yekutieli method: “**,” “***,” and “****” correspond to statistical significance with $P < 0.05$, $P < 0.01$, and $P < 0.001$, respectively. “n.s.” means not significant.

data, $3.3 \pm 0.1 \mu\text{m}^3/\text{s}$ (Fig. 2G). Several factors may contribute to the quantitative difference between the simple theory’s prefactor and the experiment. These include deviations from the idealized bead-spring model assumptions for a complex nucleosome array, potentially increased local viscosity near the coverslip surface (35), and inherent uncertainties in applying the specific preequilibrium Zimm model prefactor to this tethered chain configuration.

As an independent measurement, we observed that the diffusion of 12-mer nucleosomes was faster than what is estimated using the monomer diffusion coefficient (36) without accounting for hydrodynamic interactions. By constructing 12-mer nucleosomes with different linker DNA lengths (30 to 60 bp), we further observed that

the diffusion constant significantly increased for shorter linker nucleosomes (Fig. 2E and fig. S8). The diffusion coefficients theoretically estimated from the Zimm model, assuming the Kuhn length as $R_{96}/\sqrt{96}$ and the end-to-end distance for 12-mers $\sqrt{12/96} \times R_{96}$, where R_{96} is the measured end-to-end distance of the 96-mer array, were consistent with the experimentally measured diffusion coefficients at 150 mM KCl (Fig. 2E; see Supplementary Methods). The estimated Kuhn lengths were 25 nm for the nonacetylated array and 31 nm for the acetylated array. With a linker DNA length of 21 nm, the increased Kuhn length upon acetylation suggests a relatively stronger repulsive interaction between next-nearest neighbor nucleosomes (separated by two linkers), resulting in a stiffer chain.

Nucleosome contact frequency decays with power law consistent with Gaussian chain

To further probe the structural changes associated with histone modification patterns, we reconstituted nucleosome arrays using DNA with linker-barcode arrays to measure the contact frequency of the nucleosomes by the sequencing-based chromosome conformation capture method (37), which we call *in vitro* Hi-C (Fig. 3, A and B). We first confirmed that the basic properties of the nucleosome arrays such as nucleosome occupancy, linker accessibility, and ligation order did not change because of the barcodes (figs. S1, D to I, and S2, D to J). Next, we optimized the fixation, digestion, and ligating steps for the barcoded 601 array from the method proposed for *in vitro* reconstituted yeast chromatin (Supplementary Methods and fig. S9) (38). The optimized protocol obtains a high yield of contacts between nonadjacent regions within the same molecule while suppressing nonspecific contacts quantified by the intermolecular contacts (Fig. 3C, fig. S10A, and Materials and Methods).

For both the nonacetylated and acetylated 12-mer arrays, we found the contact frequency decayed with genomic distance following a power-law scaling consistent with an exponent near -1.5 (Fig. 3D and fig. S10B), a behavior characteristic of the Gaussian chain model. Despite this similar overall scaling exponent, the decay of contact frequency initiated from a shorter distance in the acetylated sample, resulting in a substantially decreased number of contacts for longer distances (see Materials and Methods).

Using the single-nucleosome resolution of the barcodes, we further dissected the contact frequency in the different orientations

(Fig. 3E), inspired by the method used in (39). The result shows that the orientation dependence quickly decays and becomes indistinguishable beyond around the 5-mer distance (Fig. 3F and fig. S10, C and D), suggesting that there is no canonical structure in our 12-mer samples (40), such as 30-nm fibers that have been observed for arrays with linker histone proteins or shorter linker length (18, 41–44). This result is consistent with there being no evidence of stacked structure observed in our AFM observation, as well as in the timescale of single-molecule fluctuations.

Contact pattern of ligated chromatin depends on the histone modification pattern

Next, we conducted the conformation capture experiment using the longer ligated chromatin, to seek whether heterogeneous acetylation patterns alone can induce domain-like organization. By this method, we detected contacts up to distances of more than 60-mers (around 12 kb) at significant levels beyond the interarray contacts. The contact map of the heterogeneous chromatin, the Every12-Kac arrays and Center48-Kac arrays, were clearly distinct (Fig. 4A). This difference in the large-scale contact patterns appears linked to modification-specific effects at shorter ranges. Specifically, we observed a lower measured contact frequency between pairs of acetylated regions (Kac-Kac) compared to pairs of nonacetylated regions (nonKac-nonKac) located at the same genomic separation within the heterogeneous arrays (Fig. 4B). This suggests that acetylation directly alters the measured proximity between nucleosomes, potentially reflecting a combination of reduced intrinsic attraction and/or

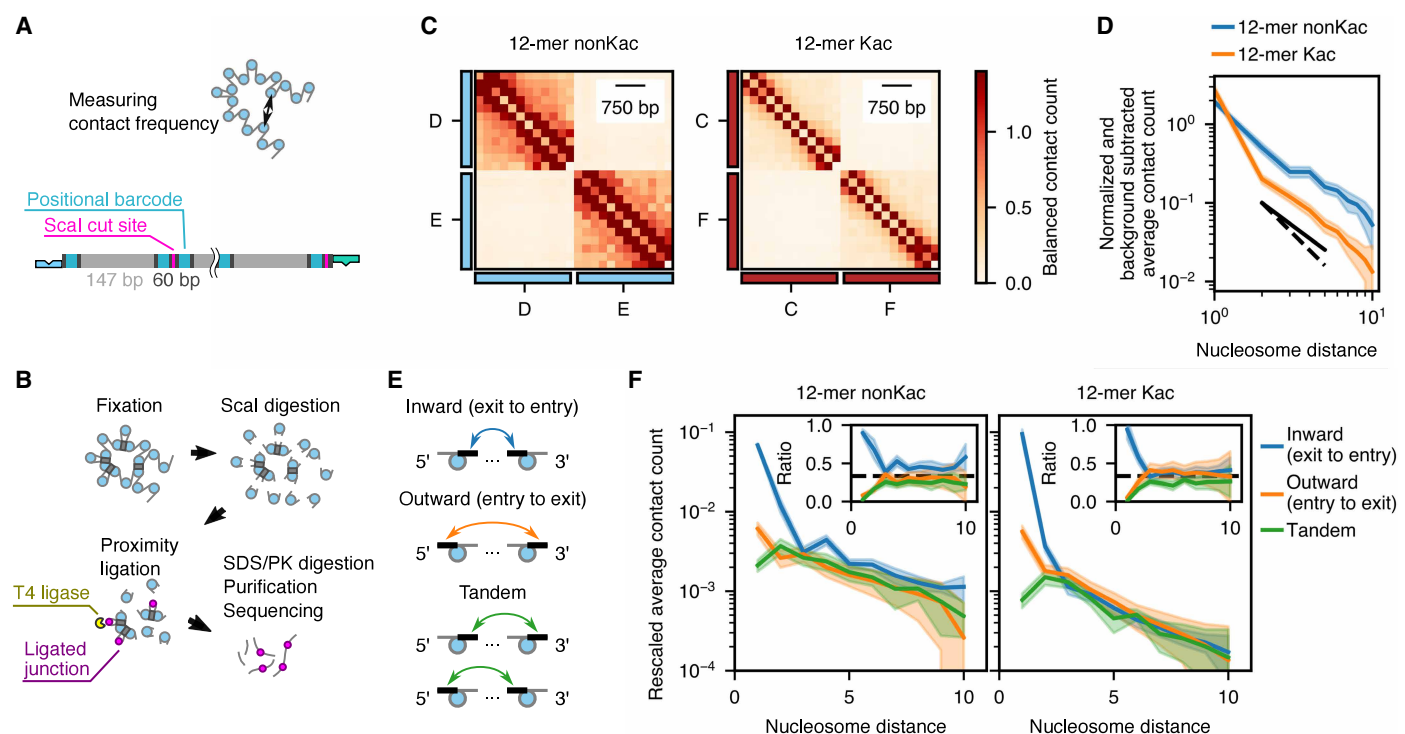


Fig. 3. In vitro contact maps of reconstituted 12-mers. (A) Schematic of the experiment and design of the barcoded 12-mer arrays. (B) Illustration of the protocol. (C) Contact map obtained from the mixed 12-mers with distinct barcodes. The contact is balanced and normalized so that the average contact frequency is 1. (D) Contact frequency as a function of the nucleosome position. The shaded area represents the uncertainty (twice the SEM). The black solid and dashed lines are the guide for the eye with the exponents of -1.5 and -2 , respectively. (E) Schematic of the contact orientation. (F) Contact frequency classified by orientation as a function of the nucleosome position distance. The shaded area represents uncertainty (twice the SEM). The dashed lines are at ratio = 1/3.

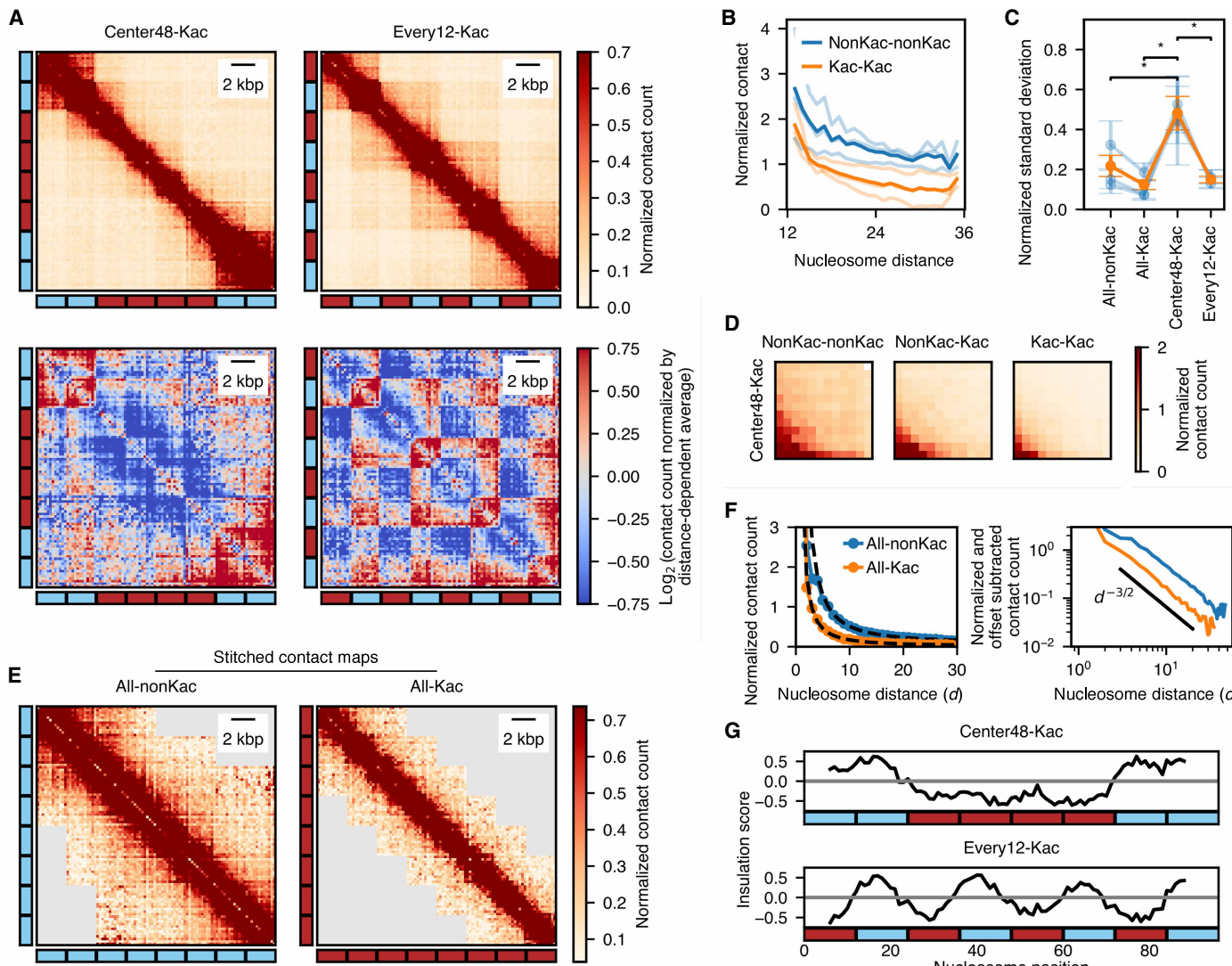


Fig. 4. In vitro contact maps of reconstituted chromatin with heterogeneous histone modifications. (A) Contact map of the ligated nucleosome arrays (96-mers as the largest) with inhomogeneous patterns. Top: Raw contact counts normalized to the total count. Bottom: The logarithm of counts normalized by the distance-dependent average. (B) Average number of contacts between the second adjacent 12-mer regions for the Every12-Kac arrays as a function of the nucleosome distance. The light-colored lines are the replicates, while the dark-colored lines are the average. The total average values were significantly different by $P < 10^{-4}$ in the Mann-Whitney test for all individual replicate pairs as well as their average. (C) SD of the median contact between the adjacent 12-mer regions, rescaled by the mean contact frequency of all pairs. ** indicates the statistical significance in the Brown-Forsythe test with $P < 0.05$. The light blue symbols are replicates, while the solid orange symbols are the average, both with SD as the error bars. (D) Accumulated contact frequency between adjacent 12-mer regions for the Center48-Kac arrays. (E) Stitched contact map of the homogeneous arrays. The gray area shows regions with nonsignificant contact counts in which more than 10% of the bins have negative contacts after background subtraction. (F) Top: Contact frequency as a function of the nucleosome position distance in the stitched contact map. The dashed lines are the power-law fits with the exponent of -1.5 with offset. Bottom: The offset-subtracted contact frequency as a function of the nucleosome position distance. The black solid line is the guide for the eye with the exponent of -1.5 . (G) Insulation score for the stitched inhomogeneous arrays with a window size of 4.

a decreased efficiency in capturing Kac-Kac interactions via the Hi-C cross-linking and ligation process itself due to local structural or dynamic changes. Consistently, the fluctuations in the contact frequency of the proximal 12-mers were larger than the homogeneous arrays in the Center48-Kac arrays (Fig. 4C and fig. S11A), reflecting the inhomogeneity of intramolecular contacts existing specifically in the Center48-Kac arrays. The contact frequency between the non-Kac regions was the highest, whereas the contact between Kac regions was less frequent (Fig. 4D and fig. S11, B to D).

For the uniformly patterned arrays (fig. S11E), we asked how the contact frequency decays for longer distances than 12-mers and how the decay depends on acetylation. We reconstructed the contact map at the 96-mer scale (Fig. 4E), assuming that the polymer structure is translationally symmetric and that the contact map of subregions will be the same irrespective of it being probed in a large or small array (see Materials and Methods). Calculating the distance dependence of the contact frequency, we again obtained results consistent with a Gaussian chain model, where the frequency decays

with a power-law exponent close to -1.5 (Fig. 4F and fig. S11F). While the measured scaling exponent appeared largely independent of the uniform modification state in this regime, the absolute contact frequency was consistently around two- to fourfold lower for the acetylated array.

By calculating the insulation score (45) for the reconstructed contact map of inhomogeneous arrays, we further confirmed the structural heterogeneity in the Center48-Kac and Every12-Kac arrays (Fig. 4G and fig. S11G). The score was consistently negative around the acetylated regions, indicating that the acetylated regions act as insulating boundaries. These results indicate that the heterogeneous histone modification patterns on the chromatin array are sufficient to induce contact domains (1), driven solely by the differential compaction and nucleosome contact frequencies between modified and unmodified regions, in the absence of other factors.

DISCUSSION

We constructed gene-scale chromatin arrays with designed histone modification patterns, demonstrating that acetylation alone, by altering physical interactions at the monomer-interaction level, can drive pattern-dependent macroscopic changes in chromatin architecture and dynamics. Notably, the acetylation-induced spreading became prominent at the 96-mer scale compared to the 12-mer scale (fig. S6), indicating a length-dependent influence. Furthermore, heterogeneous patterns were sufficient to induce distinct structural domains *in vitro*.

The observed relationship between the spatial extent and the timescales of fluctuation is consistent with the Zimm model of polymer dynamics (33, 34). This agreement indicates that hydrodynamic interactions, mediated by the solvent, are crucial determinants of chromatin fiber dynamics at these length scales and should be considered for accurate biophysical modeling. The estimated values of the Kuhn length are consistent with the value previously reported in an experiment pulling a chromatin fiber (46) and larger than the linker DNA length, reflecting the fact that the linker exit angles are not random as in the simplified beads-on-a-string model.

While the single-molecule dynamics followed the Zimm model predictions, our *in vitro* Hi-C experiments probing the ensemble-averaged structure revealed an intriguing scaling exponent of approximately -1.5 , suggestive of a Gaussian chain-like conformation (34), even for the more compact nonacetylated arrays. This apparent Gaussian behavior, as well as the orientation-independent contacts observed for 12-mers, is consistent with the previous observations that polynucleosomes with long linker length (nucleosome repeat length = 197 bp) without linker histone protein show an irregular structure (42). This structure is distinct from the regular helical 30-nm fibers reported in reconstituted chromatin with linker histone H1 or shorter linker length supplied with magnesium ion (18, 41–43).

To observe a scaling exponent of -1.5 at this length scale, a realistic polymer model would require carefully tuned monomer-monomer interactions that remain effectively neutral. This exponent is often associated with the more open chromatin structure observed in yeast (47), rather than the compact organization typical of mammalian interphase chromatin (48), suggesting that our *in vitro* system captures certain features of an open state, even for nonacetylated arrays under physiological salt conditions. However, Micro-C data from mammalian cells (49) also show an exponent near -1.5 in the sub-10-kb range before transitioning to a region closer to -1 , irrespective of the compartment (fig. S12). This implies that a self-organizing

mechanism may keep nucleosome-nucleosome interactions near neutrality at the sub-10-kb scale, largely independent of salt conditions and histone modifications.

The apparent Gaussian-like scaling observed in our Hi-C data presents an interesting puzzle, contrasting with clear acetylation-dependent changes in dynamics, contact probabilities, and effective Kuhn length. While the increased stiffness (larger Kuhn length) accompanying acetylation contributes to larger end-to-end fluctuations and reduces overall long-range contact frequency, it does not fully explain the lower contact probability measured specifically between acetylated pairs versus nonacetylated pairs at equivalent separations (Fig. 4B). This suggests an additional mechanism to stiffness change that will lead to a differential capture efficiency in the Hi-C protocol, such as acetylation locally weakening nucleosome interactions, reducing cross-linking/ligation success for distal acetylated pairs. Thus, the observed contact patterns likely stem from both altered chain stiffness and modification-specific effects on interactions changing capture efficiency. The persistence of the -1.5 scaling exponent may indicate that these combined factors, while substantially modulating contacts and overall interaction frequencies, do not markedly alter the global conformational scaling within our probed range.

These acetylation-induced changes in chromatin stiffness and local/distal interactions are notable because they intrinsically modulate the polymer's physical properties. Such alterations are expected to influence the mechanical response of chromatin under physiological forces and could affect gene regulation by altering the potential accessibility and dynamic behavior of regulatory regions. In our specific *in vitro* assay using methyltransferase, we did not detect significant differences in accessibility between acetylated and nonacetylated arrays (Fig. 1G and fig. S3). This finding suggests that within this purified system, the direct effects of H4 acetylation—increasing chain stiffness and weakening distal contacts—are not sufficient on their own to cause changes in DNA accessibility detectable by this enzymatic probe over the 96-mer length scale. Additional factors present *in vivo*, potentially recruited by or interacting differently with chromatin, are likely essential for mediating the substantial accessibility.

The chromatin-only approach establishes a baseline for understanding the contribution of histone modifications to the higher-order structure, which has previously been modeled with polymer physics with different levels of detail (50–53). Future investigations incorporating other binding components and modifications, such as H1, bromodomain-containing proteins with various tail acetylations, HP1 with H3K9 methylation, and DNA binding factors, will be essential to further elucidate the complex relationship between epigenetic marks, chromatin organization, and, ultimately, genome function. The influence of the linker DNA length, which affects the polymer property as well as the histone interactions (19, 42, 54) can be further investigated using our arrays with distinct linker lengths. This controlled *in vitro* system allows us to systematically address the extent to which specific modifications and interacting components contribute to the diverse structural and functional landscapes of chromatin.

MATERIALS AND METHODS

DNA design and preparation

All LB plates and medium were supplemented with ampicillin (0.1 mg/ml). Buffers recommended by New England Biolabs were

used for the restriction enzyme digestion and ligation reactions, if not specified.

For the nonbarcoded arrays, DNA sequences contain 12 repeats of the Widom 601 nucleosome positioning sequence (25) separated by a 61-bp linker DNA. The two ends of the whole 12-mer sequence were designed to be cut by the BglII restriction enzyme, so that the 3-bp sticky ends differ from each other by at least 2 bp, except for the 5' end of A and the 3' end of H, which ligate to the short labeled oligonucleotides (Fig. 1B). The transformed *Escherichia coli* cells (New England Biolabs, C2987) were plated on LB agar plates and incubated overnight at 37°C. Colonies were picked and grown in 3-ml LB medium for 7 to 9 hours. The cells were then transferred to 2.5-liter LB medium and cultured overnight at 37°C. Plasmids were extracted using the QIAGEN Plasmid Giga Kit (QIAGEN, 12191) and digested with BglII (0.1 to 0.4 U/μg; New England Biolabs, R0143) to excise the insert from the backbone, and EcoRV-HF (0.15 to 0.2 U/μg; New England Biolabs, R3195) to digest the backbone into 200- to 300-bp fragments for two to three overnights. The 12 × 601 fragments were then purified by two rounds of polyethylene glycol precipitation [4.33% polyethylene glycol 6000 (Nacalai Tesque Inc., 28254-85) and 0.595 M NaCl (Nacalai Tesque Inc., 31320-05) final] followed by ethanol precipitation. The DNA was then resuspended in tris-EDTA buffer (Nacalai Tesque Inc., 32739-31) and stored at –20°C.

The plasmids with the barcoded arrays were constructed to have 60-bp linker DNA, including two 17-bp barcodes, with a digestion site by ScaI in between (Fig. 3A). The plasmids with 30-, 35-, 40-, 45-, and 50-bp linker DNA was similarly prepared for Fig. 2E and fig. S8. The 12 × 601 fragments were prepared similarly to the nonbarcoded plasmids.

End labeling of A and H fragments

Following a method in (17), modified oligonucleotides 5'-Ph-TAGT CTGC(T*)CAGATATCGTCG-Biotin-triethyleneglycol-3' and 5'-C ACAGCTG(T*)CTGAG-3', where T* represents the amine-linked dT with the C6 linker (purchased from Merck), was labeled by Atto647N-NHS ester (ATTO-TEC GmbH, AD647N-31) and Atto565-NHS ester (ATTO-TEC GmbH, AD565-31), respectively. Those fragments were annealed to the complementary oligonucleotides and ligated to the "A" and "H" arrays, respectively. See Supplementary Methods for details.

Protein expression and purification

Recombinant histone H4 with or without residue-specific acetylation at K5/K8/K12/K16 was synthesized by genetic code reprogramming in a coupled transcription-translation cell-free system. The cDNA containing human histone H4 with or without the codons of K5/K8/K12/K16 replaced with the TAG triplets and a terminal TAA stop codon were subcloned into a pCR2.1-TOPO plasmid (Thermo Fisher Scientific, K450002). The unmodified and K5/K8/K12/K16-tetra-acetylated histone H4 (H4K5K8K12K16ac) proteins were designed to have an N-terminal histidine-rich affinity tag (N11; MKD-HLIHNHHKHEHAHA) followed by a Tobacco Etch Virus (TEV) protease recognition sequence (EHLYFQ), which has no additional N-terminal sequence after cleavage by TEV protease. Protein synthesis in the cell-free system was performed as described (55), using the subcloned plasmids, with a 9-ml reaction solution dialyzed against a 90-ml external feeding solution at 37°C for 6 to 18 hours. Precipitates of the unmodified H4 and H4K5K8K12K16ac were separated by centrifugation for 30 min at 30,000g at 4°C.

Unmodified human histones were recombinantly expressed in *E. coli*. The cDNA containing human histone H2A type 1-B/E, H2B type 1-J, and H3.1 were subcloned into a pET15b-derived plasmid containing an N-terminal 6 × His tag (MGSSHHHHHSSG) in which the thrombin cleavage site of pET15b (Merck Millipore, 69661) was replaced by the TEV protease recognition sequence. The H2B expression construct contains a glycine residue at the end of the TEV protease recognition sequence which remains after cleavage by TEV protease. The H2A and H3 expression constructs have no additional N-terminal sequence after cleavage by TEV protease. These histones were expressed in LB broth of *E. coli* BL21 (DE3) cells at 37°C. Induction of the recombinant histone proteins, separation of their precipitates, and preparation of the unmodified and H4K5K8K12K16ac-containing histone octamers in vitro were performed essentially as described (55).

Reconstitution of 12-mer nucleosome arrays

The template DNA hosting 12 repeats of the 601 sequence was mixed with the reconstituted histone octamer and short octamer sink DNA fragments with the molar ratio to the 601 sequences of 1.2 and 5/12 for the nonbarcoded arrays and 1.1 to 1.2 and 1/3 to 1/2 for the barcoded arrays, respectively. The reconstitution was performed by the salt-gradient dialysis from 2 M KCl to 250 mM KCl over 17 hours and then to no-salt buffer [10 mM tris-HCl (pH 7.5) and 1 mM EDTA] followed by purification by 10 to 40% sucrose gradient ultracentrifugation. Reconstituted chromatin was routinely checked by the band shift assay in agarose gel electrophoresis and polyacrylamide gel electrophoresis (PAGE) after ScaI digestion in the ScaI cut buffer [10 mM tris-HCl (pH 7.5), 0.5 mM MgCl₂, and 50 mM NaCl]. See Supplementary Methods for details.

Ligation of 12-mer arrays into 96-mer nucleosome arrays

The frozen stocks of the 12-mer arrays were quickly thawed by hand warming and then placed on ice. The equal amount of 12-mer arrays (1 to 2.5 μg for each) was mixed and purified again by 10 to 40% sucrose gradient. The arrays were then further concentrated to 0.4 to 1.1 μg/μl by centrifugation in Vivacon 500 100 kDa (Sartorius, VN01H42). The 12-mer mixture was ligated in the final concentration of 0.3 to 0.52 μg/μl (fixed to the same concentration for the same batch) with T4 DNA ligase (133 U/μl; New England Biolabs, M0202M) and 50 mM tris-HCl (pH 7.6), 2 mM ATP (New England Biolabs, P0756S), 3 mM MgCl₂, 10 mM dithiothreitol (DTT), and 0.01 mg/ml BSA (bovine serum albumin; New England Biolabs, B9200S) at 16°C overnight.

The ligated products were then washed three times with TEN 50 buffer [10 mM tris-HCl (pH 7.5), 1 mM EDTA, and 50 mM NaCl] in the 100-kDa molecular weight cutoff (MWCO) Amicon Ultra centrifugal filter at 14,000g for 3 min (15 min for the last wash) and once with the final buffer {no-salt buffer for the nonbarcoded array and the TE0.1D buffer [10 mM tris-HCl (pH 7.5), 0.1 mM EDTA, and 1 mM DTT] for the barcoded array} for 15 min. The final ligated product was stored at 4°C for a maximum of 6 weeks (nonbarcoded arrays) and for 7 weeks (barcoded arrays) with little nucleosome dissociation (verified by ScaI digestion and native PAGE as described).

The ligated arrays were checked by native PAGE after ScaI digestion as described (fig. S2, A, D, and E). The ligation was confirmed by digesting the ligated product by SDS/PK [proteinase K (0.5 mg/ml; FUJIFILM Wako Pure Chemical Corp., 169-21041 or 166-28913), 10 mM tris-HCl (pH 8.0), 40 mM EDTA, and 0.125% SDS] and

performing electrophoresis with 0.3% agarose in 1× tris-acetate-EDTA (Fig. 1D and fig. S2, F and G).

Validation of the ligation order by nanopore sequencing

SDS/PK-digested samples were purified using Ampure XP beads (Beckman Coulter, A63880) and sequenced using the Flongle or MinION flow cell (Oxford Nanopore Technologies). The input amount, purification condition, sequencing kit, and flow cell are summarized in table S1.

Accessibility assay for reconstituted chromatin

Chromatin samples and equimolar mixture of the bare DNA fragments were respectively mixed with 50 mM tris-HCl (pH 7.5), 150 mM KCl, 1 mM MgCl₂, 0.1 mg/ml BSA (New England Biolabs, B9000S), 2.4 mM S-adenosylmethionine (New England Biolabs, B9003S), and 0.645 U of EcoGII methyltransferase (New England Biolabs, M0603S) at the concentration of 4 ng/μl in the final volume of 33 μl and incubated at 37°C. The reaction was quenched by taking 10 μl of the sample after 10 and 40 min and adding 2.5 μl of 6× SDS/PK buffer [60 mM tris-HCl (pH 8.0), 240 mM EDTA, and 3% SDS], 1.5 μl of proteinase K (5 mg/ml), and 1 μl of ultrapure water and incubating at 65°C (lid 75°C) for more than 2 hours. Ten microliters of the samples was immediately quenched after mixing (“0 min” sample). DNA was purified by two rounds of purification by the Serapure magnetic beads ($\times 1.8$ volume to the sample; see Supplementary Methods), processed using the library preparation kit SQK-NBD114.24 (Oxford Nanopore Technologies), and sequenced using the MinION R10.4 flowcell (Oxford Nanopore Technologies, FLO-MIN114).

Observation by AFM

For the nucleosome counting (Fig. 1 and figs. S1 and S4), samples were diluted to 0.25 to 1 ng/μl and fixed with 0.1% glutaraldehyde (Nacalai Tesque Inc., 17003-92) or 0.1% formaldehyde (FUJIFILM Wako Pure Chemical Corp., 064-00406) and 0.05% glutaraldehyde on ice for 10 to 30 min. For the size measurement (fig. S6), ≈20 ng of the 96-mer samples (barcoded, batch 1) was diluted in the H30D buffer, and the equivalent volume of H30K150 (salt2X) buffer [30 mM Hepes-KOH (pH 7.5), 300 mM KCl, and 1 mM DTT] or H30K150M1 (salt2X) buffer [30 M Hepes-KOH (pH 7.5), 300 mM KCl, 2 mM MgCl₂, and 1 mM DTT] was added and mixed by tapping.

The samples were mounted on a mica plate coated by poly-L-ornithine solution (Sigma-Aldrich, P3655) and observed with the Innova atomic force microscope (Bruker) using the SNL10-C probe in the tapping mode with the pixel size of 9.77 nm (size measurement) or 1 to 2 nm (nucleosome counting). For Fig. 1 (H and I) and fig. S4 (A and E to M), chromatin was elongated by flow in the mounting step. See Supplementary Methods for details.

Single-molecule observation by fluorescence microscopy

For the chamber construction for single-molecule imaging, we followed a protocol in (17) with modifications. Imaging buffer (IB) was prepared according to (17, 56). See Supplementary Methods for details.

The chambers were washed sequentially with 200 μl of NaB buffer (pH 8.5) and T50 (pH 8.0) buffer [10 mM tris-HCl (pH 8.0) and 50 mM NaCl] and incubated with 80 μl of NeutrAvidin (0.25 mg/ml; Thermo Fisher Scientific, 31000) in T50 (pH 8.0) for 15 min. The chambers were then washed again with 200 μl of T50 (pH 8.0), 1 ml of T150 [10 mM tris-HCl (pH 7.5) and 150 mM NaCl], 200 μl of T50

(pH 7.5) buffer [10 mM tris-HCl (pH 7.5) and 50 mM NaCl], and lastly with 100 μl of IB (50 mM KCl). Chromatin samples, diluted to 100 pM in IB (50 mM KCl), were injected into the chambers and incubated for 2 to 5 min. The chambers were then washed twice with 50 μl of IB (50 mM KCl) and observed sequentially in (i) IB (50 mM KCl) without flow, (ii) IB (150 mM KCl) without flow, (iii) IB (50 mM KCl) without flow, and (iv) IB (50 mM KCl) with flow (200 μl/min). After sample injection, buffer exchange was performed at the rate of 25 μl/min. One hundred microliters of each buffer was injected into the reservoir, from which 50 μl was introduced into the chamber by syringe pump aspiration.

The sample was observed with a microscope equipped with the objective lens UPlanApo 60×/1.50 Oil HR TIRF (Olympus), epi-illumination by the laser light from OBIS 561-nm LS (Coherent) and OBIS 637-nm LX (Coherent), and the Multisplit V2 (Teledyne Photonics) for simultaneous dual-color observation by the highly inclined and laminated optical sheet microscopy (57). The laser intensities were 10 to 20 mW (561 nm) and 10 mW (640 nm), respectively. Fluorescence images were captured using a Prime BSI scientific Complementary Metal–Oxide–Semiconductor (sCMOS) camera (Teledyne Photonics) in the Correlated Multi-Sampling mode and 10 ms exposure. The pixel size was 0.109 nm. We took movies of 100 frames in 25 fields of view with 53.76 μm by 53.76 μm area for each condition, yielding 1000 to 4000 fluorescent spots in total. The microscope, syringe pumps, and valves were controlled by Micro-Manager (58) and Pycro-Manager (59). See Supplementary Methods for details. Two replicate experiments were performed, and the results are reported in Fig. 2 and fig. S5.

Diffusion coefficient measurement of 12-mer dynamic light scattering

Dynamic light scattering (DLS) measurements were performed using a DynaPro PlateReader II (Wyatt Technology) with a laser wavelength of $\lambda_{\text{DLS}} = 830$ nm and a scattering angle of $\theta_{\text{DLS}} = 158$ deg. The 12-mer samples were dialyzed against H30D buffer [30 mM Hepes-KOH (pH 7.5) and 1 mM DTT], and 10 μl of each sample at a concentration of 10 to 20 ng/μl was mixed with an equal volume of either H30D buffer, H30K50 (salt2X) buffer [30 mM Hepes-KOH (pH 7.5), 100 mM KCl, and 1 mM DTT], or H30K150 (salt2X) buffer [30 mM Hepes-KOH (pH 7.5), 300 mM KCl, and 1 mM DTT] to yield final KCl concentrations of 0, 50, and 150 mM, respectively. The intensity autocorrelation function $g(t)$ was fitted using two approaches: (i) the CONTIN algorithm (60–62) and (ii) the non-negative least squares (NNLS) method, which minimizes the regularized cost function $\left\| \{C(t_i) - g(t_i)\}_i \right\|_2 + \alpha \left\| \left\{ \sum_j L_{ij} x_j \right\}_i \right\|_2$, where $C(t) := \sum_j x_j \exp\left(-\frac{t}{\tau_j}\right)$ is the target function, $\{t_i\}_i$ is the discretized time, and $L_{ij} = \delta_{ij} - \delta_{ij+1}$. The τ_j value at the peak of x_j within the range of $80 \leq \tau_j \leq 200$ was used as the estimated decay time τ . Acquisitions that produced correlation functions deviating markedly from typical behavior or replicates for which the estimated τ varied substantially depending on the fitting method (CONTIN or NNLS) and regularization parameter α were excluded from further analysis. The final estimate used the NNLS with $\alpha = 10^{-3}$. The diffusion coefficient D was estimated by $D = 1/(2\tau q^2)$, where $q = \frac{4\pi n}{\lambda_{\text{DLS}}} \sin\left(\frac{\theta'_{\text{DLS}}}{2}\right)$, $n = 1.33$ is the water refractive index, and $\theta'_{\text{DLS}} = 150$ deg is the scattering angle in the solution. One to three wells per condition

were analyzed; for one well, 10 bootstrap replicates were used to generate the plots and perform the statistical tests.

In vitro Hi-C experiment

The chromatin conformation capture experiment was performed similarly to (38) with major differences in fixation, digestion, proximity ligation, and linker sequence enrichment. For the detailed protocol, see Supplementary Methods.

In short, the samples were fixed in 30 mM Hepes-KOH, 150 mM KCl, and 1 mM DTT by 0.5% formaldehyde and 0.1% glutaraldehyde or 1% formaldehyde. For 96-mer samples, a Kac 12-mer array with independent barcodes was spiked in to estimate the background level at the analysis. The reaction was quenched by glycine, and the samples were dialyzed against the no-salt buffer. The fixed samples were digested by ScaI in the ScaI cut buffer, and 4 to 16.8 ng of the sample was proximity ligated in 0.125× T4 DNA ligase buffer [50 mM tris-HCl (pH 7.5), 10 mM MgCl₂, 1 mM ATP, and 10 mM DTT at 1× concentration; New England Biolabs, B0202S] with the presence of 1/250 volume of T4 DNA ligase (Takara Bio, 2011A) at the concentration of 1.05 to 4.2 pg/μl at 37°C for 20 min. Proximity ligated samples were deproteinized by adding SDS/PK buffer [10 mM tris-HCl (pH 8.0), 40 mM EDTA, and 0.5% SDS at final concentration] and proteinase K (0.5 mg/ml at final concentration) and incubating at 65°C for 2 hours. DNA fragments were concentrated with 2-butanol (Nacalai Tesque Inc., 06102-45) and purified using the FastGene Gel/polymerase chain reaction (PCR) extraction kit (Nippon Genetics Co. Ltd., FG-91202) with EconoSpin IIa columns (Ajinomoto Bio-Pharma Services, EP-11201). After excising the linker fragments by 2.5–10 U of NotI-HF (New England Biolabs, R3189S) and AvaI (New England Biolabs, R0152S), ligated linker fragments were enriched by size selection using Serapure (see Supplementary Methods) and Ampure XP beads.

The sequencing library was prepared from the linker-enriched samples using the NEBNext Ultra II DNA Library Prep Kit for Illumina (New England Biolabs, E7645S) and NEBNext Multiplex Oligos for Illumina (UDI UMI Adaptors DNA Set 1) (New England Biolabs, E7395S) with 13 to 19 cycles of PCR. The PCR cycle was determined for each library using 1/10 of the adaptor-ligated DNA as the template with the KAPA SYBR FAST qPCR Master Mix (Roche, KK4603) by taking the threshold cycle (*C_t*) that reaches 1/2 of the maximum intensity and subtracting 2 cycles (*C_t*–2 cycles). The entire amount of the remaining adaptor-ligated DNA was used for library amplification. Library pooling was performed ensuring that the linker sequence (observed as a band at 210 bp) was present in equimolar concentration. Sequencing was performed on the NextSeq 2000 sequencer (Illumina) using the P1 flow cell in paired-end mode: 55 cycles for each paired-end read with 20 cycles for index 1 including 12-base unique molecular identifiers (UMI) and 8 cycles for index 2. For the 96-mer samples, three or four replicate experiments were performed, and the results are reported in Fig. 2 and fig. S11.

Analysis of AFM data for size measurement

The raw “TOPO” signal recorded for the forward and backward paths was corrected, aligned, and background-subtracted (see Supplementary Methods). The chromatin blobs were found by thresholding the images smoothed by the median filter (3 pixel by 3 pixel footprint) at 0.25 nm, removing objects smaller than 2 pixels and applying the binary closing operation. The histogram for the

particle volume (fig. S6B) was smoothed by the Savitzky-Golay filter, and a linear function was extrapolated to the first three peak positions to find the particles with size close to (*n* × 12)-mer with *n* = 1, ..., and 8. The areas of the particles classified in each *n* were calculated to generate fig. S6 (C and D).

Analysis of nanopore sequencing data

To generate the plots in Fig. 1 and fig. S2, the nanopore sequence data were basecalled by the dorado basecaller (version 0.7.2+9ac85c6) (63) with the “sup” model and classified by the barcode using the “demux” command. Sequencing biases were calculated by dividing the number of sequenced base pairs for sequences whose length is in the range [(*n* – 0.5) × *L*, (*n* + 0.5) × *L*], where *n* = 1, ..., and 9 and *L* is the sequence length for a 12-mer array, by the background-subtracted intensity of the electrophoresis intensities in the corresponding bands (fig. S2C).

The linker sequences (barcoded arrays) and the junctions (ligated BglII sites, nonbarcoded arrays) were aligned to the reference sequences as described in Supplementary Methods. Using the aligned positions of the linker sequences, we aligned the whole sequences to the entire 96-mer array by offsetting the sequence position by the median of the difference between the expected and sequenced positions (Fig. 1E and fig. S2B). For Fig. 1F and fig. S2H, the histograms were corrected by weighting the reads by the estimated sequence bias (fig. S2C).

For the accessibility assay, the “sup,6mA” model was used to resolve the modified adenine bases. After aligning the sequences to the reference sequences by the “dorado align” command (Supplementary Methods), the frequency of the modified base occurrence was measured using the “pileup” command of modkit (version 0.3.1) (64). We calculated the accessibility score by subtracting the values for the 0-min samples from those for the 40-min samples and then dividing the values for the chromatin samples by those for the bare DNA samples. The score values smoothed by applying the rolling average of 10 rows were used to plot Fig. 1G and fig. S3.

Analysis of fluorescence microscopy data

Images were rescaled, preprocessed, and corrected for positional shifts as described in Supplementary Methods. Fluorescent spots were located in the temporally averaged images by using the Laplacian of Gaussian filter [skimage.feature.blob_log in scikit-image version 0.20.0 (65)] and associated in time (Supplementary Methods). Chromatin molecules that did not fluctuate after compaction or did not elongate with the applied flow were considered nonspecifically bound to the coverslip and filtered out by thresholding the Gaussian width (the SD of the fitted Gaussian function) at 50 mM KCl after compaction $\sigma_{50\text{ mM KCl}}$, the ratio of the Gaussian width at 50 mM KCl before and after compaction R_σ , and the elongation (distance between the center of the blobs before and after applying the flow) *E*. The blobs with $\sigma_{50\text{ mM KCl}} > 0.25 \mu\text{m}$, $1/1.2 < R_\sigma < 1.2$, and $E > 0.75 \mu\text{m}$ were used for further analysis (fig. S5, A to C).

The 28 pixel by 28 pixel small movies at the blob positions were exported and further analyzed. First, the images were averaged in time using the sliding window to create images with different exposure times. For each frame, the blob positions were defined as the centroid of the disk-shaped regions around the blobs, with the pixel values weighted by the background-subtracted intensity of the image (Supplementary Methods).

We fitted the median values of the SD of the centroid positions by a theoretical function $S(T) := \sqrt{\frac{2\beta^2\tau^2}{T} \left[1 - \frac{1-e^{-T/\tau}}{T/\tau} \right]}$, derived as the SD of the positions of a particle following the two-dimensional Ornstein-Uhlenbeck process, $dx = -xdt/\tau + \beta dW_t^x$ and $dy = -ydt/\tau + \beta dW_t^y$, averaged over time T corresponding to the exposure time (Fig. 2F and fig. S5E; see Supplementary Methods for derivation).

After fitting, we obtained the SD at the zero exposure limit and the correlation time as $\sigma := S(T \rightarrow 0) = \beta\sqrt{2\tau}$ and τ , respectively. Considering that we are observing the two-dimensional projected end positions, we defined the cubed SD of the free end position in Fig. 2G as $R^3 = (\sqrt{3/2}\sigma)^3$.

Analysis of in vitro Hi-C data

The contact maps were generated by locating the ScalI recognition sequence and finding the matching barcode sequences at the expected position (Supplementary Methods). The 12-mer contact maps (Fig. 3C and fig. S10A, extracted from the full contact map) were balanced by the Knight-Ruiz algorithm (66) in the finest resolution resolving all barcode positions. The elements at $(i, i+a)$ and $(i+a, i)$ ($a = 0, 1, 2, 3$ and $i = 1, \dots, N-a$, N is the matrix size) were not used for the balancing, since they are likely to be affected by the ScalI digestion bias. The background level for the 96-mer contact map was calculated by measuring the contact frequency to the spike-in Kac 12-mer array with independent barcodes. The background level was subtracted from the contact map. Stitching was performed for the 96-mer arrays (Fig. 4, E to G, and fig. S11, F and G) by first rescaling the diagonal 12-mer by 12-mer submatrices so that they have the same average contact frequency and then sequentially finding the optimal scale factor for other subcontact maps that minimizes the sum of the squared difference between adjacent regions.

Analysis of Micro-C data

The balanced Micro-C contact matrix at 1-kb resolution from (49) was retrieved as entry 4DNFINNZDDXV from the 4D Nucleome Data Portal (67, 68). Compartment annotations were obtained from entry 4DNFILGE5LQU. For fig. S12A, distance-dependent contact probabilities were calculated by averaging all contact counts within A-A and B-B compartment pairs. For fig. S12B, the local distance-dependent contact probability $C(i, d)$ was computed from the contact matrix C_{ij} as follows

$$C(i, d) = \frac{1}{N} \sum_{j \in I_N(i)} C_{j-d, j+d} \quad (1)$$

where the sliding window $I_N(i)$ is defined as $\{i - \lceil (N-1)/2 \rceil, \dots, i + \lfloor (N-1)/2 \rfloor\}$. A window size of $N = 20$ (20 kbp) was chosen. Last, the distance-dependent contact exponent at bin n was estimated by linear regression of $\log C(i, d)$.

Supplementary Materials

The PDF file includes:

Supplementary Methods
Figs. S1 to S12
Legends for tables S1 to S3
References

Other Supplementary Material for this manuscript includes the following:

Tables S1 to S3

REFERENCES AND NOTES

- J. R. Dixon, I. Jung, S. Selvaraj, Y. Shen, J. E. Antosiewicz-Bourget, A. Y. Lee, Z. Ye, A. Kim, N. Rajagopal, W. Xie, Y. Diao, J. Liang, H. Zhao, V. V. Lobanenkov, J. R. Ecker, J. A. Thomson, B. Ren, Chromatin architecture reorganization during stem cell differentiation. *Nature* **518**, 331–336 (2015).
- A. Burton, M.-E. Torres-Padilla, Chromatin dynamics in the regulation of cell fate allocation during early embryogenesis. *Nat. Rev. Mol. Cell Biol.* **15**, 723–735 (2014).
- J. D. Buenrostro, B. Wu, U. M. Litzenburger, D. Ruff, M. L. Gonzales, M. P. Snyder, H. Y. Chang, W. J. Greenleaf, Single-cell chromatin accessibility reveals principles of regulatory variation. *Nature* **523**, 486–490 (2015).
- S. Park, R. Merino-Urtaza, V. Karwacki-Neisius, G. E. Carrizo, A. Athreya, A. Marin-Gonzalez, N. A. Benning, J. Park, M. M. Mitchener, N. V. Bhanu, B. A. Garcia, B. Zhang, T. W. Muir, E. L. Pearce, T. Ha, Native nucleosomes intrinsically encode genome organization principles. *Nature* **643**, 572–581 (2025).
- J. Xu, H. Ma, J. Jin, S. Uttam, R. Fu, Y. Huang, Y. Liu, Super-resolution imaging of higher-order chromatin structures at different epigenomic states in single mammalian cells. *Cell Rep.* **24**, 873–882 (2018).
- C. Tse, T. Sera, A. P. Wolffe, J. C. Hansen, Disruption of higher-order folding by core histone acetylation dramatically enhances transcription of nucleosomal arrays by RNA polymerase III. *Mol. Cell. Biol.* **18**, 4629–4638 (1998).
- M. Shogren-Knaak, H. Ishii, J.-M. Sun, M. J. Pazin, J. R. Davie, C. L. Peterson, Histone H4-K16 acetylation controls chromatin structure and protein interactions. *Science* **311**, 844–847 (2006).
- A. Allahverdi, R. Yang, N. Korolev, Y. Fan, C. A. Davey, C.-F. Liu, L. Nordenskiöld, The effects of histone H4 tail acetylations on cation-induced chromatin folding and self-association. *Nucleic Acids Res.* **39**, 1680–1691 (2011).
- J. Funke, P. Ketterer, C. Lieleg, S. Schunter, P. Korber, H. Dietz, Uncovering the forces between nucleosomes using DNA origami. *Sci. Adv.* **2**, e1600974 (2016).
- C. Dhalluin, J. E. Carlson, L. Zeng, C. He, A. K. Aggarwal, M.-M. Zhou, M.-M. Zhou, Structure and ligand of a histone acetyltransferase bromodomain. *Nature* **399**, 491–496 (1999).
- J. Lovén, H. A. Hoke, C. Y. Lin, A. Lau, D. A. Orlando, C. R. Vakoc, J. E. Bradner, T. I. Lee, R. A. Young, Selective inhibition of tumor oncogenes by disruption of super-enhancers. *Cell* **153**, 320–334 (2013).
- A. J. Bannister, P. Zegerman, J. F. Partridge, E. A. Miska, J. O. Thomas, R. C. Allshire, T. Kouzarides, Selective recognition of methylated lysine 9 on histone H3 by the HP1 chromo domain. *Nature* **410**, 120–124 (2001).
- M. Lachner, D. O'Carroll, S. Rea, K. Mechta, T. Jenuwein, Methylation of histone H3 lysine 9 creates a binding site for HP1 proteins. *Nature* **410**, 116–120 (2001).
- S. Machida, Y. Takizawa, M. Ishimaru, Y. Sugita, S. Sekine, J.-i. Nakayama, M. Wolf, H. Kurumizaka, Structural basis of heterochromatin formation by human HP1. *Mol. Cell* **69**, 385–397.e8 (2018).
- S. Poepel, V. Kasinath, E. Nogales, Cryo-EM structures of PRC2 simultaneously engaged with two functionally distinct nucleosomes. *Nat. Struct. Mol. Biol.* **25**, 154–162 (2018).
- N. J. Francis, R. E. Kingston, C. L. Woodcock, Chromatin compaction by a polycomb group protein complex. *Science* **306**, 1574–1577 (2004).
- S. Kilic, S. Felekyan, O. Doroshenko, I. Boichenko, M. Dimura, H. Vardanyan, L. C. Bryan, G. Arya, C. A. M. Seidel, B. Fierz, Single-molecule FRET reveals multiscale chromatin dynamics modulated by HP1α. *Nat. Commun.* **9**, 235 (2018).
- F. Song, P. Chen, D. Sun, M. Wang, L. Dong, D. Liang, R.-M. Xu, P. Zhu, G. Li, Cryo-EM study of the chromatin fiber reveals a double helix twisted by tetranucleosomal units. *Science* **344**, 376–380 (2014).
- B. A. Gibson, L. K. Doolittle, M. W. G. Schneider, L. E. Jensen, N. Gamarra, L. Henry, D. W. Gerlich, S. Redding, M. K. Rosen, Organization of chromatin by intrinsic and regulated phase separation. *Cell* **179**, 470–484.e21 (2019).
- H. Strickfaden, T. O. Tolsma, A. Sharma, D. A. Underhill, J. C. Hansen, M. J. Hendzel, Condensed Chromatin behaves like a solid on the mesoscale in vitro and in living cells. *Cell* **183**, 1772–1784.e13 (2020).
- S. Portillo-Ledesma, Z. Li, T. Schlick, Genome modeling: From chromatin fibers to genes. *Curr. Opin. Struct. Biol.* **78**, 102506 (2023).
- L. N. Mishra, J. J. Hayes, A nucleosome-free region locally abrogates histone H1-dependent restriction of linker DNA accessibility in chromatin. *J. Biol. Chem.* **293**, 19191–19200 (2018).
- M. M. Müller, B. Fierz, L. Bittova, G. Liszczak, T. W. Muir, A two-state activation mechanism controls the histone methyltransferase Suv39h1. *Nat. Chem. Biol.* **12**, 188–193 (2016).
- M. J. Blacketer, S. J. Feely, M. A. Shogren-Knaak, Nucleosome interactions and stability in an ordered nucleosome array model system. *J. Biol. Chem.* **285**, 34597–34607 (2010).
- P. T. Lowary, J. Widom, New DNA sequence rules for high affinity binding to histone octamer and sequence-directed nucleosome positioning. *J. Mol. Biol.* **276**, 19–42 (1998).
- B. M. Turner, Histone acetylation and control of gene expression. *J. Cell Sci.* **99**, 13–20 (1991).

27. M. Grunstein, Histone acetylation in chromatin structure and transcription. *Nature* **389**, 349–352 (1997).
28. M. Wakamori, Y. Fujii, N. Suka, M. Shirouzu, K. Sakamoto, T. Umehara, S. Yokoyama, Intra-and inter-nucleosomal interactions of the histone H4 tail revealed with a human nucleosome core particle with genetically-incorporated H4 tetra-acetylation. *Sci. Rep.* **5**, 17204 (2015).
29. M. Wakamori, K. Okabe, K. Ura, T. Funatsu, M. Takinoue, T. Umehara, Quantification of the effect of site-specific histone acetylation on chromatin transcription rate. *Nucleic Acids Res.* **48**, 12648–12659 (2020).
30. Z. Shipony, G. K. Marinov, M. P. Swaffer, N. A. Sinnott-Armstrong, J. M. Skotheim, A. Kundaje, W. J. Greenleaf, Long-range single-molecule mapping of chromatin accessibility in eukaryotes. *Nat. Methods* **17**, 319–327 (2020).
31. A. B. Stergachis, B. M. Debo, E. Haugen, L. S. Churchman, J. A. Stamatoyannopoulos, Single-molecule regulatory architectures captured by chromatin fiber sequencing. *Science* **368**, 1449–1454 (2020).
32. Q. Chen, R. Yang, N. Korolev, C. F. Liu, L. Nordenskiöld, Regulation of nucleosome stacking and chromatin compaction by the histone H4 N-terminal tail–H2A acidic patch interaction. *J. Mol. Biol.* **429**, 2075–2092 (2017).
33. B. H. Zimm, Dynamics of polymer molecules in dilute solution: Viscoelasticity, flow birefringence and dielectric loss. *J. Chem. Phys.* **24**, 269–278 (1956).
34. M. Doi, S. F. Edwards, *The Theory of Polymer Dynamics* (Oxford Univ. Press, 1988), vol. 73.
35. A. J. Goldman, R. G. Cox, H. Brenner, Slow viscous motion of a sphere parallel to a plane wall—I Motion through a quiescent fluid. *Chem. Eng. Sci.* **22**, 637–651 (1967).
36. J. Yao, P. T. Lowary, J. Widom, Direct detection of linker DNA bending in defined-length oligomers of chromatin. *Proc. Natl. Acad. Sci. U.S.A.* **87**, 7603–7607 (1990).
37. E. Lieberman-Aiden, N. L. van Berkum, L. Williams, M. Imakaev, T. Ragoczy, A. Telling, I. Amit, B. R. Lajoie, P. J. Sabo, M. O. Dorschner, R. Sandstrom, B. Bernstein, M. A. Bender, M. Groudine, A. Gnirke, J. Stamatoyannopoulos, L. A. Mirny, E. S. Lander, J. Dekker, Comprehensive mapping of long-range interactions reveals folding principles of the human genome. *Science* **326**, 289–293 (2009).
38. E. Oberbeckmann, K. Quillilan, P. Cramer, A. M. Oudelaar, In vitro reconstitution of chromatin domains shows a role for nucleosome positioning in 3D genome organization. *Nat. Genet.* **56**, 483–492 (2024).
39. M. Ohno, T. Ando, D. G. Priest, V. Kumar, Y. Yoshida, Y. Taniguchi, Sub-nucleosomal genome structure reveals distinct nucleosome folding motifs. *Cell* **176**, 520–534.e25 (2019).
40. K. Maeshima, R. Rogge, S. Tamura, Y. Joti, T. Hikima, H. Szerlong, C. Krause, J. Herman, E. Seidel, J. DeLuca, T. Ishikawa, J. C. Hansen, Nucleosomal arrays self-assemble into supramolecular globular structures lacking 30-nm fibers. *EMBO J.* **35**, 1115–1132 (2016).
41. D. E. Olins, A. L. Olins, Chromatin history: Our view from the bridge. *Nat. Rev. Mol. Cell Biol.* **4**, 809–814 (2003).
42. A. Routh, S. Sandin, D. Rhodes, Nucleosome repeat length and linker histone stoichiometry determine chromatin fiber structure. *Proc. Natl. Acad. Sci. U.S.A.* **105**, 8872–8877 (2008).
43. N. Jentink, C. Purnell, B. Kable, M. T. Swulius, S. A. Grigoryev, Cryoelectron tomography reveals the multiplex anatomy of condensed native chromatin and its unfolding by histone citrullination. *Mol. Cell* **83**, 3236–3252.e7 (2023).
44. S. Cai, Y. Song, C. Chen, J. Shi, L. Gan, Natural chromatin is heterogeneous and self-associates in vitro. *Mol. Biol. Cell* **29**, 1652–1663 (2018).
45. E. Crane, Q. Bian, R. P. McCord, B. R. Lajoie, B. S. Wheeler, E. J. Ralston, S. Uzawa, J. Dekker, B. J. Meyer, Condensin-driven remodelling of X chromosome topology during dosage compensation. *Nature* **523**, 240–244 (2015).
46. Y. Cui, C. Bustamante, Pulling a single chromatin fiber reveals the forces that maintain its higher-order structure. *Proc. Natl. Acad. Sci. U.S.A.* **97**, 127–132 (2000).
47. J. D. Halverson, J. Smrek, K. Kremer, A. Y. Grosberg, From a melt of rings to chromosome territories: The role of topological constraints in genome folding. *Rep. Prog. Phys.* **77**, 022601 (2014).
48. A. L. Sanborn, S. S. P. Rao, S.-C. Huang, N. C. Durand, M. H. Huntley, A. I. Jewett, I. D. Bochkov, D. Chinnappan, A. Cutkosky, J. Li, K. P. Geeting, A. Gnirke, A. Melnikov, D. McKenna, E. K. Stamenova, E. S. Lander, E. L. Aiden, Chromatin extrusion explains key features of loop and domain formation in wild-type and engineered genomes. *Proc. Natl. Acad. Sci. U.S.A.* **112**, E6456–E6465 (2015).
49. T.-H. S. Hsieh, C. Cattoglio, E. Slobodyanyuk, A. S. Hansen, O. J. Rando, R. Tjian, X. Darzacq, Resolving the 3D landscape of transcription-linked mammalian chromatin folding. *Mol. Cell* **78**, 539–553.e8 (2020).
50. K. Adachi, K. Kawaguchi, Chromatin state switching in a polymer model with mark-conformation coupling. *Phys. Rev. E* **100**, 060401 (2019).
51. M. Barbieri, M. Chotalia, J. Fraser, L.-M. Lavitas, J. Dostie, A. Pombo, M. Nicodemi, Complexity of chromatin folding is captured by the strings and binders switch model. *Proc. Natl. Acad. Sci. U.S.A.* **109**, 16173–16178 (2012).
52. R. Colleparo-Guevara, G. Portella, M. Vendruscolo, D. Frenkel, T. Schlick, M. Orozco, Chromatin unfolding by epigenetic modifications explained by dramatic impairment of internucleosome interactions: A multiscale computational study. *J. Am. Chem. Soc.* **137**, 10205–10215 (2015).
53. D. Michieletto, E. Orlandini, D. Marenduzzo, Polymer model with epigenetic recoloring reveals a pathway for the de novo establishment and 3D organization of chromatin domains. *Phys. Rev. X* **6**, 041047 (2016).
54. T. Brouwer, C. Pham, A. Kaczmarczyk, W.-J. De Voogd, M. Botto, P. Vizjak, F. Mueller-Planitz, J. van Noort, A critical role for linker DNA in higher-order folding of chromatin fibers. *Nucleic Acids Res.* **49**, 2537–2551 (2021).
55. M. Kikuchi, S. Morita, M. Wakamori, S. Sato, T. Uchikubo-Kamo, T. Suzuki, N. Dohmae, M. Shirouzu, T. Umehara, Epigenetic mechanisms to propagate histone acetylation by P300/CBP. *Nat. Commun.* **14**, 4103 (2023).
56. M. Mivelaz, B. Fierz, Observing protein interaction dynamics to chemically defined chromatin fibers by colocalization single-molecule fluorescence microscopy. *Methods* **184**, 112–124 (2020).
57. M. Tokunaga, N. Imamoto, K. Sakata-Sogawa, Highly inclined thin illumination enables clear single-molecule imaging in cells. *Nat. Methods* **5**, 159–161 (2008).
58. A. Edelstein, N. Amodaj, K. Hoover, R. Vale, N. Stuurman, Computer control of microscopes using μManager. *Curr. Protoc. Mol. Biol.* **92**, 14.20.1–14.20.17 (2010).
59. H. Pinkard, N. Stuurman, I. E. Ivanov, N. M. Anthony, W. Ouyang, B. Li, B. Yang, M. A. Tsuchida, B. Chhun, G. Zhang, R. Mei, M. Anderson, D. P. Shepherd, I. Hunt-Isaak, R. L. Dunn, W. Jahr, S. Kato, L. A. Royer, J. R. Thiagarajah, K. W. Elceir, E. Lundberg, S. B. Mehta, L. Waller, Pycro-Manager: Open-source software for customized and reproducible microscope control. *Nat. Methods* **18**, 226–228 (2021).
60. S. W. Provencher, CONTIN: A general purpose constrained regularization program for inverting noisy linear algebraic and integral equations. *Comput. Phys. Commun.* **27**, 229–242 (1982).
61. A. Scotti, W. Liu, J. S. Hyatt, E. S. Herman, H. S. Choi, J. W. Kim, L. A. Lyon, U. Gasser, A. Fernandez-Nieves, The CONTIN algorithm and its application to determine the size distribution of microgel suspensions. *J. Chem. Phys.* **142**, 234905 (2015).
62. Stephen Provencher, CONTIN. <http://lcmode.lca/contin.shtml>.
63. Oxford Nanopore Technologies PLC, Nanoporetech/Dorado. <https://github.com/nanoporetech/dorado>.
64. Oxford Nanopore Technologies PLC, Nanoporetech/modkit. <https://github.com/nanoporetech/modkit>.
65. S. van der Walt, J. L. Schönberger, J. Nunez-Iglesias, F. Boulogne, J. D. Warner, N. Yager, E. Gouillart, T. Yu, scikit-image contributors, Scikit-image: Image processing in Python. *PeerJ* **2**, e453 (2014).
66. P. A. Knight, D. Ruiz, A fast algorithm for matrix balancing. *IMA J. Numer. Anal.* **33**, 1029–1047 (2013).
67. S. B. Reiff, A. J. Schroeder, K. Kirli, A. Cosolo, C. Bakker, L. Mercado, S. Lee, A. D. Veit, A. K. Balashov, C. Vitzthum, W. Ronchetti, K. M. Pitman, J. Johnson, S. R. Ehmsen, P. Kerpedjiev, N. Abdennur, M. Imakaev, S. U. Öztürk, Ü. Çamoğlu, L. A. Mirny, N. Gehlenborg, B. H. Alver, P. J. Park, The 4D nucleome data portal as a resource for searching and visualizing curated nucleomics data. *Nat. Commun.* **13**, 2365 (2022).
68. J. Dekker, A. S. Belmont, M. Guttman, V. O. Leshy, J. T. Lis, S. Lomvardas, L. A. Mirny, C. C. O’Shea, P. J. Park, B. Ren, J. C. R. Politz, J. Shendure, S. Zhong, The 4D nucleome project. *Nature* **549**, 219–226 (2017).
69. B. Dorigo, T. Schalch, K. Bystricky, T. J. Richmond, Chromatin fiber folding: Requirement for the histone H4 N-terminal tail. *J. Mol. Biol.* **327**, 85–96 (2003).
70. Z. Zhang, S. R. Park, A. Pertisnidis, A. Revyakin, Cloud-Point PEG Glass Surfaces for Imaging of Immobilized Single Molecules by Total-internal-reflection Microscopy. *Bio Protoc.* **6**, e1784 (2016).
71. N. Rohland, D. Reich, Cost-effective, high-throughput DNA sequencing libraries for multiplexed target capture. *Genome Res.* **22**, 939–946 (2012).
72. D. Nečas, P. Klápetek, Gwyddion: An open-source software for SPM data analysis. *Centr. Eur. J. Phys.* **10**, 181–188 (2012).
73. S. Kubo, K. Umeda, N. Kodera, S. Takada, Removing the parachuting artifact using two-way scanning data in high-speed atomic force microscopy. *Biophys. Physicobiol.* **20**, e200006 (2023).
74. D. Erb, pybaselines: A Python library of algorithms for the baseline correction of experimental data. 10.5281/zenodo.5608581, <https://github.com/derb12/pybaselines>.
75. P. J. A. Cock, T. Antao, J. T. Chang, B. A. Chapman, C. J. Cox, A. Dalke, I. Friedberg, T. Hamelryck, F. Kauff, B. Wilczynski, M. J. L. de Hoon, Biopython: Freely available Python tools for computational molecular biology and bioinformatics. *Bioinformatics* **25**, 1422–1423 (2009).
76. M. Roelfs, P. C. Kroon, tBuLi/Symfit: Symfit 0.5.6, Zenodo (2023); 10.5281/zenodo.7643591, <https://doi.org/10.5281/zenodo.7643591>.
77. Y. T. Fukai, K. Kawaguchi, LapTrack: Linear assignment particle tracking with tunable metrics. *Bioinformatics* **39**, btac799 (2023).
78. M. Koch, J.-U. Sommer, A. Blumen, Polymer chains tethered to impenetrable interfaces: Broadening of relaxation spectra. *J. Chem. Phys.* **106**, 1248–1256 (1997).

Acknowledgments: We thank Y. Sakaide for technical assistance, O. Nishimura and T. Kondo (Laboratory for Developmental Genome System, RIKEN Center for Biosystems Dynamics Research) for assistance in sequencing, T. Yamamoto for the discussion on the polymer relaxation timescale, and K. Adachi, S. Kohyama, R.T. Cerbus, and I. Hiratani for reading and commenting on the manuscript. We also thank all the past and current members of the Kawaguchi laboratory for helpful discussions. **Funding:** This work was supported by JSPS KAKENHI grant numbers JP22K14016 (to Y.T.F.), JP22K15033, JP23K17392 (to T.K.), JP23H05475, JP24H02328 (to H.K.), JP20H03388, JP21H05764, JP24K02184 (to T.U.), JP19H05795, JP19H05275, JP21H01007, JP23H00095, and JP25H01361 (to K.K.). This work was also supported by JST ERATO grant number JPMJER1901, JST CREST grant number JPMJCR24T3, Research Support Project for Life Science and Drug Discovery (BLNDS) JP25ama121009 (to H.K.), and JST ACT-X grant number JPMJAX24LF (to Y.T.F.). **Author contributions:** Conceptualization: Y.T.F. and K.K. Methodology: Y.T.F., T.K., S.K., L.Y., S.Z., C.T.,

M.K., H.K., and K.K. Software: Y.T.F. Validation: Y.T.F. Formal analysis: Y.T.F. and K.K. Investigation: Y.T.F., S.K., L.Y., S.Z., C.T., M.K., and K.K. Resources: M.W., T.U., S.M., and M.S. Data curation: Y.T.F. and K.K. Writing—original draft: Y.T.F. and K.K. Writing—review and editing: Y.T.F., T.K., S.Z., S.M., M.S., H.K., T.U., and K.K. Visualization: Y.T.F. and K.K. Supervision: K.K. Project administration: Y.T.F. and K.K. Funding acquisition: H.K., T.U., K.K., Y.T.F., and T.K. **Competing interests:** The authors declare that they have no competing interests. **Data and materials availability:** The basic data and code needed to reproduce our results can be found at doi: 10.5281/zenodo.15826485.

Submitted 2 April 2025

Accepted 25 September 2025

Published 19 November 2025

10.1126/sciadv.adx9282

Supplementary Materials for

Gene-scale *in vitro* reconstitution reveals histone acetylation directly controls chromatin architecture

Yohsuke T. Fukai *et al.*

Corresponding author: Yohsuke T. Fukai, ysk@yfukai.net; Kyogo Kawaguchi, kyogo.kawaguchi@riken.jp

Sci. Adv. **11**, eadx9282 (2025)
DOI: 10.1126/sciadv.adx9282

The PDF file includes:

Supplementary Methods
Figs. S1 to S12
Legends for tables S1 to S3
References

Other Supplementary Material for this manuscript includes the following:

Tables S1 to S3

Supplementary Information

Supplementary Information contains Supplementary Methods, all Supplementary Figures and Supplementary Tables.

Supplementary Methods

Plasmid construction for non-barcoded 12-mer nucleosome arrays

To introduce additional restriction enzyme cut sites, the original plasmid containing 12 repeats of the 601 sequence was digested with BbsI-HF (New England Biolabs, R3539), and the plasmid backbone was amplified by polymerase chain reaction (PCR) using the primers containing the sticky end sequences for the ligation reaction. These fragments were then purified by agarose gel electrophoresis and assembled using the NEBuilder HiFi DNA Assembly Master Mix (New England Biolabs, E2621) and transformed into NEB 5-alpha Competent *E. coli* (New England Biolabs, C2987).

Plasmid construction for barcoded 12-mer nucleosome arrays

First, a plasmid with a single 601 sequence and spacer sequence (plasmid 1) was generated by PCR amplification of the plasmid backbone of a non-barcoded plasmid, digesting the product by AflIII (New England Biolabs, R0541S) and BanI (New England Biolabs, R0118S), which was ligated to a single 601 fragment digested by AflIII and BanI. The plasmid was then amplified using the 5-alpha cells and purified using the NucleoSpin™ Plasmid Transfection-grade kit (Macherey-Nagel, 740490), digested with AvaI (New England Biolabs, R0152S) and purified by agarose gel electrophoresis.

Fragments containing a 601 sequence and a barcoded linker sequence were generated by annealing two oligonucleotides (120 bp each, 20 bp annealing region) with a temperature gradient from 95 to 4 °C at 1 °C/min in buffer containing 10 mM Tris-HCl (pH 7.5) and 50 mM NaCl or 10 mM Bis-Tris-Propane (pH 7.4) and 100 mM NaCl, and then filling in the single stranded parts by 0.1 U Klenow fragments (Takara Bio, 2140A) at the concentration 0.1 µg/µL with 0.1 mM dNTP mix (New England Biolabs, N0447S) in 1X Klenow fragment buffer (10 mM Tris-HCl (pH 7.5), 7 mM MgCl₂, 0.1 mM DTT). The sample was incubated first at 10 °C for 4 hours and then at 4 °C overnight, and then precipitated by ethanol with an overnight incubation at -20 °C. 40 µg of the filled oligonucleotide was cut with 200 U AvaI in 200 µL and purified by electrophoresis in 3 % agarose gel.

The digested fragment was then ligated into the AvaI-digested plasmid 1 treated with Quick CIP, transformed into the 5-alpha cells, and the cells were grown on an LB plate. The colonies were then collected and midi-cultured, and the plasmid was purified using the NucleoBond Xtra Midi kit (Macherey-Nagel, U0410B) (plasmid 2).

Fragments containing a single 601 sequence and a barcoded linker sequence with the BsmBI recognition sequence cutting the AvaI site were similarly prepared and ligated into the BbsI-digested plasmid 2 treated with Quick CIP (BbsI-HF: New England Biolabs, R3539L). The plasmid was transformed into the 5-alpha cells, which were grown on an LB plate. Colonies were collected, and the plasmids were purified using the NucleoSpin Plasmid Transfection-grade kit (plasmid 3)

Fragments containing a 601 sequence and a barcoded linker sequence were purified from the plasmid 2 by digestion with *Ava*I and electrophoresis in 3 % agarose gel. 180 ng of the fragment was then ligated to the plasmid 3 digested by *Bbs*I and treated with Quick CIP at 10:1 ratio with 2000 U T4 DNA ligase (New England Biolabs, M0202M), at 16 °C for overnight in 13 µL. The ligated product was transformed into the 5-alpha cells, which were grown on an LB plate. The colonies were then collected and mid-cultured, and the plasmid was purified using the NucleoBond Xtra Midi/Maxi kit (plasmid 4). The plasmid 4 was then transformed into the 5-alpha cells, which were grown on an LB plate. The colonies were isolated and checked by direct PCR, which revealed that the plasmid typically contains 4–9 repeats of the 601 sequence along with the spacer sequences.

Colonies hosting plasmids containing 5-mer to 7-mer repeats without errors were identified by direct colony PCR and Sanger sequencing. Plasmids were isolated from those colonies using the NucleoSpin Plasmid Transfection-grade kit, digested by *Bbs*I, and treated with Quick CIP. Nine independent plasmids were then constructed by ligating the digested plasmids to the 5-mer to 7-mer products isolated from plasmid 4 using *Bbs*I and *Bsm*BI digestion (*Bsm*BI-v2: New England Biolabs, R0739S) followed by agarose gel electrophoresis. The *Bgl*II sites for the sticky ends and the adjacent barcode sequences were modified similarly to the non-barcoded plasmids.

Plasmids with different linker lengths were constructed using a similar strategy. Plasmids containing a single linker sequence and a single Widom 601 sequence excised by *Ava*I digestion was constructed from single-stranded oligonucleotides and a plasmid backbone containing a single Widom 601 sequence using the NEBuilder HiFi DNA Assembly Master Mix. The *Ava*I site at the 3' end of the fragment was designed to be digested also by *Bbs*I, with the *Bbs*I recognition site located outside the fragment. For each linker length, two variants were generated: plasmid 5, which contains a *Bsm*BI site within the fragment that allows digestion of the *Ava*I site at the 5' end, and plasmid 6, which lacks this site.

Plasmid 6 was digested with *Ava*I, and the excised fragment was purified by agarose gel electrophoresis. The purified fragment (13.8 ng/µL) was ligated into *Bbs*I-digested, Quick CIP-treated plasmid 5 using T4 DNA ligase (New England Biolabs, M0202M) in T4 DNA Ligase Reaction Buffer (New England Biolabs, B0202S) at 16 °C for overnight, with the fragment at a 10-fold molar excess relative to the plasmid and the ligase added at 1/13 of the total reaction volume. The ligation product was transformed into *E. coli* 5-alpha cells and plasmid DNA was extracted using the NucleoBond Xtra Midi kit. The plasmids were then digested with *Bbs*I-HF and subjected to electrophoresis in 0.7 % agarose gel in 1× TAE buffer. Bands corresponding to single-cut plasmids containing 5–7 insert fragments were excised, gel-purified, and self-ligated at a concentration of 1 ng/µL using 17.5 U/µL T4 DNA ligase (Takara Bio, 2011A) in 1× Takara ligase buffer at 16 °C for 60 min, followed by enzyme inactivation at 70 °C for 10 min. The ligated products were transformed into 5-alpha cells, and clones for 5–7-mer constructs were identified by gel electrophoresis and confirmed by Sanger sequencing.

To generate 12-mer constructs, the verified insert fragments were excised from the plasmids by *Bbs*I and *Bsm*BI digestion, purified by agarose gel electrophoresis, and ligated into other *Bbs*I-digested, CIP-treated plasmids. The *Bgl*II sites for the sticky ends and the adjacent barcode sequences were modified similarly to the non-barcoded plasmids. Additionally, any remaining non-unique barcodes were replaced with unique ones through restriction enzyme digestion followed by assembly using the NEBuilder HiFi DNA Assembly Master Mix.

Purification of octamer sink DNA fragments

2-300 bp octamer sink DNA fragments were generated by taking the supernatant of the PEG precipitation to concentrate the EcoRV-digested backbone fragments, precipitating the DNA with ethanol, and digesting the remaining 12×601 array with StyI-HF (New England Biolabs, R3500S) and precipitating by phenol-chloroform-isoamyl alcohol and ethanol if it remained in the product. These octamer sink fragments were used in the reconstitution step to prevent non-specific binding of histone octamers to linker regions (17,69).

End labeling of A and H fragments

For labeling, 28 µL of 1 mM modified oligonucleotide (5'-Ph-TAGTCTGC(T*)CAGATATCGTCG-Biotin-3', where T* represents the amine-linked dT with the C6 linker, purchased from Merck) dissolved in 0.091 M sodium tetraborate-HCl buffer (NaB buffer, made from Sodium Tetraborate Decahydrate, Nacalai Tesque, Inc., 31223-85) was mixed with 5.6 µL of 14 mM Atto647N-NHS ester (ATTO-TEC GmbH, AD647N-31) in DMSO and incubated overnight at room temperature. The labeled fragment was ethanol precipitated with ×0.286 volume of 3 M NaOAc and ×2.571 volume of ethanol, with 10 min incubation at -20 °C. Another modified oligonucleotide (5'-CACAGCTG(T*)CTGAG-3') was also labeled with Atto565-NHS ester (ATTO-TEC GmbH, AD 565-31). The dye labeling efficiency measured by the absorbance was 60 % and 69 %, respectively.

These labeled oligonucleotides were then annealed with the complementary strands extended by 3 bp for the sticky ends that ligate with the A and H arrays, respectively (Fig. 1B). Annealing was performed at a concentration of 100 µM for each fragment, in the presence of 10 mM Bis-Tris-Propane (pH 7.4) (Nacalai Tesque, Inc., 08892-32), 1 mM MgCl₂ and 100 mM NaCl, with cooling at a rate of 1 °C/min.

1.2 mg of the BgII-digested and PEG-purified A and H fragments were then mixed with a five-fold molar excess of the annealed products and ligated with 2100 U T4 DNA ligase (Takara Bio, 2011A) in a final reaction volume of 750 µL at 16 °C for overnight. The ligated product was then PEG-purified as described in the previous section.

Reconstitution of 12-mer nucleosome arrays

The template DNA hosting 12 repeats of the 601 sequence was mixed with the reconstituted histone octamer and short octamer sink DNA fragments, where the salt concentration was adjusted to 2 M KCl. The molar ratio of the octamer and buffer DNA fragment to the 601 sequences was chosen to be 1.2 and 5/12 for the non-barcoded arrays and 1.1 and 1/3 for the barcoded arrays.

The mixture was transferred to a microdialysis tube, Xpress Micro Dialyzer MD100 MWCO 6-8 kDa (Scienova GmbH, SCI-40076), and dialyzed in a gradient from RB-High (10 mM Tris-HCl (pH 7.5) (Nacalai Tesque, Inc., 35434-21), 1 mM EDTA (Nacalai Tesque, Inc., 06894-85), 2 M KCl (Nacalai Tesque, Inc., 28514-75), and 1 mM DTT (Nacalai Tesque, Inc., 14128-62)) to RB-Low (10 mM Tris-HCl (pH 7.5), 1 mM EDTA, 250 mM KCl) by adding 1.6 L of RB-Low to 0.4 L of RB-High at a rate of 1.6 mL/min while maintaining the total volume. The dialysis tubes were then transferred to 400 mL of RB-Low for another 4 hours of dialysis. The mixture was transferred to 1.5 mL microcentrifuge tubes and centrifuged at 10,000 × g for 10 min. The supernatant was again transferred to microdialysis tubes

and dialyzed against 400 mL of No-salt buffer (10 mM Tris-HCl (pH 7.5) and 1 mM EDTA) for more than 4 hours. The mixture was then transferred to 1.5 mL microcentrifuge tubes and centrifuged at 10,000 × g for 10 min, and the supernatant was transferred to fresh lo-bind tubes (BMBio ST, BM4015).

After the reconstitution, the arrays were purified by 10 % - 40 % sucrose gradient ultracentrifugation. The centrifuged solution was fractionated into 800 μL aliquots by gentle aspiration from the top of the tube, and each fraction was checked by the agarose gel electrophoresis (0.7 % agarose in 0.2X TBE). One or two peak fractions were then concentrated using 100 kDa MWCO Amicon Ultra centrifugal filter (Merck Millipore, UFC5100) at 14,000 × g, and then washed twice by adding 450 μL of No-salt buffer and centrifuging at 14,000 × g for 5 – 15 min.

Reconstituted chromatin was routinely checked by the band shift assay in agarose gel electrophoresis (0.7 % agarose in 0.2X TBE). Also, the nucleosome reconstitution efficiency was validated by digesting ≈ 100 ng of the sample with 2.5 – 10 U of ScaI (Takara Bio, 1084A) in 10 μL of the ScaI cut buffer (10 mM Tris-HCl (pH 7.5), 0.5 mM MgCl₂ and 50 mM NaCl) at 22 °C for 14 hours and confirming the band shift with electrophoresis in native polyacrylamide gel electrophoresis (PAGE) (5 % in 1X TBE, 120V for 30 min) (fig. S1).

The reconstituted 12-mer arrays were diluted to 50-100 ng/μL and supplemented with glycerol at a final concentration of 5 %, aliquoted to 2.5 μg per tube, snap frozen with liquid nitrogen, and stored at -80 °C.

Details of AFM observation

Sample fixation

For the nucleosome counting (Fig. 1 and figs. S1, S4, except Fig. 1I and fig. S4A,E-M), samples were diluted in the No-salt buffer to 0.25-1 ng/μL and fixed with 0.1 % glutaraldehyde (Nacalai Tesque Inc., 17003-92) on ice for 10 min (12-mers) or 30 min (96-mers). For Fig. 1I and figs. S4A,E-M, the sample was diluted in H30D buffer (30 mM HEPES-KOH (pH 7.5) and 1 mM DTT) to 3 ng/μL and fixed with 0.1 % formaldehyde (FUJIFILM Wako Pure Chemical Corp., 064-00406) and 0.05 % glutaraldehyde on ice for 15 min.

Mounting sample on mica plate for AFM observation

A mica plate (Alliance Biosystems, 01872-MB) was peeled by a piece of adhesive tape. 0.01 % poly-L-ornithine solution (Sigma-Aldrich, P3655) was spotted onto the freshly peeled mica plate and then incubated for 1.5 min at room temperature. The plate was then washed three times with 1 mL of ultrapure water (Milli-Q, Merck Millipore) and dried completely with a stream of nitrogen gas.

For the 12-mer samples and 96-mer samples except Fig. 1H,I and fig. S4A,E-M, sample solutions were spotted onto the coated mica plate and incubated for 5 min at room temperature. The sample was gently washed out with 1 mL of ultrapure water and dried with a stream of nitrogen gas. For Fig. 1H, a 1.5 mm × 3 mm chamber (1 mm thickness) made of PDMS sheet and a glass slide was placed on the coated mica plate and 50 μL of the sample was gently injected in 10 sec. We then removed the chamber, washed the plates with 1 mL of ultrapure water twice, and dried them with a stream of nitrogen gas. For Fig. 1I and fig. S4A,E-M, 10 μL of the sample was loaded onto the mica plate spinning at 850-1000 rpm

for 20 sec. After the spin-coating, the sample was gently washed out with 1 mL of ultrapure water and dried with a stream of nitrogen gas.

Samples were observed with the Innova atomic force microscope (Bruker) using the SNL10-C probe in the tapping mode. The set point was typically at 1.5-2 V with the drive amplitude at 5 V.

Details of single-molecule fluorescence microscopy

Chamber construction for single-molecule observation

For the chamber construction for single-molecule imaging, we followed a protocol in Ref. (17) with modifications. Inlet and outlet holes were made on glass slides (Matsunami Glass, S2441) with a micro-grinder. Coverslips (Matsunami Glass, No.1SHT) and glass slides were placed on a TeflonTM rack in a glass beaker. They were washed by sonication in 20× diluted Ultrasonic Cleaner Alkaline Cleaning Agent (SDNU-A4, AS ONE Corporation) for 60 min by ASU-2 (AS ONE Corporation) and kept overnight. The glasses were rinsed five times with ultrapure water and sonicated for 20 min in ultrapure water. They were then rinsed with acetone, sonicated for 20 min in acetone, rinsed with isopropanol, sonicated for 20 min in isopropanol, rinsed with ultrapure water five times, sonicated for 20 min in ultrapure water, and rinsed with ultrapure water five times. The coverslips were Piranha-cleaned with 25 % v/v Hydrogen Peroxide (30 %) (Nacalai Tesque, Inc., 18411-25) and 75 % v/v Sulfuric Acid (Nacalai Tesque, Inc., 32519-95) at 80 °C for 60 min and rinsed four times with ultrapure water. Then, they were mildly etched with 0.5 M KOH with sonication for 60 min to increase the density of the silanol group. The sonication chamber (14 cm×15 cm×10 cm) was first filled with ice to avoid heating (70). The glasses were rinsed twice with ultrapure water and then twice with acetone. The surface was amino-activated by soaking in either 100 mL of 3 % 3-aminopropyltriethoxysilane (Nacalai Tesque, Inc., 02309-04) in the mixture of 95 mL of ethanol, 5 mL of ultrapure water, and 2 mL of acetic acid (Replicate 1) or 80 mL of 3 % 3-aminopropyltriethoxysilane in acetone (Replicate 2) for 60 min at room temperature. The glasses were then rinsed twice with acetone, then twice with ultrapure water, and dried with a stream of nitrogen gas.

40 mg of PEG-SVA (MPEG-SVA, Laysan Bio, Inc.) and 1 mg of biotin-PEG-SVA (BIO-PEG-SVA, Laysan Bio, Inc.) were dissolved into 120 µL of NaB buffer with 0.1 M K₂SO₄. The solution was vortexed well and centrifuged at 10,000 × g for 15 sec. Immediately, 40 µL of the solution was dropped onto the amino-modified coverslip, and another coverslip was placed to sandwich the solution. The coverslips were kept overnight at room temperature in a dark, humid chamber and then rinsed with ultrapure water and dried with a stream of nitrogen gas. They were further passivated with short PEG-NHS ester (2,5-dioxopyrrolidin-1-yl 2,5,8,11-tetraoxatetradecan-14-oate, BLD, BD306356). 12 µL of short PEG was mixed with 240 µL of NaB buffer containing 0.5M KCl, and the coverslips were reacted with the solution in the same way for 2 hours at room temperature. After the reaction, they were quickly rinsed with ultrapure water and dried with a stream of nitrogen gas. For replicate 1, the surface was further passivated by incubation with 1 mg of N-Succinimidyl Acetate (Tokyo Chemical Industry, S0878) dissolved into 240 µL of NaB buffer containing 0.5 M KCl, for 2 hours at room temperature. After the reaction, they were quickly rinsed with ultrapure water and dried with a stream of nitrogen gas.

Pieces of double-coated Kapton[®] film tape (silicone-based adhesive, Teraoka 760H), ≈ 45 µm thick, were cut to make five 12 mm×2 mm channels. SYLGARDTM 184 silicone elastomer kit (DOW) was used

to fabricate a polydimethylsiloxane (PDMS) block. 20 g of base and 2 g of hardener were mixed well, degassed in a vacuum chamber, poured into a 10 cm diameter petri dish, and cured overnight at 80 °C. PDMS blocks were cut out and holes punched to match the holes in the glass slide. The glass slide and PDMS mold were then plasma etched (“Hi” configuration in PDC-32G, Harrick Plasma, corresponding to 18 W applied power to the RF coil) for 1 min and immediately pressed together for adhesion.

The chamber was constructed by sandwiching the adhesive tape between the glass slide and passivated coverslip (Fig. 2B). The channel height was measured with a confocal microscope and found to be $57 \pm 6 \mu\text{m}$. The chambers were kept in a vacuum at -20°C .

At observation, the chambers were taken out of the freezer, and liquid reservoirs (1 mL pipette tips) were inserted into the holes of the PDMS mold and glued with epoxy. We waited for more than 15 min to avoid contaminating the observation chambers with the glue. The coverslips were further passivated again by injecting 20 μL of the mixture of short PEG-NHS ester (5 μL) and NaB buffer (100 μL) (replicate 1) or 0.1 M NaB buffer (pH 8.5) containing 0.5 M KCl (replicate 2) and incubating for more than 15 min.

Imaging buffer preparation

37.5 mg of (\pm)-6-Hydroxy-2,5,7,8-tetramethylchromane-2-carboxylic acid (Trolox, Sigma-Aldrich, 238813) was mixed with 37.5 mL of ultrapure water supplemented with 50 μL of 2.8 M NaOH. The solution was rotated in the dark until the precipitate dissolved, and the concentration of Trolox was measured by the absorbance at 290 nm ($2350 \text{ M}^{-1}\text{cm}^{-1}$). The Trolox solution was then supplemented with HEPES-KOH (pH 7.5, Dojindo 348-01372), D(+)-glucose (FUJIFILM Wako Pure Chemical Corp., 045-31162), and KCl to make the IBs containing 50 mM HEPES-KOH (pH 7.5), 2 mM Trolox, 3.2 % w/v glucose and 50 mM, 100 mM or 150 mM of KCl. Glucose oxidase + bovin liver catalase solution (GODCAT) was prepared by first dissolving 1 mg of catalase (C40-100MG, Sigma Aldrich) in 100 μL of 50 mM PBS (pH 7), and mixing the 20 μL of this solution with 30 μL of T50 (10 mM Tris-HCl (pH 7.5) and 50 mM NaCl) and 5 mg of glucose oxidase (Sigma Aldrich, G2133-10KU). The IBs were supplemented with 1/200 volume of GODCAT just before observation.

Microscope setup

The sample was observed with a fluorescence microscope built with IX83 (Olympus) equipped with the objective lens UPlanApo 60x / 1.50 Oil HR TIRF (Olympus) and with the filters and dichroic mirrors of ZET405/488/561/640xv2, ZT405/488/561/640pcv2 and ZET405/488/561/640mv2 (Chroma Technology). The laser light from OBIS 561nm LS (Coherent) and OBIS 637nm LX (Coherent) were combined by a dichroic mirror (ZT561rdc-UF3, Chroma Technology) and introduced from the rear port of the microscope and focused at the rear focal plane of the objective. The Multisplit V2 (Teledyne Photonics) split the fluorescence light into regions. Fluorescent light that

- Passed through T565lpqr and T635lpqr, and filtered by ET655lp (Chroma Technology)
- Passed through T565lpqr and reflected by T635lpqr, and filtered by ET600/50m (Chroma Technology)

were observed as the signals for the tethered end (Atto647N) and free end (Atto565), respectively (Fig. 2A,C). The angle of the laser has been adjusted for observation with the Highly Inclined and Lami-

nated Optical Sheet (HILO) microscopy (57) so that the signal from the Atto565 is maximized. The laser intensity was 10-20 mW (561 nm) and 10 mW (640 nm), respectively.

Detailed protocol for *in vitro* Hi-C experiment

Fixation

Samples were dialyzed against 12 mL of H30D buffer (30 mM HEPES-KOH (pH 7.5) and 1 mM DTT) for 1 hour at 4 °C in the microdialysis tubes before fixation. They were fixed at the final concentration of 4 ng/µL (12-mer samples), 2.37 ng/µL (96-mer samples, replicates 1 and 2) or 2 ng/µL (96-mer samples, replicates 3 and 4) with 0.5 % formaldehyde and 0.1 % glutaraldehyde in 30 mM HEPES-KOH, 150 mM KCl and 1 mM DTT at 30 °C for 5 min. The reaction was quenched by adding ×1/11 volume of 12× quenching buffer (2.12 M glycine (Nacalai Tesque Inc., 17141-95) and 120mM Tris-HCl (pH7.5, Nacalai Tesque Inc., 35434-21 and 37313-25)). For the 12-mer experiment, the fixation and quenching were performed with the combination of 1 % formaldehyde and ×1/6 volume of the quenching buffer 2 (2.33 M Glycine and 70 mM Tris-HCl (pH 7.5)) and 0.5 % formaldehyde + 0.1 % glutaraldehyde and ×1/12.21 volume of the quenching buffer 2. Samples were dialyzed against 12 mL of No-salt buffer for 1 hour at 4 °C in the microdialysis tubes.

The sample after fixation was checked by the agarose gel electrophoresis and found to show a similar band pattern to that for the samples without fixation (fig. S9A,B). The sample concentration was measured using the Qubit™ dsDNA Quantification Assay Kit HS (Invitrogen, Q32854), and the measured value was used to dilute the sample in the following steps. The measured value was ≈ 2.1 times lower than the actual DNA concentration due to the lower dye binding efficiency. In the following steps, the concentration was calculated by multiplying the measured value by 2.1.

ScaI digestion and wash

The samples were digested at the center of the linker with 0.5 U/µL ScaI (Takara Bio, 1084A) in the ScaI cut buffer (10 mM Tris-HCl (pH 7.5), 0.5 mM MgCl₂, 50 mM NaCl, and 1 mM DTT supplemented with 0.1 mg/mL of recombinant albumin (New England Biolabs, B9200S)) at 22 °C for 14 hours at a final concentration of 5. 6-6.1 ng/µL (12-mer samples), 3.6 ng/µL (96-mer samples, replicates 1 and 2), or 3.0 ng/µL (96-mer samples, replicates 3 and 4). Unfixed samples were also digested at a similar concentration.

The sample was mixed with ×1/9 volume of 10× Mg²⁺ quench buffer (500 mM Tris-HCl (pH 7.5) and 190 mM EDTA) and incubated at 22 °C for 20 min. 5.25-12.1 ng of the sample was taken and digested by SDS/PK (0.5 mg/mL Proteinase K 10 mM Tris-HCl (pH 8.0), 40 mM EDTA and 0.5 % SDS) at 65 °C for 2 h and checked by PAGE and Agilent 2100 Bioanalyzer High Sensitivity DNA Kit (Agilent, 5067-4626) (fig. S9C-G). The results confirm that the DNA was digested into mononucleosomes without systematic bias in the digestion efficiency dependent on the histone modification (fig. S9F,G).

The samples were washed using 100 kDa MWCO Amicon Ultra centrifugal filters using the following protocol:

1. Load 500 µL of the Chromatin Wash Buffer (20 mM HEPES-NaOH (pH7.5), 50 mM NaCl, 0.5 mM EDTA and 0.05 % IGEPAL CA-630 (MP Biomedicals, Inc., 198596)) and centrifuge at 6000 × g

for 3 min at 4 °C.

2. Load the samples and 400 µL of the Chromatin Wash Buffer. Centrifuge at 6000 × g for 3 min at 4 °C.
3. Add 450 µL of the Chromatin Wash Buffer, and centrifuge at 6000 × g for 3 min at 4 °C.
4. Add 450 µL of the Chromatin Wash Buffer, and centrifuge at 6000 × g for 5 min at 4 °C.
5. Add 450 µL of the No-salt buffer and centrifuge at 6000 × g for 5 min at 4 °C.

The washed samples were quantified using the Qubit HS kit. 1.1-10.5 ng of the samples were used for quantification by PAGE (fig. S9C,D). The results indicate the appearance of multi-nucleosome bands, which were not observed in the unfixed samples (fig. S9C,D).

Proximity ligation

Proximity ligation of 4-16.8 ng of the sample was performed in 0.125× T4 DNA ligase buffer (50 mM Tris-HCl (pH 7.5), 10 mM MgCl₂, 1 mM ATP and 10 mM DTT at 1× concentration, New England Biolabs, B0202S) with the presence of 1/250 volume of T4 DNA ligase (Takara Bio, 2011A) at the concentration of 4.2 pg/µL (12-mer samples and 96-mer sample replicate 1) and 1.05 pg/µL (other samples) at 37 °C for 20 min. To avoid aggregation, we first diluted the samples in 10 mM Tris-HCl (pH 7.5), and then ligase buffer and T4 DNA ligase were added and mixed by inversion of the tubes (PROTEOSAVE SS 15mL Conicaltube, FUJIFILM Wako Pure Chemical Corp., 634-28101).

After the proximity ligation, the samples were deproteinized by adding SDS/PK buffer (10 mM Tris-HCl (pH 8.0), 40 mM EDTA and 0.5 % SDS at final concentration) and Proteinase K (0.5 mg/mL at final concentration) in ×1.4 volumes of the proximity ligation and incubating at 65 °C for 2 hours. The samples were concentrated with 2-butanol (Nacalai Tesque Inc., 06102-45) to 3-600 µL, and purified using the FastGene Gel/PCR extraction kit (Nippon Genetics Co., Ltd., FG-91202) with EconoSpin™ IIa columns (Ajinomoto Bio-Pharma Services, EP-11201). ×5 volume of the GP1 solution was used in the first step. The final product was eluted to 40 µL of GP3, which was pre-warmed to 60 °C.

The concentrated samples were quantified using the Qubit HS kit. 0.5 ng of the samples were used for quantification by Agilent 2100 Bioanalyzer High Sensitivity DNA Kit (fig. S9E). The result indicates the appearance of the ligation product compared to the input samples.

Linker digestion, enrichment, and library preparation

The linker sequences were excised from the ligated product by digestion using 32 µL (20 µL for the 12-mer samples) of sample, 5-20 U of NotI-HF (New England Biolabs, R3189S) and 2.5-10 U of AvaiI in 1× rCutSmart buffer (New England Biolabs), 37 °C (lid 75 °C) for 2 hours in 40 µL (25 µL for the 12-mer samples). The digested product was quantified by Agilent 2100 Bioanalyzer High Sensitivity DNA Kit (fig. S9E).

Magnetic bead solution for purification (71) (Serapure) with 2.5 M NaCl was prepared according to the following protocol:

1. Take 1 mL of Sera-Mag SpeedBead Carboxylate-Modified Magnetic Particles (Cytiva, 65152105050250) and wash them with 1 mL of 10 mM Tris-HCl (pH 8.0) (Nacalai

Tesque Inc., 35435-11) by pipetting three times. Place the solution on a magnetic rack and discard the supernatant.

2. Add 1 mL of 100 mM Tris-HCl (pH 8.0) to the washed beads and mix well.
3. Add 25 mL of 5 M NaCl (Nacalai Tesque Inc., 31320-05) and the bead solution into a 50 mL conical tube.
4. Add 20 mL of 50 % (w/v) PEG 8000 (MP Biomedicals, Inc., 195445) in ultrapure water to the tube.
5. Add 4 mL of 100 mM Tris-HCl (pH 8.0) and adjust the final volume to 50 mL by adding ultrapure water.

The sample was purified, and short linker fragments were enriched using Serapure, Ampure XP beads, and precipitation solution (PS, 2.5 M NaCl, 20 % PEG 8000, 10 mM Tris-HCl (pH 8.0)) according to the following protocol:

1. Pre-enrichment wash

- (a) Add 120 μ L of Serapure:PS = 1.8:1.2 mix to 40 μ L of sample, pipette 15 times.
- (b) Incubate for 5 min at room temperature.
- (c) Place the sample on a magnetic rack and wait for 2 min.
- (d) Discard the supernatant.
- (e) Add 100 μ L of 70 % ethanol and discard.
- (f) Repeat the previous step.
- (g) Remove the sample from the magnetic rack, centrifuge, and place it on the magnetic rack.
Remove the ethanol and dry the beads briefly, but do not wait longer than 1 min.
- (h) Add 10 μ L of TE buffer and pipette well. Wait for 2 min.
- (i) Place the sample on a magnetic rack and take the supernatant to another PCR tube.

2. Linker enrichment

- (a) Add 10 μ L of TE buffer to the sample. Mix the sample, Ampure XP Beads, and PS in a ratio of 1:1.2:0.3 (20 μ L, 24 μ L and 6 μ L) by pipetting 15 times.
- (b) Place the samples on the ThermoMixier C (Eppendorf) and keep 25 °C 600 rpm and incubate for 30 min.
- (c) Immediately place the samples on a magnetic rack and incubate for 2 min.
- (d) Transfer the supernatant to another PCR tube.
- (e) Add 150 μ L of Serapure and PS solution (ratio 2:1) to the supernatant. Mix by pipetting 15 times.
- (f) Incubate the samples at room temperature for 5 min.
- (g) Place the samples on a magnetic rack and wait for 2 min.
- (h) Discard the supernatant.

- (i) Add 100 µL of 70 % ethanol to the beads and discard. Repeat this step twice.
- (j) Remove the sample from the magnetic rack, spin it quickly, and place it on the magnetic rack to remove all ethanol. Dry the beads briefly, but do not wait longer than 1 min.
- (k) Add 5µL TE and pipette well. Wait 2 min at room temperature.
- (l) Place the samples on a magnetic rack and transfer the supernatant to another PCR tube.

The samples were analyzed using the Agilent 2100 Bioanalyzer High Sensitivity DNA kit (fig. S9E). The result indicates the enrichment of the linker fragments compared to the input samples.

The sequencing library was prepared from the linker-enriched samples and sequenced as described in the main text.

Preprocessing for AFM images

The forward and backward “TOPO” signals from the AFM were opened with Gwyddion (72) (version 2.62) and processed with the functions “Correct scars”, “Align rows” (in the “Matching” mode), “Level image” and then saved as HDF5 files. Row-wise backgrounds for these signals were estimated by taking the column-wise median values of the pixels, excluding the pixels that deviated more than 30 nm from the median height for the row. The signals were rescaled by subtracting this row-wise background.

The column offset to align the forward and backward signals was found by the peak of the cross-correlation of the two signals, and these signals were merged taking the minimum value of the aligned images similarly to (73). After that, the two-dimensional background signal was estimated as follows. First, the median filter with a footprint of 5×5 was applied, followed by applying a Gaussian filter with a standard deviation of 2. The background was then estimated using a rolling ball algorithm (`skimage.restoration.rolling.ball`) with a radius of 10 after scaling the image by a factor of 2×10^{11} , followed by an additional Gaussian filter with a standard deviation of 5. The result was then rescaled to the original range by dividing by the scaling factor. We performed another round of background subtraction by estimating the background height using the `Baseline2D.pspline_arpls` function from the `pybaselines` package (74) (version 1.1.0). The mask image for the pixels used for fitting was generated by thresholding the image with 0.25 nm and eroding with a 4-pixel radius disk.

Details of nanopore sequencing data analysis

Alignment of linker sequences

For the barcoded arrays, the linker sequences were aligned to the reads using `Bio.Align.PairwiseAligner` of Biopython (version 1.83) (75) with the settings

- `open_gap_score = -2`
- `extend_gap_score = -4`
- `query_left_open_gap_score = -10`
- `query_left_extend_gap_score = -10`

- `query_right_open_gap_score = -10`
- `query_right_extend_gap_score = -10`
- `mode = 'local'`

The alignment results with an alignment score greater than 42 and mapped to a region containing 5-55 bp of the query were analyzed downstream. Since the length of the aligned sequences was different for the 5'-end and 3'-end of the 96-mer, the threshold score was calculated as $0.8 \times l$, where l is the length of the aligned sequence. For the non-barcoded arrays, the junctions (ligated BgII sites) were searched using the `Bio.SeqUtils.nt_search` function.

Alignment for accessibility assay

First, the linker sequences were aligned as described. Sequences were categorized by containing 12-mers and exported into BAM files, retaining the information from the base-called BAM files. The sequences in the BAM files were then aligned to the corresponding reference sequence by the “dorado align” command.

Details of fluorescence microscopy data analysis

Preprocessing and molecule finding

Image data were rescaled by subtracting the background signal (measured from the mean signals without incident light) and dividing by the mean pixel gain (measured by fitting a linear function to the mean and standard deviation values at low illumination). Images for each condition (100 frames each) were averaged for blob detection. Blobs were detected using the Laplacian of Gaussian filter (`skimage.feature.blob_log` in scikit-image version 0.20.0 (65)) with the parameters `min_sigma=2`, `max_sigma=2`, `num_sigma=2`, `threshold=0.75`, `overlap=0.25`, `exclude_border=25`. For each blob, two-dimensional Gaussian functions were fitted to the data with the objective of the least square difference by successively applying the Nelder-Mead method and the trust-constr method using the `symfit` package (76) (Version 0.5.6). Blobs with a Pearson correlation of less than 0.5 from the fitted function values, less than 50 photons for a single frame, and whose center deviates from that detected by the Laplacian of Gaussian filter were excluded from the analysis.

The positional shift between the two channels was corrected using images of multicolor fluorescent beads (TetraSpeck Microspheres, 0.2 μm , ThermoFisher, T7280). The movement of the stage between conditions was corrected using the positions of the far-red blobs (the tethered ends). Specifically, the translation and rotation that minimizes the cost function $-\sum_{i,j} \exp\left[-\|X_i - Y_j\|^2 / \sigma^2\right]$, where X_i and Y_j are the blob positions before and after the transformation, were found by brute-force optimization. Then, the blobs without a matching blob within 2 pixels were discarded, and the final translation and rotation values were estimated by minimizing the mean squared Euclidean distance to the nearest blob. We tracked the blob positions for the free ends in the aligned coordinate to associate them temporally. Since the blob typically shifts with the flow, the images for the flow-applied conditions were shifted to compensate for the effect of the flow (for this association process only). We used LapTrack (77) with

`track_dist_metric="squeuclidean"` and `track_cost_cutoff=225`. The blobs not tracked for more than 50 frames were removed from the analysis. Free ends within 3 pixels of the nearest tethered end were classified as colocalized.

Blob position analysis

For each image, the images were thresholded at the 90 % percentile of intensity, and connected regions with less than two pixels and those touching the boundaries were removed. Movies with more than two connected regions after dilation with the kernel of a 3-pixel radius disk and those with more than five pixels in the thresholded regions touching the boundaries were removed from the analysis. The “centroid masks” were created as disk-shaped regions with a radius of 5 pixels whose center was at the centroid of the original segmented region. The blob position is defined as the centroid of the centroid mask, with the pixel values weighted by the background-subtracted intensity of the image.

Derivation of the fitting function for different exposure times

We obtained the formula $S(T) = \sqrt{\frac{2\beta^2\tau^2}{T} \left[1 - \frac{1-e^{-T/\tau}}{T/\tau} \right]}$ by calculating the variance of the time-averaged position $\bar{x}_T(t) := \frac{1}{T} \int_t^{t+T} x(t') dt'$ as

$$c_T^x := \langle \bar{x}_T(t)^2 \rangle = \frac{1}{T^2} \int_t^{t+T} dt' \int_t^{t+T} dt'' \langle x(t') x(t'') \rangle \quad (\text{S2})$$

$$= \frac{1}{T^2} \int_0^T dt' \int_0^T dt'' \frac{\tau\beta^2}{2} e^{-|t'-t''|/\tau} \quad (\text{S3})$$

$$= \frac{\beta^2\tau^2}{T} \left[1 - \frac{1-e^{-T/\tau}}{T/\tau} \right]. \quad (\text{S4})$$

The standard deviation of the free end position in 2D (Fig. 2F and fig. S5E) is therefore given by $S(T) := \sqrt{\langle \bar{x}_T(t)^2 + \bar{y}_T(t)^2 \rangle} = \sqrt{c_T^x + c_T^y} = \sqrt{2c_T^x}$.

Zimm model with free or tethered ends

Consider a polymer chain consisting of N beads connected by harmonic springs. The time evolution of the position of the i -th bead, $\vec{r}_i(t) = (x_i(t), y_i(t), z_i(t))$, is governed by the Langevin equation

$$\frac{d\vec{r}_i}{dt} = - \sum_{j=0}^{N-1} H_{ij} \frac{\partial U}{\partial \vec{r}_j} + \vec{\xi}_i(t), \quad (\text{S5})$$

where H is the hydrodynamic interaction tensor, U is the potential energy of the system, and $\vec{\xi}_i(t)$ is the random force acting on the i -th bead ($i = 0, 1, \dots, N - 1$). The random force satisfies the fluctuation-dissipation theorem

$$\langle \vec{\xi}_i(t) \cdot \vec{\xi}_j(t') \rangle = 2k_B T H_{ij} \delta(t - t'), \quad (\text{S6})$$

where k_B is the Boltzmann constant, T is the temperature, and $\langle \cdot \rangle$ denotes the ensemble average. Let us consider the Rouse model, where the potential energy is given by

$$U = \frac{k}{2} \sum_{i=0}^{N-2} (\vec{r}_{i+1} - \vec{r}_i)^2, \quad (\text{S7})$$

where k is the spring constant that satisfies

$$k = \frac{3k_B T}{b^2} \quad (\text{S8})$$

with b being the Kuhn length. Under this setup, the average end-to-end distance of the polymer is $R := \sqrt{\langle |\vec{r}_{N-1} - \vec{r}_0|^2 \rangle^{\text{eq}}} = \sqrt{Nb}$, where $\langle \cdot \rangle^{\text{eq}}$ denotes the equilibrium ensemble average.

In the Zimm model, the hydrodynamic interaction tensor is substituted by its equilibrium value:

$$H_{ij}^{\text{eq}} := \langle H_{ij} \rangle^{\text{eq}} = \frac{1}{6\pi\eta a} \delta_{ij} + \frac{1}{\sqrt{6\pi^3|i-j|}\eta b} (1 - \delta_{ij}) \quad (\text{S9})$$

where η is the viscosity of the solvent, and a is the radius of the bead. The Rouse model is obtained by neglecting the off-diagonal terms in the hydrodynamic interaction tensor, which is justified if $a \ll b$.

The Langevin equation is now given by

$$\frac{d\vec{r}_i}{dt} = -k \sum_{j=0}^{N-1} \sum_{k=0}^{N-1} H_{ij}^{\text{eq}} A_{jk} \vec{r}_k + \vec{\xi}_i(t), \quad (\text{S10})$$

where

$$A = \begin{pmatrix} 1 & -1 & 0 & \cdots & 0 \\ -1 & 2 & -1 & \cdots & 0 \\ 0 & -1 & 2 & \cdots & 0 \\ \vdots & \vdots & \vdots & \ddots & \vdots \\ 0 & 0 & 0 & \cdots & 1 \end{pmatrix}, \quad (\text{S11})$$

for the case of free ends, and

$$A = \begin{pmatrix} 2 & -1 & 0 & \cdots & 0 \\ -1 & 2 & -1 & \cdots & 0 \\ 0 & -1 & 2 & \cdots & 0 \\ \vdots & \vdots & \vdots & \ddots & \vdots \\ 0 & 0 & 0 & \cdots & 1 \end{pmatrix}, \quad (\text{S12})$$

for the case of one end tethered to a fixed point. We note that the effect of the impenetrable interface at the tethered end (e.g., passivated glass) is negligible since the experiment measures fluctuations parallel to it. In this case, the relaxation time scale is identical to the chain tethered at one end but otherwise free (78).

By diagonalizing the matrix A as $A = O\Lambda O^T$ using an orthogonal matrix O (satisfying $O^T O = I$) and a diagonal matrix Λ , the equation of motion can be written as

$$\frac{d\vec{X}_n}{dt} = - \sum_{m=0}^{N-1} \sum_{l=0}^{N-1} k \tilde{H}_{nm} \Lambda_{ml} \vec{X}_l + O_{in} \vec{\xi}_i(t), \quad (\text{S13})$$

with $n = 0, 1, \dots, N - 1$, $\vec{X}_n = O_{in} \vec{r}_i$ and $\tilde{H} = O_{in} H^{\text{eq}} O$.

For the free end case, the eigenvalues of A are (for $n = 0, 1, \dots, N - 1$)

$$\Lambda_{nn} = 4 \sin^2\left(\frac{n\pi}{2N}\right), \quad (\text{S14})$$

and the eigenvectors are given by (for $i = 0, 1, \dots, N - 1$ and $n = 0, 1, \dots, N - 1$)

$$O_{in} = \sqrt{\frac{2}{N}} \cos\left(\frac{(2i+1)n\pi}{2N}\right). \quad (\text{S15})$$

We therefore have (for $n, m = 0, 1, \dots, N - 1$)

$$\tilde{H}_{nm} = \frac{2}{N} \sum_{i=0}^{N-1} \sum_{j=0}^{N-1} \cos\left(\frac{(2i+1)n\pi}{2N}\right) \cos\left(\frac{(2j+1)m\pi}{2N}\right) H_{ij}^{\text{eq}}. \quad (\text{S16})$$

For the tethered end case, the eigenvalues of A are

$$\Lambda_{nn} = 4 \sin^2\left(\frac{(2n+1)\pi}{2(2N+1)}\right), \quad (\text{S17})$$

and the eigenvectors are given by

$$O_{in} = \sqrt{\frac{4}{2N+1}} \sin\left(\frac{(i+1)(2n+1)\pi}{2N+1}\right), \quad (\text{S18})$$

We therefore have

$$\tilde{H}_{nm} = \frac{4}{2N+1} \sum_{i=0}^{N-1} \sum_{j=0}^{N-1} \sin\left(\frac{(i+1)(2n+1)\pi}{2N+1}\right) \sin\left(\frac{(j+1)(2m+1)\pi}{2N+1}\right) H_{ij}^{\text{eq}}. \quad (\text{S19})$$

The slowest time scale of relaxation is given by the inverse of the smallest non-zero eigenvalue of $K := k\tilde{H}\Lambda$. However, this is, in general, an ill-defined problem, since the eigenvalues of K can be negative, when the off-diagonal part of the hydrodynamic interaction tensor becomes dominant. This unphysical situation arises due to the approximation Eq. (S9). We nevertheless expect that this approximation is valid for the spatially extended modes (i.e., small n), and take the eigenvalue corresponding to the eigenvector that has the largest component of the $n = 1$ mode (for the free end case) or the $n = 0$ mode (for the tethered end case) as the inverse of the slowest relaxation time, τ . That is, by diagonalizing K as $K = P\lambda P^T$ using an orthogonal matrix P and a diagonal matrix λ , we define τ by

$$p(n) := \underset{m}{\operatorname{argmax}} |P_{nm}| \quad (\text{S20})$$

$$\tau := 1/\lambda_{p(n)p(n)}, \quad (\text{S21})$$

with $n = 1$ for the free end chain and $n = 0$ for the tethered chain.

Under this definition, we numerically obtained τ from the eigenspectrum of K , while varying the Kuhn length b and fixing $N = 96$ (fig. S7A,B). In both the free end and tethered end cases, we obtain the crossover from the Zimm regime to the Rouse regime as b increases:

$$\tau = \alpha \frac{\eta}{k_B T} R^3 \quad \text{for } b \ll a, \quad (\text{S22})$$

$$\tau = \nu \frac{\eta a N}{\pi k_B T} R^2 \quad \text{for } b \gg a. \quad (\text{S23})$$

and $\alpha \approx 1.09$ for the tethered end case¹. We used $\alpha = 1.09$ in comparing with data in Fig. 2G.

For the free end case, since the mean position $\vec{r} := \sum_{i=0}^{N-1} \vec{r}_i / N = \vec{X}_{n=0} / \sqrt{2N}$ follows

$$\frac{d\vec{r}}{dt} = \frac{1}{\sqrt{2N}} O_{i0} \vec{\xi}_i(t), \quad (\text{S24})$$

leading to

$$\langle |\vec{r}(t')|^2 \rangle = \frac{1}{2N} \int_0^t ds \int_0^t du O_{i0} O_{j0} \langle \vec{\xi}_i(s) \cdot \vec{\xi}_j(u) \rangle \quad (\text{S25})$$

$$= \frac{6k_B T}{N^2} t \sum_{i=0}^{N-1} \sum_{j=0}^{N-1} H_{ij}. \quad (\text{S26})$$

Using H_{ij}^{eq} for H_{ij} , the sum is

$$\sum_{i=0}^{N-1} \sum_{j=0}^{N-1} H_{ij} = \frac{N}{6\pi\eta a} + \frac{1}{\sqrt{6\pi^3}\eta b} \sum_{i=0}^{N-1} \sum_{j=0, j \neq i}^{N-1} \frac{1}{\sqrt{|i-j|}} = \frac{N}{6\pi\eta a} + \frac{1}{\sqrt{6\pi^3}\eta b} \left[\frac{8N^{3/2}}{3} + 2\zeta\left(\frac{1}{2}\right)N \right] + o(N). \quad (\text{S27})$$

with the Riemann zeta function $\zeta(\cdot)$. Therefore, we have

$$\langle |\vec{r}(t')|^2 \rangle = 6D_z t, \quad (\text{S28})$$

with²

$$D_z \approx \frac{k_B T}{6\pi\eta a N} + \frac{k_B T}{\sqrt{6\pi^3}\eta b} \left[\frac{8}{3\sqrt{N}} + \frac{2\zeta(1/2)}{N} \right] \quad (\text{S29})$$

The first term corresponds to the diffusion coefficient without accounting for the hydrodynamic interactions. In Fig. 2E, we took $N = 12$ and $a = 6.8$ nm (36). For the theoretical values without hydrodynamic interactions (dashed line), only the first term was used. For those including hydrodynamic interactions (markers), the values of b and N estimated from the 96-mer single-molecule observations, as described in the main text, were applied.

¹In (34), this factor is calculated as 0.325 [Eq. (4.63)]. The difference arises from their approximation, which leads to $\int_0^N dn \int_0^N dm \cos(\pi n/N) \cos(\pi m/N) / \sqrt{|n-m|} \approx N^{3/2} / \sqrt{2}$ due to their continuum-limit calculation (following (33)), being larger than our corresponding term $\sum_{i=0}^N \sum_{j \neq i}^N \cos((2i+1)\pi/2N) \cos((2j+1)\pi/2N) / \sqrt{|i-j|} \approx 0.439N^{3/2}$. There is also the distinction that (34) is approximating $\tau \approx 1/k\tilde{H}_{11}\Lambda_{11}$ in our notation, whereas we use the eigenvalue of K to obtain τ [Eq. (S21)].

²The first term is the same as (34).

Details for in vitro Hi-C data analysis

Analysis pipeline for contact map generation

The reverse complement sequence of the second read was aligned to the first read using `Bio.Align.PairwiseAligner` with the settings

- `open_gap_score = -2`
- `extend_gap_score = -4`
- `query_left_open_gap_score = -2`
- `query_left_extend_gap_score = -2`
- `query_right_open_gap_score = -2`
- `query_right_extend_gap_score = -2`
- `mode = 'local'`

Only sequences with a score greater than 50 and the ScaI recognition sequence (AGTACT) found around the center (between 20 bp and 25 bp) were used in the downstream analysis. Groups of sequences with the same insert sequence and the UMI sequence were counted as a single sequence.

For the replicate 1 and 2 of the 96-mer experiments, we found that the non-barcoded arrays were also present at the positions of the E (NonKac) and F (Kac) arrays, likely due to misidentification of the samples during the ligation step. For these samples, we estimated the abundance of the total arrays by assuming that the contact frequency with the spike-in Kac 12-mer array is symmetric with respect to the center position of the array, and corrected the corresponding rows and columns using the estimated ratio.

20-bp sequences at the 5' and 3' sides of the ScaI recognition sequence were extracted, and a bar-coded sequence with the minimum Hamming distance was selected. Sequences with an average Hamming distance of less than 2 (99.44 % of the total sequences) were used in the downstream analysis.

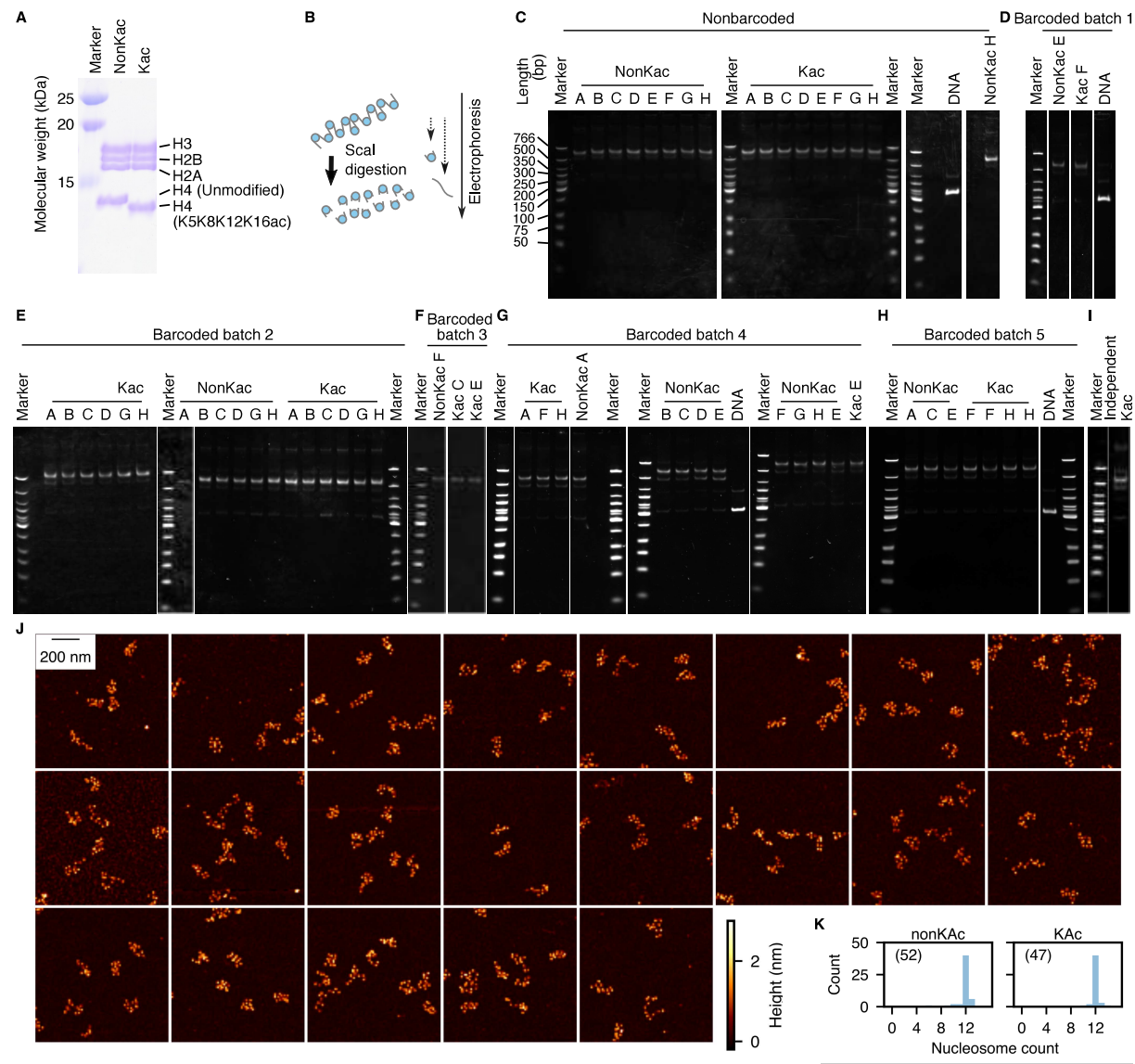
Background level estimation

Let the count matrix $C_{i,j}$ where $i, j = 1, \dots, M$ and $i, j = M + 1, \dots, N$ be the linker indices for the 96-mer and spike-in 12-mer arrays. We calculated the background level $B_{i,j}$ at (i, j) as

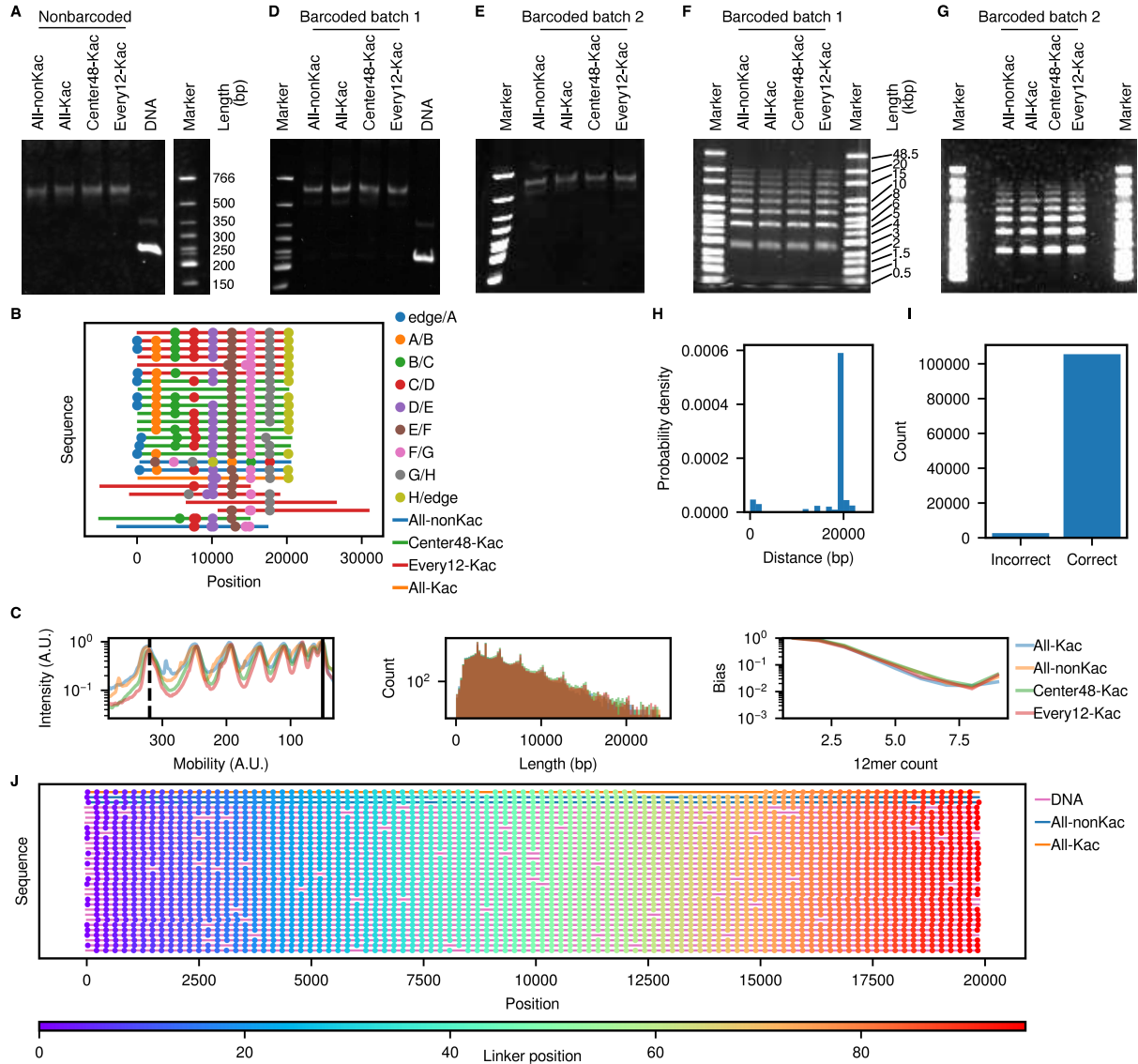
$$\begin{aligned} D_i &= \sum_{j=1}^N C_{i,j} \\ E_i &= \text{median}_{j=M+1}^N \left(\frac{C_{i,j}}{D_j} \right) \\ B_{i,j} &= (D_i E_j + D_j E_i) / 2 \end{aligned}$$

assuming $C_{i,j} \approx \beta C'_i C'_j$ where C'_i is the concentration of fragment containing the i -th linker and β is the efficiency for random ligation.

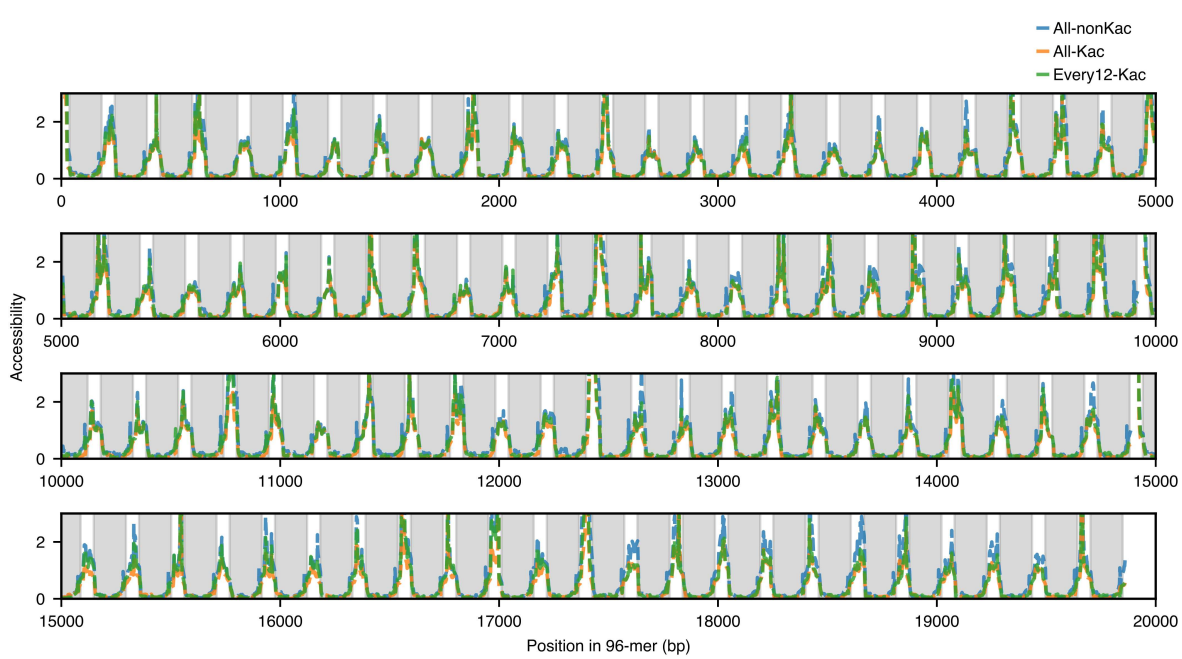
Supplementary Figures



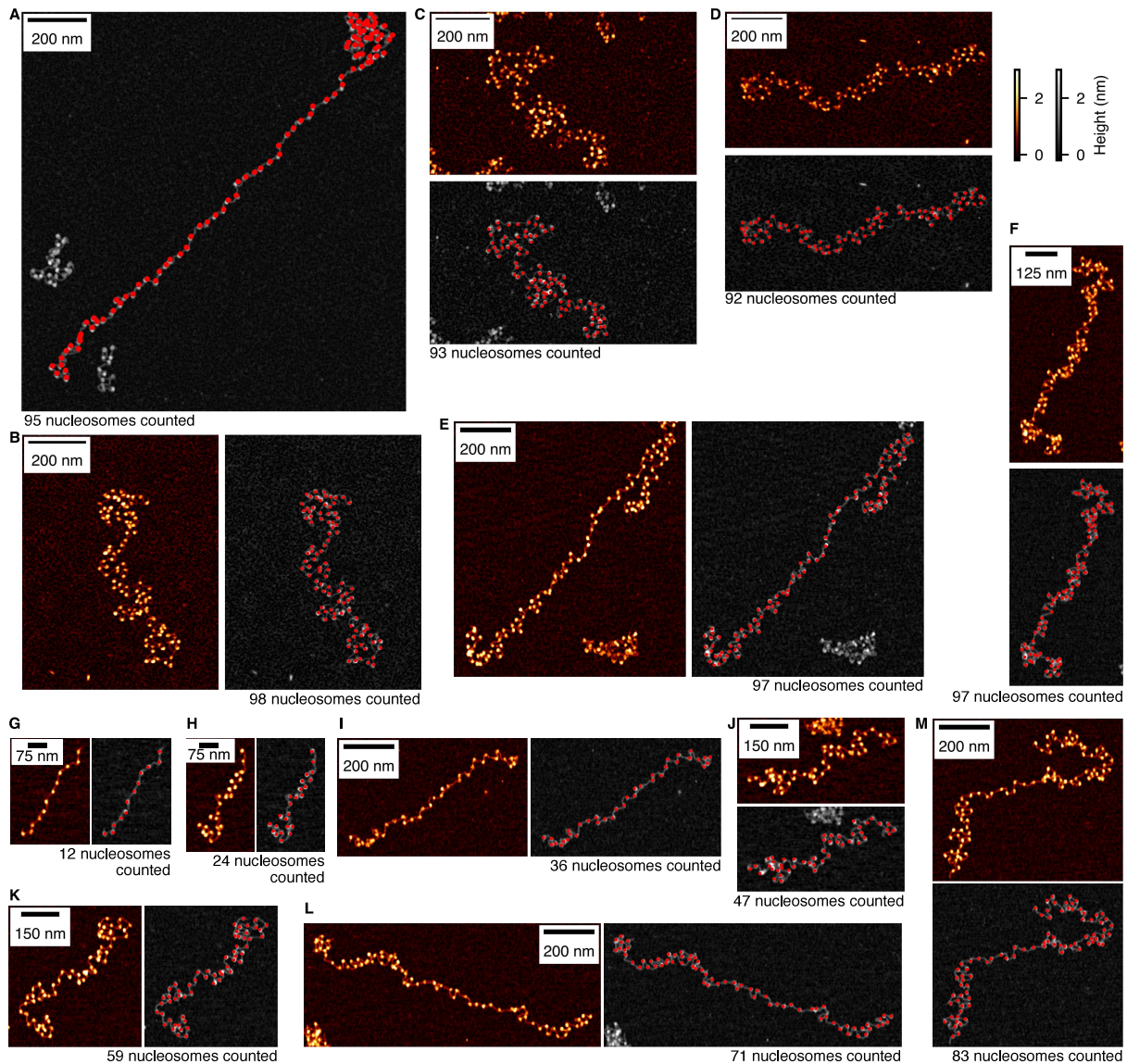
Supplementary Fig. S1: Validation of acetylated and non-acetylated 12-mer arrays. (A) SDS-PAGE of reconstituted histone octamers with and without H4 Lysine tail acetylation. (B) Schematic of nucleosome reconstitution confirmation by gel-shift assay after ScaI digestion. (C-I) Confirmation of the nucleosome reconstitution by gel-shift assay for the non-barcoded (C) and barcoded (D-I) 12-mer arrays. (J) Example snapshots of AFM with reconstituted 12-mer arrays with barcode. (K) Distribution of the nucleosome counts in the clusters found in the AFM images.



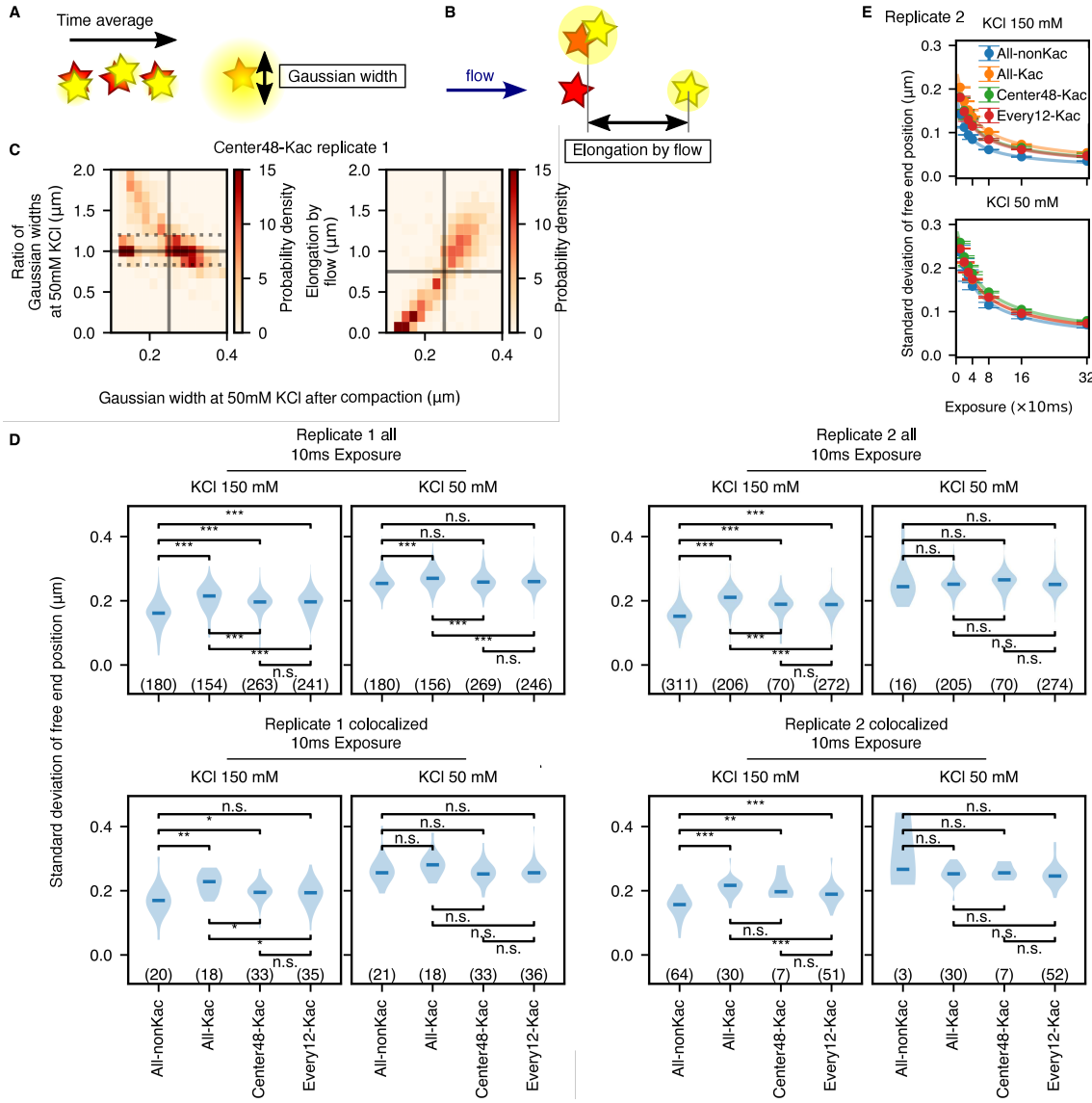
Supplementary Fig. S2: Validation of ligated arrays. (A) Confirmation of the nucleosome reconstitution by gel-shift assay for the non-barcoded ligated arrays. (B) Each sequence for Fig. 1E. (C) Illustration of nanopore sequencing bias. The left, center, and right plots show the fluorescent intensity in 0.3 % agarose gel electrophoresis, the length distribution of the sequences, and the estimated read bias, respectively. In the left plot, the black dashed and solid lines show the mobility for the 12-mer and 96-mer, respectively. The plots show the data for experiment 2 for the non-barcoded array (Table S1). (D,E) Confirmation of the nucleosome reconstitution by gel-shift assay for the barcoded ligated arrays. (F,G) Electrophoresis result of the ligated product of eight barcoded 12-mer arrays. (H) Sequence bias-corrected distribution of the length of barcoded DNA when subsampling the sequences that include both ends of the 96-mer design. (I) The correct and incorrect ligation count at the junctions for the barcoded arrays. (J) Aligned sequences of the barcoded arrays with a length close to 96-mer.



Supplementary Fig. S3: Accessibility assay of the ligated arrays. The accessibility was measured as the ratio of the fraction of adenine methylated by EcoGII for the ligated nucleosome arrays to that of DNA without histones.

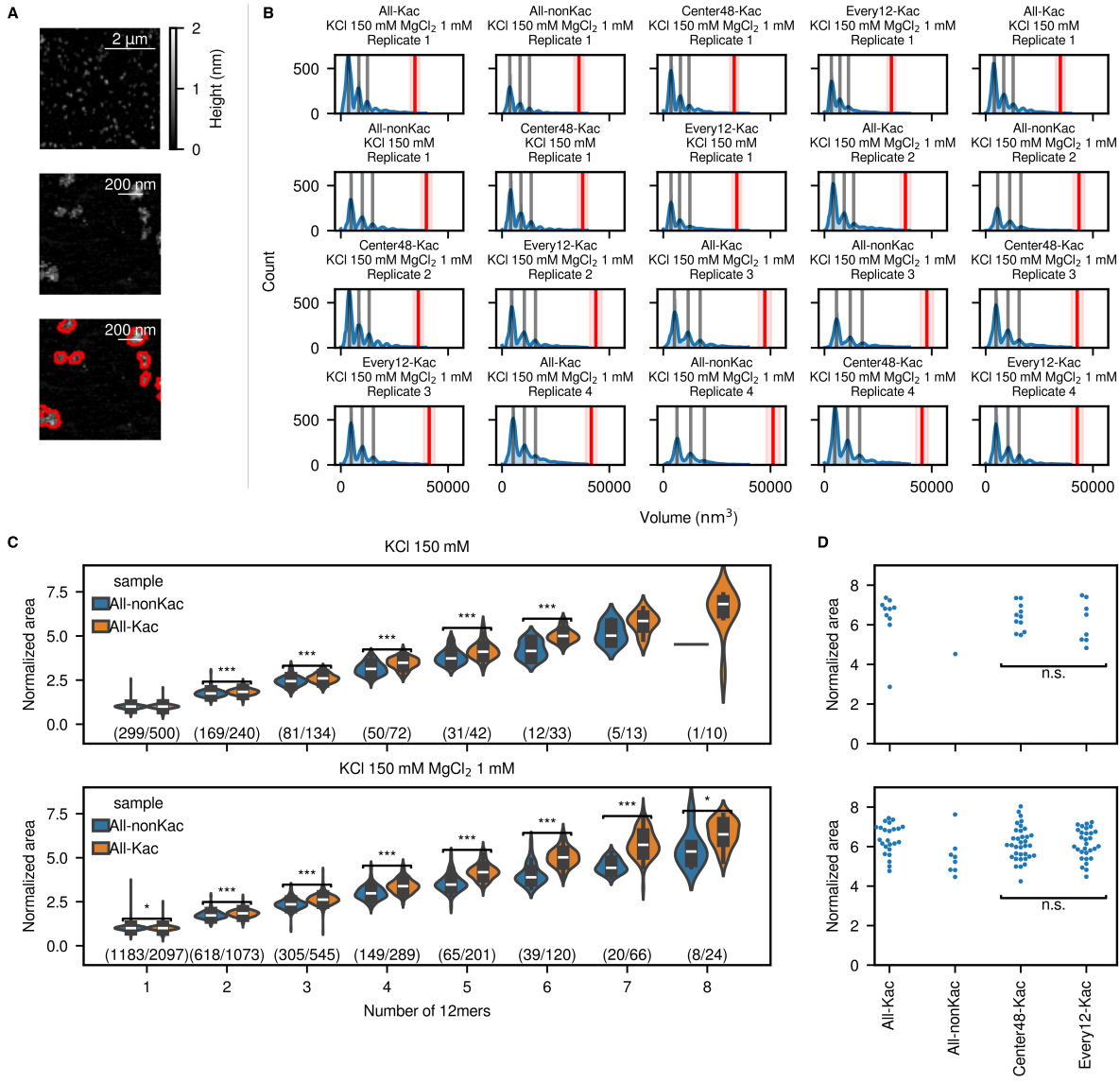


Supplementary Fig. S4: AFM images and nucleosome counts of reconstituted arrays. **(A-F)** Arrays with nucleosome counts close to 96. **(G-M)** Arrays with nucleosome counts close to $1 \times 12, \dots, 7 \times 12$. All-nonKac (A,I,K-M), All-Kac (B,F) Center48-Kac (C), and Every12-Kac (D,E,G,H,J) samples. Bar-coded (A,E-M) and non-barcoded (B-D). The raw image for (A) is shown as Fig. 1I. The red points show the detected nucleosome positions.

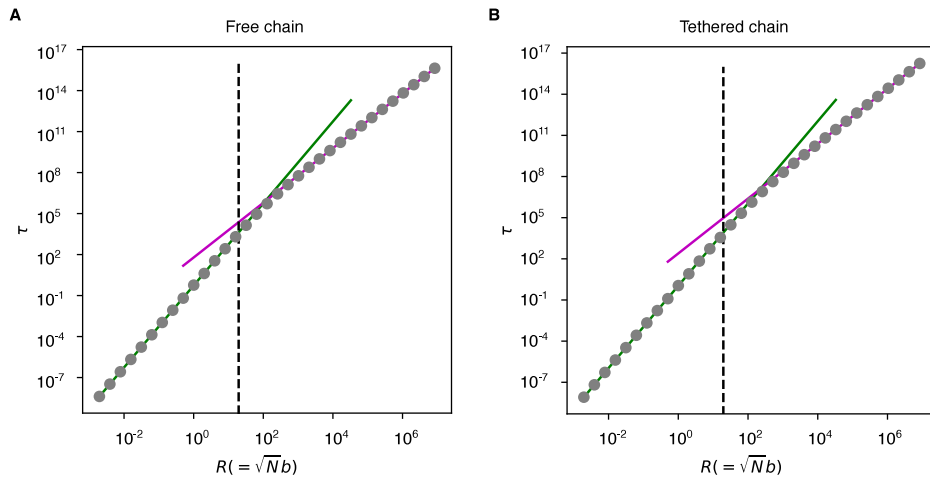


Supplementary Fig. S5: Filtering scheme and replicate results for single-molecule microscopy.

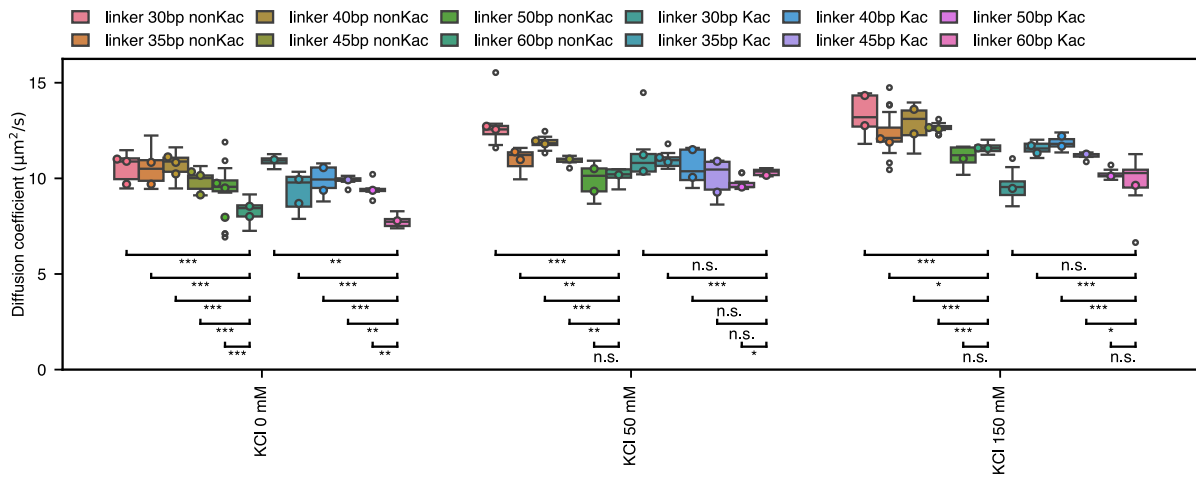
(A,B) Schematic for the definition of the Gaussian width (A) and the elongation by flow (B). (C) (left) 2D histogram of the Gaussian width at 50mM KCl (after compaction by 150mM KCl) and the ratio of the Gaussian widths before and after the compaction. (right) 2D histogram of the Gaussian width at 50mM KCl after the compaction and the elongation by flow. The solid gray line shows the thresholds for the Gaussian width after compaction and elongation by flow. The gray dotted lines show the thresholds for the ratio of Gaussian widths before and after the compaction. The plots show data for the Center48-Kac sample (replicate 1). (D) Replicate results for Fig. 2D, plotted using all the filtered free end tracks (top) and only tracks that colocalize with the tethered end fluorescent signals (bottom). The asterisks indicate the statistical significance of the Mann-Whitney test adjusted by the Benjamini-Yekutieli method: “*”, “**”, and “***” correspond to statistical significance with $p < 0.05$, $p < 0.01$, and $p < 0.001$, respectively. “n.s.” means not significant. The numbers in parentheses indicate the number of analyzed spots. (E) Replicate results for Fig. 2F.



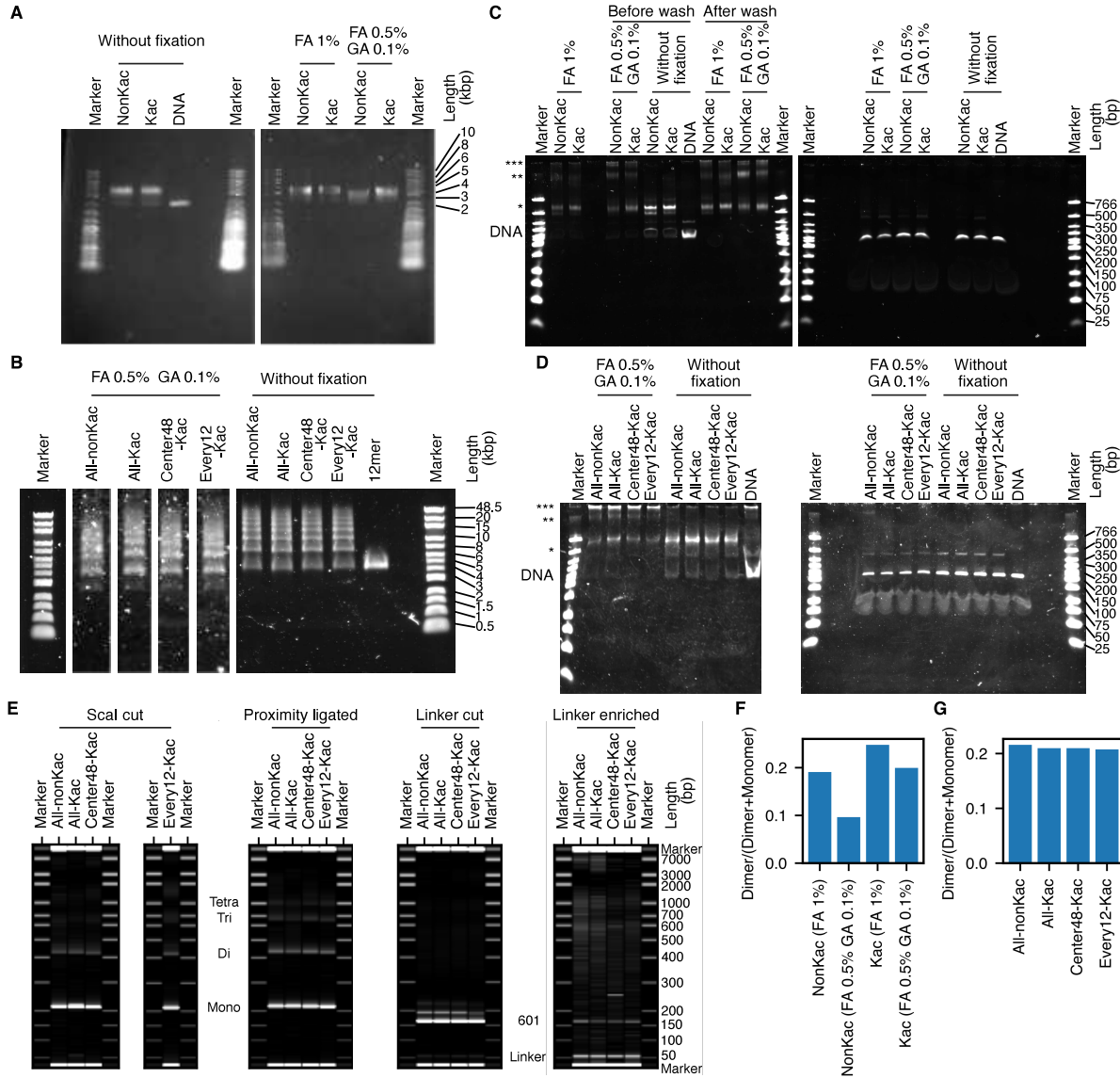
Supplementary Fig. S6: Size measurement of ligated products using AFM. **(A)** Representative low-resolution AFM images of ligated products. Red lines indicate the boundaries of the detected blobs. **(B)** Histograms showing the measured volumes of the blobs. Gray lines correspond to the estimated volumes for 12-mer, 24-mer, and 36-mer. The red line and shaded region show the estimated volume and volume range of the 96-mer. **(C)** Blob area normalized to that of the 12-mer, grouped by the count of the 12mers estimated by the volume. The numbers in parentheses indicate the number of analyzed blobs. The asterisks indicate the statistical significance of the Mann-Whitney test: “*”, “**”, and “***” correspond to statistical significance with $p < 0.05$, $p < 0.01$, and $p < 0.001$, respectively. A non-significant difference is indicated by the absence of an asterisk. **(D)** Pattern-dependent normalized areas for arrays whose volumes are in the estimated range for the 96-mer. “n.s.” indicates a non-significant difference according to the Mann-Whitney test.



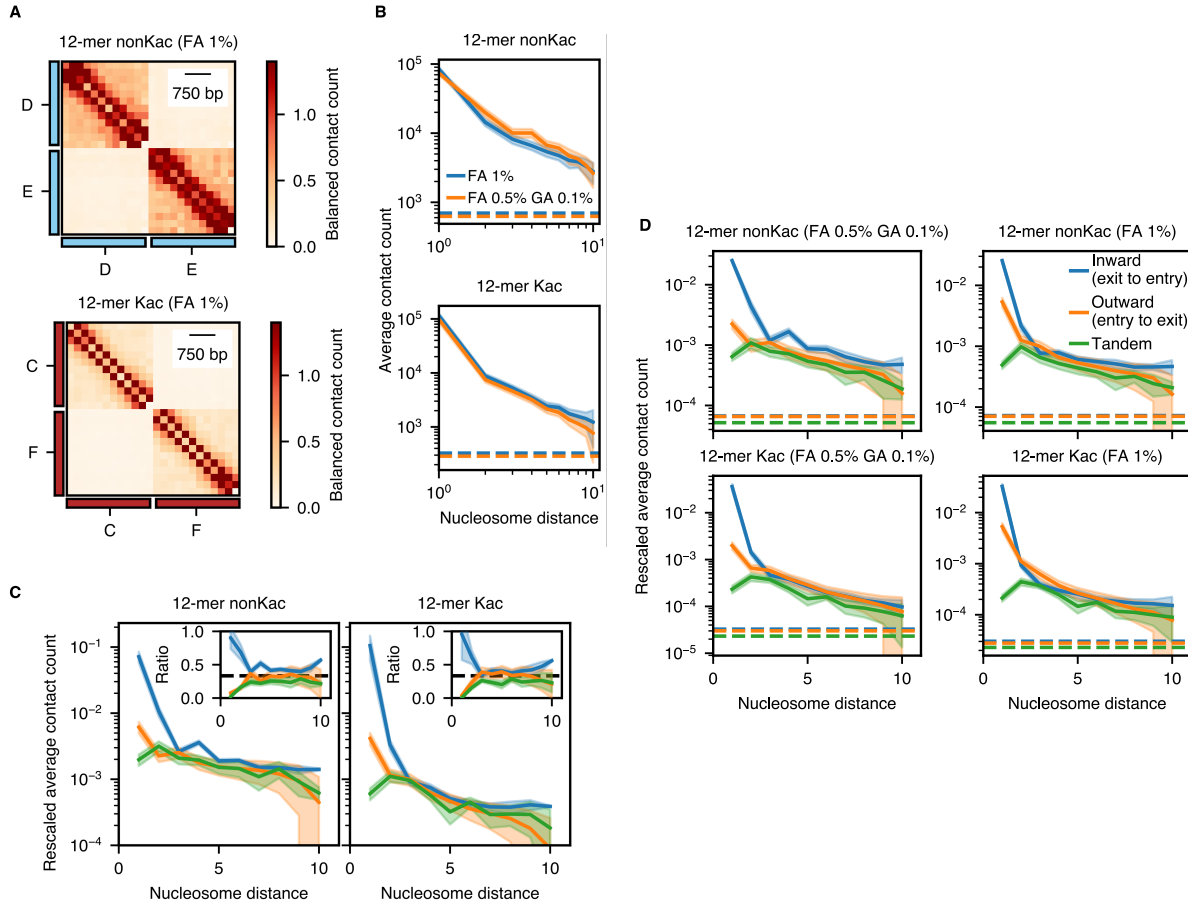
Supplementary Fig. S7: Comparison between experimental data and Zimm model. Zimm model numerics for prefactor estimation regarding the relation between size $R = \sqrt{N}b$ and time scale τ (see section ‘Zimm model with tethered end’ in the supplementary). The Kuhn length b is varied with fixed $a = 1$ as well as $\eta = k_B T = 1$, and $N = 96$. Dashed line is at $b = 2$. Green lines are extensions of fits using the two left-most points to obtain α , and the magenta lines are fits using the two right-most points for ν . **(A)** Free chain case. Green line: $\tau = 0.5501R^{2.9998}$. Magenta line: $\tau = 1.9993R^{2.0000}$, where the exponents and the prefactor are both fitting parameters. **(B)** Tethered chain case. Green line: $\tau = 1.0857R^{2.9998}$. Magenta line: $\tau = 8.0771R^{2.0000}$, where the exponents and the prefactor are both fitting parameters.



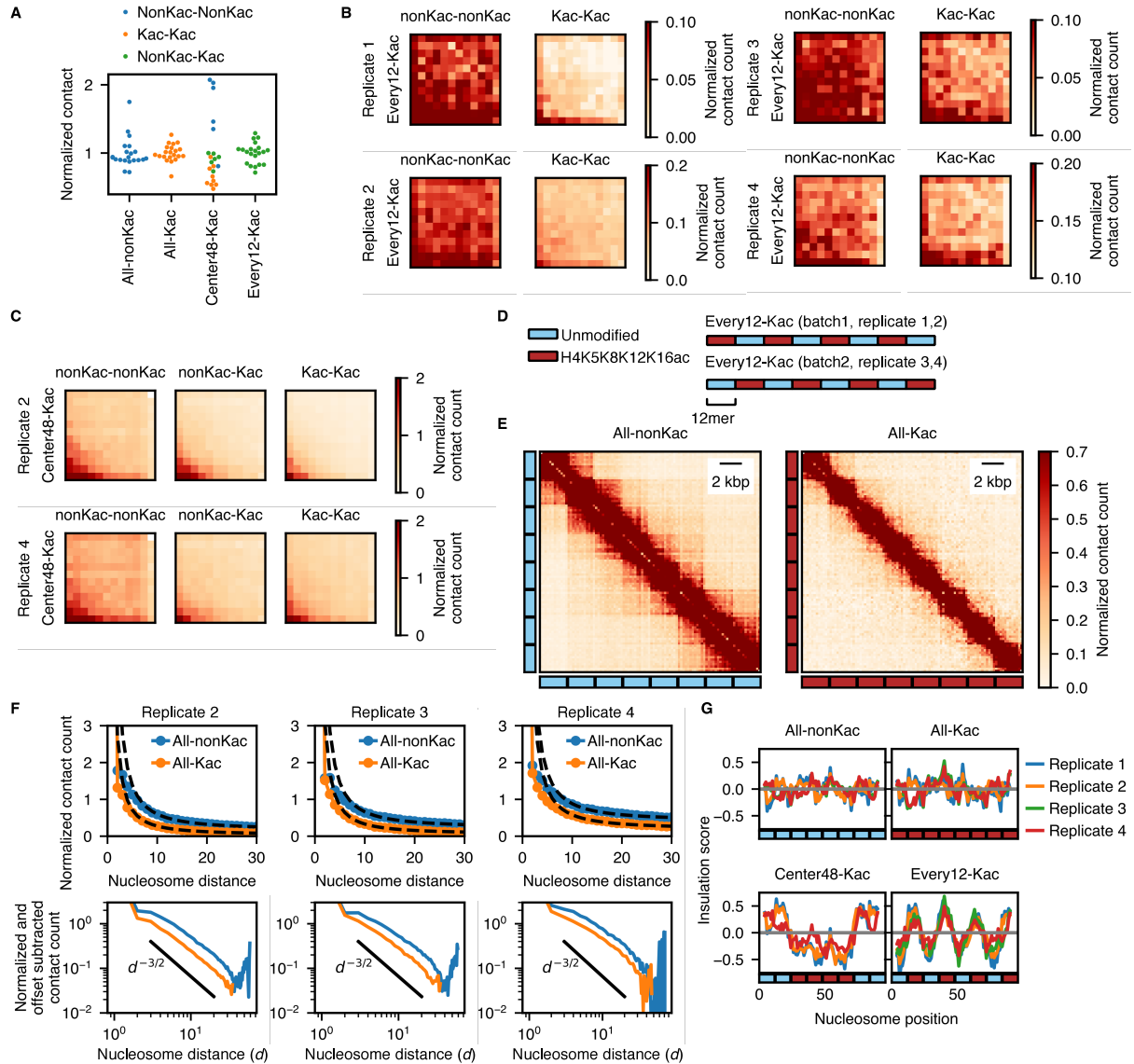
Supplementary Fig. S8: Diffusion coefficients of free-floating 12-mer arrays measured by dynamic light scattering. Complete dataset corresponding to Fig. 2E. Refer to the caption of Fig. 2E for details on the annotations indicating statistical significance and boxplot elements. The value estimated using the averaged autocorrelation for each observation is shown by the circular filled symbols.



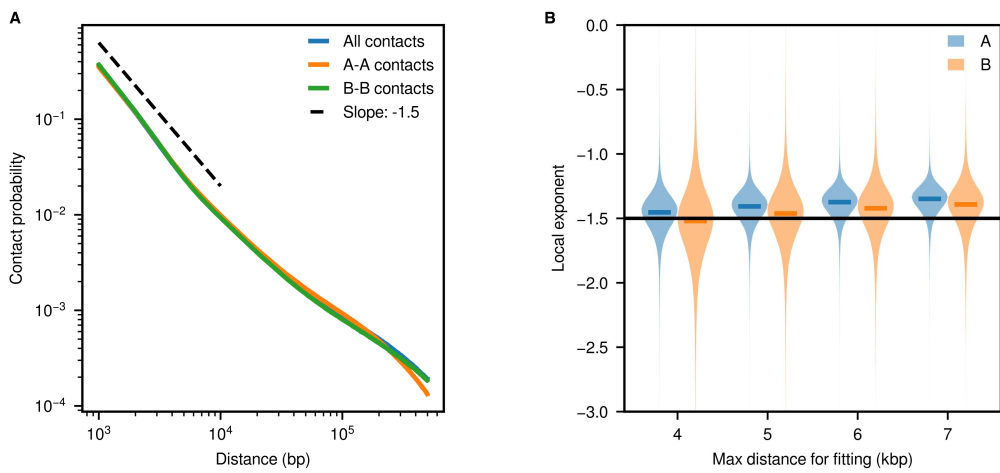
Supplementary Fig. S9: Experimental details of the contact map experiment. (A) 0.7 % agarose gel electrophoresis in 0.2X TBE of the 12-mer samples before and after fixation. (B) 0.3 % agarose gel electrophoresis in 0.2X TBE of the ligated samples before and after fixation. (C,D) 5 % native PAGE in 1X TBE of 12-mer (C) and ligated (D) samples after ScaI digestion. The left and right gels correspond to the samples before and after SDS/PK digestion, respectively. The band positions for the bare DNA, mononucleosome, dinucleosome, and products with lower mobility are shown by the text “DNA” and the single, double, and triple asterisks, respectively. (E) Pseudogel images showing the Bioanalyzer traces in each protocol step (see Materials and Methods). In the left images, the band positions for the single, double, triple, and tetra nucleosomes are shown, respectively, by the text “Mono”, “Di”, “Tri”, and “Tetra”. In the right images, the band positions for the Widom 601 and linker sequences are shown by the texts “601” and “Linker”. (F,G) Relative abundance of dinucleosomes after ScaI digestion, calculated from the bioanalyzer traces. 12-mer samples (F) and ligated samples (G). FA and GA abbreviate formaldehyde and glutaraldehyde.



Supplementary Fig. S10: Fixation method dependence on *in vitro* Hi-C. **(A)** Contact map obtained from mixed 12-mers with distinct barcodes fixed with 1 % of formaldehyde (FA). The contact is balanced and normalized so that the average contact frequency is 1. **(B)** Contact frequency as a function of the nucleosome position with different fixation me thods. The shaded area represents the uncertainty (twice the s.e.m.). The dashed lines indicate the average contact frequency of the barcodes originating from the different 12-mer arrays. **(C)** The same plot as Fig. 3F for the balanced matrices. **(D)** Raw data for Fig. 3F and the same plot for the samples fixed with 1 % FA. The shaded area represents the uncertainty (twice the s.e.m.). The dashed lines indicate the background level, estimated as the average contact frequency of the barcodes originating from the different 12-mer arrays.



Supplementary Fig. S11: Additional results of *in vitro* Hi-C for ligated arrays. (A) All data for Fig. 4C, categorized by the nucleosome type. (B) Accumulated contact frequency between second adjacent 12-mer regions for the Every12-Kac arrays. (C) Replicate results for Fig. 4D. (D) Design of histone modification patterns for the Every12-Kac arrays in each replicate. (E) All-to-all contact map of the ligated nucleosome arrays with homogeneous patterns. (F) Replicate results for Fig. 4F. (G) Replicate results for Fig. 4G with the data for homogeneous arrays. The sequence of replicates 2 and 3 for Every12 arrays are flipped to match the modification patterns (See (D)).



Supplementary Fig. S12: Power-law decay of Micro-C contact probability for mouse ES cells using data from Ref. (49). (A) Distance-dependent average contact probability categorized by the compartments. The black dashed line indicates a power-law decay with an exponent of -1.5 . (B) Local power-law exponent in 20 kbp window, calculated for each compartment. Exponents were estimated within genomic distances ranging from 2 kbp to 4 – 7 kbp. The black line indicates the exponent -1.5 .

Supplementary Tables

Supplementary Table S1: (Attached as a separate file) Summary of nanopore sequencing experiments. “gDNA” protocol was used for all experiments.

Supplementary Table S2: (Attached as a separate file) Sequences for the 12mer plasmids.

Supplementary Table S3: (Attached as a separate file) Source data for Fig. 2E and fig. S8.

REFERENCES AND NOTES

1. J. R. Dixon, I. Jung, S. Selvaraj, Y. Shen, J. E. Antosiewicz-Bourget, A. Y. Lee, Z. Ye, A. Kim, N. Rajagopal, W. Xie, Y. Diao, J. Liang, H. Zhao, V. V. Lobanenkov, J. R. Ecker, J. A. Thomson, B. Ren, Chromatin architecture reorganization during stem cell differentiation. *Nature* **518**, 331–336 (2015).
2. A. Burton, M.-E. Torres-Padilla, Chromatin dynamics in the regulation of cell fate allocation during early embryogenesis. *Nat. Rev. Mol. Cell Biol.* **15**, 723–735 (2014).
3. J. D. Buenrostro, B. Wu, U. M. Litzenburger, D. Ruff, M. L. Gonzales, M. P. Snyder, H. Y. Chang, W. J. Greenleaf, Single-cell chromatin accessibility reveals principles of regulatory variation. *Nature* **523**, 486–490 (2015).
4. S. Park, R. Merino-Urteaga, V. Karwacki-Neisius, G. E. Carrizo, A. Athreya, A. Marin-Gonzalez, N. A. Benning, J. Park, M. M. Mitchener, N. V. Bhanu, B. A. Garcia, B. Zhang, T. W. Muir, E. L. Pearce, T. Ha, Native nucleosomes intrinsically encode genome organization principles. *Nature* **643**, 572–581 (2025).
5. J. Xu, H. Ma, J. Jin, S. Uttam, R. Fu, Y. Huang, Y. Liu, Super-resolution imaging of higher-order chromatin structures at different epigenomic states in single mammalian cells. *Cell Rep.* **24**, 873–882 (2018).
6. C. Tse, T. Sera, A. P. Wolffe, J. C. Hansen, Disruption of higher-order folding by core histone acetylation dramatically enhances transcription of nucleosomal arrays by RNA polymerase III. *Mol. Cell. Biol.* **18**, 4629–4638 (1998).
7. M. Shogren-Knaak, H. Ishii, J.-M. Sun, M. J. Pazin, J. R. Davie, C. L. Peterson, Histone H4-K16 acetylation controls chromatin structure and protein interactions. *Science* **311**, 844–847 (2006).
8. A. Allahverdi, R. Yang, N. Korolev, Y. Fan, C. A. Davey, C.-F. Liu, L. Nordenskiöld, The effects of histone H4 tail acetylations on cation-induced chromatin folding and self-association. *Nucleic Acids Res.* **39**, 1680–1691 (2011).

9. J. J. Funke, P. Ketterer, C. Lieleg, S. Schunter, P. Korber, H. Dietz, Uncovering the forces between nucleosomes using DNA origami. *Sci. Adv.* **2**, e1600974 (2016).
10. C. Dhalluin, J. E. Carlson, L. Zeng, C. He, A. K. Aggarwal, M.-M. Zhou, M.-M. Zhou, Structure and ligand of a histone acetyltransferase bromodomain. *Nature* **399**, 491–496 (1999).
11. J. Lovén, H. A. Hoke, C. Y. Lin, A. Lau, D. A. Orlando, C. R. Vakoc, J. E. Bradner, T. I. Lee, R. A. Young, Selective inhibition of tumor oncogenes by disruption of super-enhancers. *Cell* **153**, 320–334 (2013).
12. A. J. Bannister, P. Zegerman, J. F. Partridge, E. A. Miska, J. O. Thomas, R. C. Allshire, T. Kouzarides, Selective recognition of methylated lysine 9 on histone H3 by the HP1 chromo domain. *Nature* **410**, 120–124 (2001).
13. M. Lachner, D. O’Carroll, S. Rea, K. Mechtler, T. Jenuwein, Methylation of histone H3 lysine 9 creates a binding site for HP1 proteins. *Nature* **410**, 116–120 (2001).
14. S. Machida, Y. Takizawa, M. Ishimaru, Y. Sugita, S. Sekine, J.-i. Nakayama, M. Wolf, H. Kurumizaka, Structural basis of heterochromatin formation by human HP1. *Mol. Cell* **69**, 385–397.e8 (2018).
15. S. Poepsel, V. Kasinath, E. Nogales, Cryo-EM structures of PRC2 simultaneously engaged with two functionally distinct nucleosomes. *Nat. Struct. Mol. Biol.* **25**, 154–162 (2018).
16. N. J. Francis, R. E. Kingston, C. L. Woodcock, Chromatin compaction by a polycomb group protein complex. *Science* **306**, 1574–1577 (2004).
17. S. Kilic, S. Felekyan, O. Doroshenko, I. Boichenko, M. Dimura, H. Vardanyan, L. C. Bryan, G. Arya, C. A. M. Seidel, B. Fierz, Single-molecule FRET reveals multiscale chromatin dynamics modulated by HP1 α . *Nat. Commun.* **9**, 235 (2018).
18. F. Song, P. Chen, D. Sun, M. Wang, L. Dong, D. Liang, R.-M. Xu, P. Zhu, G. Li, Cryo-EM study of the chromatin fiber reveals a double helix twisted by tetranucleosomal units. *Science* **344**, 376–380 (2014).

19. B. A. Gibson, L. K. Doolittle, M. W. G. Schneider, L. E. Jensen, N. Gamarra, L. Henry, D. W. Gerlich, S. Redding, M. K. Rosen, Organization of chromatin by intrinsic and regulated phase separation. *Cell* **179**, 470–484.e21 (2019).
20. H. Strickfaden, T. O. Tolsma, A. Sharma, D. A. Underhill, J. C. Hansen, M. J. Hendzel, Condensed Chromatin behaves like a solid on the mesoscale in vitro and in living cells. *Cell* **183**, 1772–1784.e13 (2020).
21. S. Portillo-Ledesma, Z. Li, T. Schlick, Genome modeling: From chromatin fibers to genes. *Curr. Opin. Struct. Biol.* **78**, 102506 (2023).
22. L. N. Mishra, J. J. Hayes, A nucleosome-free region locally abrogates histone H1–Dependent restriction of linker DNA accessibility in chromatin. *J. Biol. Chem.* **293**, 19191–19200 (2018).
23. M. M. Müller, B. Fierz, L. Bittova, G. Liszczak, T. W. Muir, A two-state activation mechanism controls the histone methyltransferase Suv39h1. *Nat. Chem. Biol.* **12**, 188–193 (2016).
24. M. J. Blacketer, S. J. Feely, M. A. Shogren-Knaak, Nucleosome interactions and stability in an ordered nucleosome array model system. *J. Biol. Chem.* **285**, 34597–34607 (2010).
25. P. T. Lowary, J. Widom, New DNA sequence rules for high affinity binding to histone octamer and sequence-directed nucleosome positioning. *J. Mol. Biol.* **276**, 19–42 (1998).
26. B. M. Turner, Histone acetylation and control of gene expression. *J. Cell Sci.* **99**, 13–20 (1991).
27. M. Grunstein, Histone acetylation in chromatin structure and transcription. *Nature* **389**, 349–352 (1997).
28. M. Wakamori, Y. Fujii, N. Suka, M. Shirouzu, K. Sakamoto, T. Umehara, S. Yokoyama, Intra-and inter-nucleosomal interactions of the histone H4 tail revealed with a human nucleosome core particle with genetically-incorporated H4 tetra-acetylation. *Sci. Rep.* **5**, 17204 (2015).

29. M. Wakamori, K. Okabe, K. Ura, T. Funatsu, M. Takinoue, T. Umehara, Quantification of the effect of site-specific histone acetylation on chromatin transcription rate. *Nucleic Acids Res.* **48**, 12648–12659 (2020).
30. Z. Shipony, G. K. Marinov, M. P. Swaffer, N. A. Sinnott-Armstrong, J. M. Skotheim, A. Kundaje, W. J. Greenleaf, Long-range single-molecule mapping of chromatin accessibility in eukaryotes. *Nat. Methods* **17**, 319–327 (2020).
31. A. B. Stergachis, B. M. Debo, E. Haugen, L. S. Churchman, J. A. Stamatoyannopoulos, Single-molecule regulatory architectures captured by chromatin fiber sequencing. *Science* **368**, 1449–1454 (2020).
32. Q. Chen, R. Yang, N. Korolev, C. F. Liu, L. Nordenskiöld, Regulation of nucleosome stacking and chromatin compaction by the histone H4 N-terminal tail–H2A acidic patch interaction. *J. Mol. Biol.* **429**, 2075–2092 (2017).
33. B. H. Zimm, Dynamics of polymer molecules in dilute solution: Viscoelasticity, flow birefringence and dielectric loss. *J. Chem. Phys.* **24**, 269–278 (1956).
34. M. Doi, S. F. Edwards, *The Theory of Polymer Dynamics* (Oxford Univ. Press, 1988), vol. 73.
35. A. J. Goldman, R. G. Cox, H. Brenner, Slow viscous motion of a sphere parallel to a plane wall—I Motion through a quiescent fluid. *Chem. Eng. Sci.* **22**, 637–651 (1967).
36. J. Yao, P. T. Lowary, J. Widom, Direct detection of linker DNA bending in defined-length oligomers of chromatin. *Proc. Natl. Acad. Sci. U.S.A.* **87**, 7603–7607 (1990).
37. E. Lieberman-Aiden, N. L. van Berkum, L. Williams, M. Imakaev, T. Ragoczy, A. Telling, I. Amit, B. R. Lajoie, P. J. Sabo, M. O. Dorschner, R. Sandstrom, B. Bernstein, M. A. Bender, M. Groudine, A. Gnirke, J. Stamatoyannopoulos, L. A. Mirny, E. S. Lander, J. Dekker, Comprehensive mapping of long-range interactions reveals folding principles of the human genome. *Science* **326**, 289–293 (2009).

38. E. Oberbeckmann, K. Quililan, P. Cramer, A. M. Oudelaar, In vitro reconstitution of chromatin domains shows a role for nucleosome positioning in 3D genome organization. *Nat. Genet.* **56**, 483–492 (2024).
39. M. Ohno, T. Ando, D. G. Priest, V. Kumar, Y. Yoshida, Y. Taniguchi, Sub-nucleosomal genome structure reveals distinct nucleosome folding motifs. *Cell* **176**, 520–534.e25 (2019).
40. K. Maeshima, R. Rogge, S. Tamura, Y. Joti, T. Hikima, H. Szerlong, C. Krause, J. Herman, E. Seidel, J. DeLuca, T. Ishikawa, J. C. Hansen, Nucleosomal arrays self-assemble into supramolecular globular structures lacking 30-nm fibers. *EMBO J.* **35**, 1115–1132 (2016).
41. D. E. Olins, A. L. Olins, Chromatin history: Our view from the bridge. *Nat. Rev. Mol. Cell Biol.* **4**, 809–814 (2003).
42. A. Routh, S. Sandin, D. Rhodes, Nucleosome repeat length and linker histone stoichiometry determine chromatin fiber structure. *Proc. Natl. Acad. Sci. U.S.A.* **105**, 8872–8877 (2008).
43. N. Jentink, C. Purnell, B. Kable, M. T. Swulius, S. A. Grigoryev, Cryoelectron tomography reveals the multiplex anatomy of condensed native chromatin and its unfolding by histone citrullination. *Mol. Cell* **83**, 3236–3252.e7 (2023).
44. S. Cai, Y. Song, C. Chen, J. Shi, L. Gan, Natural chromatin is heterogeneous and self-associates in vitro. *Mol. Biol. Cell* **29**, 1652–1663 (2018).
45. E. Crane, Q. Bian, R. P. McCord, B. R. Lajoie, B. S. Wheeler, E. J. Ralston, S. Uzawa, J. Dekker, B. J. Meyer, Condensin-driven remodelling of X chromosome topology during dosage compensation. *Nature* **523**, 240–244 (2015).
46. Y. Cui, C. Bustamante, Pulling a single chromatin fiber reveals the forces that maintain its higher-order structure. *Proc. Natl. Acad. Sci. U.S.A.* **97**, 127–132 (2000).
47. J. D. Halverson, J. Smrek, K. Kremer, A. Y. Grosberg, From a melt of rings to chromosome territories: The role of topological constraints in genome folding. *Rep. Prog. Phys.* **77**, 022601 (2014).

48. A. L. Sanborn, S. S. P. Rao, S.-C. Huang, N. C. Durand, M. H. Huntley, A. I. Jewett, I. D. Bochkov, D. Chinnappan, A. Cutkosky, J. Li, K. P. Geeting, A. Gnirke, A. Melnikov, D. McKenna, E. K. Stamenova, E. S. Lander, E. L. Aiden, Chromatin extrusion explains key features of loop and domain formation in wild-type and engineered genomes. *Proc. Natl. Acad. Sci. U.S.A.* **112**, E6456–E6465 (2015).
49. T.-H. S. Hsieh, C. Cattoglio, E. Slobodyanyuk, A. S. Hansen, O. J. Rando, R. Tjian, X. Darzacq, Resolving the 3D landscape of transcription-linked mammalian chromatin folding. *Mol. Cell* **78**, 539–553.e8 (2020).
50. K. Adachi, K. Kawaguchi, Chromatin state switching in a polymer model with mark-conformation coupling. *Phys. Rev. E* **100**, 060401 (2019).
51. M. Barbieri, M. Chotalia, J. Fraser, L.-M. Lavitas, J. Dostie, A. Pombo, M. Nicodemi, Complexity of chromatin folding is captured by the strings and binders switch model. *Proc. Natl. Acad. Sci. U.S.A.* **109**, 16173–16178 (2012).
52. R. Collepardo-Guevara, G. Portella, M. Vendruscolo, D. Frenkel, T. Schlick, M. Orozco, Chromatin unfolding by epigenetic modifications explained by dramatic impairment of internucleosome interactions: A multiscale computational study. *J. Am. Chem. Soc.* **137**, 10205–10215 (2015).
53. D. Michieletto, E. Orlandini, D. Marenduzzo, Polymer model with epigenetic recoloring reveals a pathway for the de novo establishment and 3D organization of chromatin domains. *Phys. Rev. X* **6**, 041047 (2016).
54. T. Brouwer, C. Pham, A. Kaczmarczyk, W.-J. De Voogd, M. Botto, P. Vizjak, F. Mueller-Planitz, J. van Noort, A critical role for linker DNA in higher-order folding of chromatin fibers. *Nucleic Acids Res.* **49**, 2537–2551 (2021).
55. M. Kikuchi, S. Morita, M. Wakamori, S. Sato, T. Uchikubo-Kamo, T. Suzuki, N. Dohmae, M. Shirouzu, T. Umehara, Epigenetic mechanisms to propagate histone acetylation by P300/CBP. *Nat. Commun.* **14**, 4103 (2023).

56. M. Mivelaz, B. Fierz, Observing protein interaction dynamics to chemically defined chromatin fibers by colocalization single-molecule fluorescence microscopy. *Methods* **184**, 112–124 (2020).
57. M. Tokunaga, N. Imamoto, K. Sakata-Sogawa, Highly inclined thin illumination enables clear single-molecule imaging in cells. *Nat. Methods* **5**, 159–161 (2008).
58. A. Edelstein, N. Amodaj, K. Hoover, R. Vale, N. Stuurman, Computer control of microscopes using µManager. *Curr. Protoc. Mol. Biol.* **92**, 14.20.1–14.20.17 (2010).
59. H. Pinkard, N. Stuurman, I. E. Ivanov, N. M. Anthony, W. Ouyang, B. Li, B. Yang, M. A. Tsuchida, B. Chhun, G. Zhang, R. Mei, M. Anderson, D. P. Shepherd, I. Hunt-Isaak, R. L. Dunn, W. Jahr, S. Kato, L. A. Royer, J. R. Thiagarajah, K. W. Eliceiri, E. Lundberg, S. B. Mehta, L. Waller, Pycro-Manager: Open-source software for customized and reproducible microscope control. *Nat. Methods* **18**, 226–228 (2021).
60. S. W. Provencher, CONTIN: A general purpose constrained regularization program for inverting noisy linear algebraic and integral equations. *Comput. Phys. Commun.* **27**, 229–242 (1982).
61. A. Scotti, W. Liu, J. S. Hyatt, E. S. Herman, H. S. Choi, J. W. Kim, L. A. Lyon, U. Gasser, A. Fernandez-Nieves, The CONTIN algorithm and its application to determine the size distribution of microgel Suspensions. *J. Chem. Phys.* **142**, 234905 (2015).
62. Stephen Provencher, CONTIN. <http://lcmodel.ca/contin.shtml>.
63. Oxford Nanopore Technologies PLC, Nanoporetech/Dorado. <https://github.com/nanoporetech/dorado>.
64. Oxford Nanopore Technologies PLC, Nanoporetech/modkit. <https://github.com/nanoporetech/modkit>.
65. S. van der Walt, J. L. Schönberger, J. Nunez-Iglesias, F. Boulogne, J. D. Warner, N. Yager, E. Gouillart, T. Yu, scikit-image contributors, Scikit-image: Image processing in Python. *PeerJ* **2**, e453 (2014).

66. P. A. Knight, D. Ruiz, A fast algorithm for matrix balancing. *IMA J. Numer. Anal.* **33**, 1029–1047 (2013).
67. S. B. Reiff, A. J. Schroeder, K. Kırkı, A. Cosolo, C. Bakker, L. Mercado, S. Lee, A. D. Veit, A. K. Balashov, C. Vitzthum, W. Ronchetti, K. M. Pitman, J. Johnson, S. R. Ehmsen, P. Kerpedjiev, N. Abdennur, M. Imakaev, S. U. Öztürk, U. Çamoğlu, L. A. Mirny, N. Gehlenborg, B. H. Alver, P. J. Park, The 4D nucleome data portal as a resource for searching and visualizing curated nucleomics data. *Nat. Commun.* **13**, 2365 (2022).
68. J. Dekker, A. S. Belmont, M. Guttmann, V. O. Leshyk, J. T. Lis, S. Lomvardas, L. A. Mirny, C. C. O’Shea, P. J. Park, B. Ren, J. C. R. Politz, J. Shendure, S. Zhong, The 4D nucleome project. *Nature* **549**, 219–226 (2017).
69. B. Dorigo, T. Schalch, K. Bystricky, T. J. Richmond, Chromatin fiber folding: Requirement for the histone H4 N-terminal tail. *J. Mol. Biol.* **327**, 85–96 (2003).
70. Z. Zhang, S. R. Park, A. Pertsinidis, A. Revyakin, Cloud-Point PEG Glass Surfaces for Imaging of Immobilized Single Molecules by Total-internal-reflection Microscopy. *Bio Protoc.* **6**, e1784 (2016).
71. N. Rohland, D. Reich, Cost-effective, high-throughput DNA sequencing libraries for multiplexed target capture. *Genome Res.* **22**, 939–946 (2012).
72. D. Nečas, P. Klapetek, Gwyddion: An open-source software for SPM data analysis. *Centr. Eur. J. Phys.* **10**, 181–188 (2012).
73. S. Kubo, K. Umeda, N. Kodera, S. Takada, Removing the parachuting artifact using two-way scanning data in high-speed atomic force microscopy. *Biophys. Physicobiol.* **20**, e200006 (2023).
74. D. Erb, pybaselines: A Python library of algorithms for the baseline correction of experimental data. 10.5281/zenodo.5608581, <https://github.com/derb12/pybaselines>.
75. P. J. A. Cock, T. Antao, J. T. Chang, B. A. Chapman, C. J. Cox, A. Dalke, I. Friedberg, T. Hamelryck, F. Kauff, B. Wilczynski, M. J. L. de Hoon, Biopython: Freely available Python

- tools for computational molecular biology and bioinformatics. *Bioinformatics* **25**, 1422–1423 (2009).
76. M. Roelfs, P. C. Kroon, tBuLi/Symfit: Symfit 0.5.6, *Zenodo* (2023); 10.5281/zenodo.7643591, <https://doi.org/10.5281/zenodo.7643591>.
77. Y. T. Fukai, K. Kawaguchi, LapTrack: Linear assignment particle tracking with tunable metrics. *Bioinformatics* **39**, btac799 (2023).
78. M. Koch, J.-U. Sommer, A. Blumen, Polymer chains tethered to impenetrable interfaces: Broadening of relaxation spectra. *J. Chem. Phys.* **106**, 1248–1256 (1997).